# AIX-MARSEILLE UNIVERSITÉ

Doctoral School: Sciences du Mouvement Humain

INSTITUT DES SCIENCES DU MOUVEMENT (UMR 7287)

A thesis submitted in fulfillment of the requirements for the degree of Doctor of Philosophy at Aix-Marseille Université

---

# Robotic touch for contact perception: Contributions to sensor design, manufacturing and signal processing

---

Xi Lin

Defended on 15th of December 2020 before committee:

| | | |
|---|---|---|
| Nathan Lepora | University of Bristol | Reviewer |
| Abderrahmane Kheddar | Université Montpellier, Country | Reviewer |
| Katherine J. Kuchenbecker | Max Planck Institute for Intelligent Systems | Examiner |
| Christine Prelle | Université de Technologie de Compiègne | Examiner |
| Marc Ramuz | École des Mines de Saint-Étienne | Examiner |
| Michaël Wiertlewski | TU Delft | Advisor |
| Stéphane Viollet | Aix-Marseille Université | Advisor |

# Declaration of Authorship

I, Xi Lin, declare that this thesis titled, "Robotic touch for contact perception: Contributions to sensor design, manufacturing and signal processing" and the work presented in it are my own. I confirm that:

- This work was done wholly or mainly while in candidature for a research degree at this University.
- Where any part of this thesis has previously been submitted for a degree or any other qualification at this University or any other institution, this has been clearly stated.
- Where I have consulted the published work of others, this is always clearly attributed.
- Where I have quoted from the work of others, the source is always given. With the exception of such quotations, this thesis is entirely my own work.
- I have acknowledged all main sources of help.
- Where the thesis is based on work done by myself jointly with others, I have made clear exactly what was done by others and what I have contributed myself.

Signed:

Date: 04/01/2021

AIX-MARSEILLE UNIVERSITÉ

# *Abstract*

Doctoral School: Sciences du Mouvement Humain

**Robotic touch for contact perception:**
**Contributions to sensor design, manufacturing and signal processing**

by Xi Lin

Tactile perception subserves the impressive dexterity found in humans but also found in their robotic counterparts. However, despite their inception in the early 50s, robotic tactile sensors remain rarely seen in commercial and research developments, because their manufacturing is complex, and they often have few sensing points. Recently, a new wave of tactile sensors relying on off-the-shelf cameras, provides a dense tactile image of the contact. However, by the way these sensors operate, the link between the mechanics of the skin and the tactile images is not evident.

In this thesis, we present a novel camera-based tactile sensor, named ChromaTouch, which captures physically-driven dense images of the three dimensional interaction that happens at the interface between the artificial skin and the touched object. The sensor measures the strain field induced by the contact, by imaging the pattern and color change of two overlapping markers array, one translucent and yellow and the other opaque and magenta. The motif seen by the camera is a bijective function of the relative motion of the markers allowing a reconstruction of the stress and strain field at the interface. The sensor, boasting up to 441 sensing elements, shows high robustness to external luminosity and camera resolution, and it is able to estimate the local coefficient of friction of the contact surface with one simple press. A hemispherical version extended the results to arbitrary shapes and is able to estimate the local curvature via a simple press using Hertz contact theory.

Sensing the dense 3d deformation field at the contact opens the doors to a comprehensive, physically-based measurement of the interaction. Improved artificial perception of the object (i.e. shape, compliance and friction) and of the interaction (i.e. partial and full slippage or rotation, and roll) can inform robotic exploration, dexterous grasping and manipulation.

# *Résumé*

La perception tactile sous-tend l'impressionnante dextérité observée chez les humains mais également chez leurs homologues robotiques. Malgré leurs débuts dans les années 50, les capteurs tactiles robotiques restent rarement vus dans les développements commerciaux et de recherche, car leur fabrication est complexe et ils ont souvent peu de points de détection. Récemment, une nouvelle vague de capteurs tactiles reposant sur des caméras du commerce offre une image tactile dense du contact. Cependant, par le fonctionnement de ces capteurs, le lien entre la mécanique de la surface du capteur et les images tactiles n'est pas directe et nécessite un étalonnage.

Dans cette thèse, nous présentons un nouveau capteur tactile, appelé ChromaTouch, qui utilise une caméra pour capturer des images denses physiquement conduites de l'interaction tridimensionnelle qui se produit à l'interface entre la peau artificielle et l'objet touché. Le capteur mesure le champ de contrainte induit par le contact, en imaginant le motif et le changement de couleur de deux couches de marqueurs qui se chevauchent, l'un translucide et jaune et l'autre opaque et magenta. Le motif vu par la caméra est une fonction bijective du mouvement relatif des marqueurs permettant une reconstruction du champ de contraintes et de déformations à l'interface. Le capteur, doté de 441 éléments de détection, montre une grande robustesse à la luminosité externe et à la résolution de la caméra, et il est capable d'estimer le coefficient de frottement local de la surface de contact avec une simple pression. Une version hémisphérique a étendu les résultats à des formes arbitraires et est capable d'estimer la courbure locale via une simple presse en utilisant la théorie des contacts de Hertz.

La détection du champ de déformation 3D dense au niveau du contact ouvre les portes à une mesure complète et physique de l'interaction. Une perception artificielle précise des propriétés de l'objet (forme, compliance et frottement) et de l'interaction (c'est-à-dire le glissement ou la rotation partielle et totale, et le roulis) peut informer l'exploration robotique, la saisie et la manipulation habiles.

# Acknowledgements

Foremost, I would like to express my sincere gratitude to my primary supervisor Michaël Wiertlewski, not only for his enthusiasm and rigorous attitude to scientific study that influenced me deeply, but also for his continuous support and encouragement in overcoming numerous obstacles I have been facing through my research and my life. I would also like to acknowledge Stéphane Viollet for his immense knowledge and insightful discussions that inspired me on my research.

I would like to thank the wonderful engineering team at the Institute for Movement Science: Julien Diperi and Marc Boyron, for their enthusiastic technical assistance and valuable advice on my works and research.

My sincere thanks also goes to my dear colleagues in the Marseille lab: Laurence Willemet, Julien Dupeyroux, Nicolas Huloux, Corentin Bernard, Anna Verbe, Aimie Berger, Ilya Brodoline and Evandro Bernardes, not only for the inspiring discussions during the lunch and coffee breaks but also for those happy hours we have spent in Marseille. I am also grateful to everyone I met at CoR lab of the TU Delft, especially David Abbink, Padmaja Kulkarni, Mohammad Mahdi Shirazi and Rob Scharff, for their help on my thesis.

Besides, I would like to thank my friends Qingfeng Li, Yuan Hao, Xuan Luo, Xifeng Sun, Wei Wang and Qi Wei, without their accompany to the gym, the beach, and the restaurants in Marseille, I could not keep such a healthy state and happy mood during my thesis.

At last but not least, I would like to thank my parents Guizhi Zhang and Jun Lin, for their moral encouragement, as well as their spiritual support in every path I take.

# Contents

# List of Figures

# List of Abbreviations

| | |
|---|---|
| **CNN** | Convolutional neural network |
| **CNS** | Central nervous system |
| **DoF** | Degree of freedom |
| **EP** | Exploratory procedure |
| **HHD** | Helmholtz-Hodge Decomposition |
| **kNN** | k-nearest neighbors algorithm |
| **MEMS** | Microelectromechanical systems |
| **PDMS** | Polydimethylsiloxane |
| **PVDF** | polyvinylidene difluoride |
| **SIFT** | Scale-invariant feature transform |
| **SVM** | Support vector machine |
| **TIR** | Total internal reflection |
| **TLC** | Thermochromic Liquid Crystal |

Chapter 1

# Introduction

## Contents

## 1.1 Background

Automation and robotics permeate every aspect of the modern society, from the most complex industrial applications to helping the general public with daily chores. They are particularly useful for handling menial or dangerous tasks and help us live better lives. This rapid adoption creates a new demand for robots that perform complex operations in dynamic and unstructured environments. The promise of a robot that can safely and intuitively work alongside humans will lead to fundamental changes in our society through application in healthcare, agriculture, human-robot interactions and object manipulations. In particular, one of the central challenge of robotics is to be able to explore, grasp and manipulate arbitrary objects with a human-like accuracy and dexterity. For instructing robots to manipulate with precision and care, we can take inspiration from how humans can easily feel, explore, grasp, and manipulate a wide variety of objects, do complex tasks with high precision such as writing and sewing. The answer to humans' extraordinary dexterity seems to lie in their fine-tuned sensorimotor loop that controls the muscle activation based, in par, on inputs from the sense of touch.

Imagine lighting up a match, one have to just grab the match stick, strike the stick on the match box. This is a simple task that human may perform many times in their life. However, Johansson et al. [75] carried out an experiment, studying the impact of removing the sense of touch on their ability to perform dexterous manipulations. The subject with fingertips anesthetized is asked to light a match. The results were remarkable: subject could barely manage to pick up a match stick and light it up. The simple task, which only took 5 seconds before with sense of touch, became struggling and will take 5 times longer after anesthetization of fingertips. Human's clumsiness in this experiments is similar to the struggles of modern robots when they deal with complex manipulation tasks. Why did taking away the sense of touch have such an impact on human subject?

Human's sense of touch allows direct measurement of the contact through interactions with the external environment. The measurements of contact inform about pressure, friction, compliance, texture, temperature, and other physical properties of objects in contact, which helps create a mental model of the haptic scene. Without this tactile feeling, human hands would be like anesthetized, and manipulation tasks such as lighting a match, will be extremely difficult.

Given the prevalence of touch in human, it is surprising that most of the recent commercial and industrial robots use visual sensing as a substitute of tactile sensing. However, the visual feedback is remote and the view is often occluded by the actuators at the point of contact. Moreover, when robotic hand is in touch with the object, no knowledge of the contact force can be obtained. For a grasping task, the slippage may happen if the object is slippery and the grasping force is too small. The fragile object may risk of being broken if the grasping force is too large. Interactions with objects without tactile sensing hinder the robot from achieving dexterous manipulation in unknown environments.

In this context, implementation of tactile sensors onto robotic grippers have become an essential step towards human-like manipulations. Tactile sensors began to develop in the 1970s and now play an important role in various domain. The increasing requirement of tactile information in various technical systems, such as robotic hands, medical equipment, touch screen on smart phones, leads to the appearance of diverse tactile sensing technologies. Nowadays, the development of tactile sensing technologies becomes a trend. Various tactile sensors with different modalities have been designed and studied. Several tactile sensors are now commercially available.

## 1.2 Problem statements

The importance of tactile sensing has long been well acknowledged in the robotics community as substantial advances in tactile sensor technology began from 1980s. However, despite the fast advancement in tactile sensing technologies, artificial tactile sensors aiming at robust dexterous manipulation still need much improvements to achieve the capabilities of human beings. Exploiting the sense of touch in robots remains challenging after almost 50 years of research.

First of all, the tactile sensing technology has been largely limited to sparse pointwise measurements, which falls far away from the rich tactile feedback of human skin. The density of human's mechanoreceptors on the fingertip can reach around 250 units/cm$^2$ [76], which offer an extremely dense sensing array comparing with the palm where the receptors' density is only around 58 units/cm$^2$. Moreover, these mechanoreceptors respond to various stimuli such as normal force, shear force, light tapping and vibrations. The sense to shear is also proven important to detect slippage [11]. However, most commercially available tactile sensors either lack of dense measurement, or cannot measure both normal and shear stresses.

Second, many recent tactile sensors focus on measuring one single contact information, which is not enough for acquiring a complete view of the object in touch for dexterous manipulation. For example, many tactile sensors are only able to measure one directional force or deformation. However, it was proved that shear information is as important as normal information because it can be used for detecting friction to prevent slippage.

Finding the adequate method to process and interpret the tactile data for robotic control could be a third challenge. Using tactile feedback has been proven to be useful in robotic hand control. However, almost all the off the shelf robotic hands employ only vision or single point force sensor to perform manipulation tasks. A few solutions employing tactile sensors but lack of sensing capabilities [9, 155, 160]. The implementation of tactile array in robotic control loop remains computationally costly.

In order to design and develop a tactile sensor suitable for dexterous manipulation tasks, one should answer the following questions.

- **How to measure relevant tactile cues?** The interaction between tactile sensors and objects is complex. Contact information involves various modalities including normal and shear forces, 3d deformation, vibration and slippage. Force and deformation indicate whether the object is in contact, and how much is the contact force. The vibration may indicate the texture and roughness of the contact surface. The slippage measurement enables the robot to increase the grip force to prevent objects from dropping. The measurements of contact information are usually achieved by transducers that convert mechanical touch to different types of signals including electrical, magnetic, optical, and even acoustic signals. Analyzing the converted signals allows the estimation of different contact information. The combination of all the tactile modalities may even provide a more complete understanding of the contact. A tactile sensor should be able to measure tactile information which infers the contact conditions.

- **How to extract contact information and object properties from measurements?** In general interactions, objects could have arbitrary shape, friction, compliance and other physical properties. For objects with different physical properties, different manipulation strategies should be employed for robot to execute appropriate actions. The interaction information such as contact force and slippage should also be detected to ensure a robustness of the action. For fragile objects, the grasping force should be suitable for holding the object whilst not damaging it. For slippery objects, the grasping force must increase to avoid slippage.

For objects with complex shape, the robot must know where is the optimal position to perform the most stable grasp. The knowledge of the object properties, which could be extracted from the contact information mentioned above, may guide humans to properly manipulate no matter which kind of objects. For example, the measurement of deformation and stress distribution are usually used for shape and edge detection. The vibrations can be used for slippage detection. The ratio of normal and shear forces applied on the object leads to the coefficient of friction of the contact. Therefore, the tactile sensor should be able to extract various object properties from the contact information in order to adapt manipulation tasks on different objects and in unknown environments.

## 1.3 Research objectives

Aiming to solve the problem of existing tactile sensors and satisfy the requirements in tactile sensing, the two main goals of this thesis are:

- First, to design an artificial tactile sensor that is able to measure both normal and lateral deformation or force. Additionally, the sensor should have a high spatial resolution with dense measuring elements and could be mounted onto robots for manipulation tasks. For achieving this goal, the camera-based tactile sensing method is employed. The detailed rationale of the camera-based sensor design is explained in section 3.1. Several different prototypes were manufactured to improve the sensor design. A testing platform was set up to calibrate and test the proposed sensor.

- Second, to use the sensor to measure contact information and extract properties of the object in touch. In this thesis, we focus on measurements of sensor's deformation due to contact, estimations of the curvature of the object, and also estimations of the friction between the object and the sensor. Objects with various shapes and frictional state will be used to test the tactile sensor. The frictional state can be quantified by the coefficient of friction and is related to the frictional properties (e.g. slippery, rough). Sensor's ability to measure different contact information and object physical properties will be evaluated.

## 1.4 Thesis overview

This thesis is organized as follows:

**Chapter 2** provides a literature review of studies on tactile sensing in the context of improving robotic manipulation. The functionality of humans finger is reviewed to provide an overview of how humans sense touch. Various tactile sensors and tactile sensing technologies are then reviewed to introduce how do tactile sensors transduce touch to other processable tactile signals. Tactile perception is also reviewed to show methods for extracting useful tactile signals and interpreting the tactile data to contact conditions and object properties. Robot actions regarding various perceived tactile information is further detailed at the end, including exploration, grasping and manipulation.

**Chapter 3** presents the first version of a camera-based tactile sensor named ChromaTouch. The design and manufacturing of the sensor are described. A sensing method using color mixing principle is proposed and evaluated. With this new sensing design, the sensor is able to estimate the normal displacement map by calculating the color change induced by the deformation of the sensor. Advantages and limitations of this method are discussed in this chapter.

**Chapter 4** presents the second version of the ChromaTouch sensor which comes in a hemi-spherical shape. The sensor is designed for robotic use and is mounted onto a robotic arm. The advantages of spherical sensor is discussed. The sensor is able to estimate the curvature via a simple press. The algorithm for curvature estimation using the hemi-spherical sensor is tested and evaluated.

**Chapter 5** presents the third version of the ChromaTouch sensor with a much higher spatial resolution, which has 441 sensing elements of 1 $mm^2$ in size, comparing to the first and second version with only 100 and 77 sensing elements. Instead of calibrating the sensor using color change as presented in chapter 3, the calibration of this sensor is acheived using convolutional neural network, which is proven to be more accurate and robust comparing with the first version. With the high spatial resulotion, this sensor can distinguish the difference of frictional condition on the same contact area by a simple press.

**Chapter 6** concludes the thesis by summarising the different versions of the tactile sensor, the progression of the signal processing algorithms, as well as the contributions of this thesis and possible future studies building on this work.

Chapter 2

# State of the art

## Contents

TACTILE sensors provide rich information on the contact condition and object properties. Comparing with traditional robots that use only visual feedback, robots equipped with tactile sensors not only see, but also feel the objects, which improve robotic grasping and manipulation. This chapter reviews the literature from the design of tactile sensors to the use of tactile feedback in robotic control. This chapter is divided into the following three sections:

– **Transduction:** Various tactile sensing designs using different transduction methods are presented in this section, as the transduction from mechanical touch to processable tactile signal is the first step of tactile sensing. After a presentation of humans' tactile sensing system, two main transduction methods are reviewed including electromechanical and camera-based transduction.

– **Perception:** Tactile perception refers to extracting information of objects and contact from raw tactile signals. This section introduces how humans perceive objects and interactions, and then reviews the literature for the robotic perception of object properties and interactions.

– **Action:** This section presents the state of the art of robotic actions employing tactile sensing. The literature review in this section shows the control of robotic exploration, grasping, and manipulation tasks using the contact information extracted from the tactile signals as feedback to improve the dexterity of the robotic hand.

Figure 2.1 shows the relation between robot-object contact, tactile transduction, tactile perception, and robotic action, where tactile sensor plays an essential role to link the contact and perception.

## 2.1 Transduction: Encoding mechanics

At its core, a tactile sensor transduces mechanical interactions into signals that are interpretable by a digital controller. From the past 30 years, a plethora of tactile sensors have been invented using all the possible transduction techniques, such as capacitive, piezoresistive, piezoelectric, magnetic, and optic. The objective of all these transduction methods is to convert mechanical contact to another form of signals. Reading and analyzing the converted signals allows the estimation of the object property, such as shape, texture, softness, and contact information, such as slippage, force, deformation.

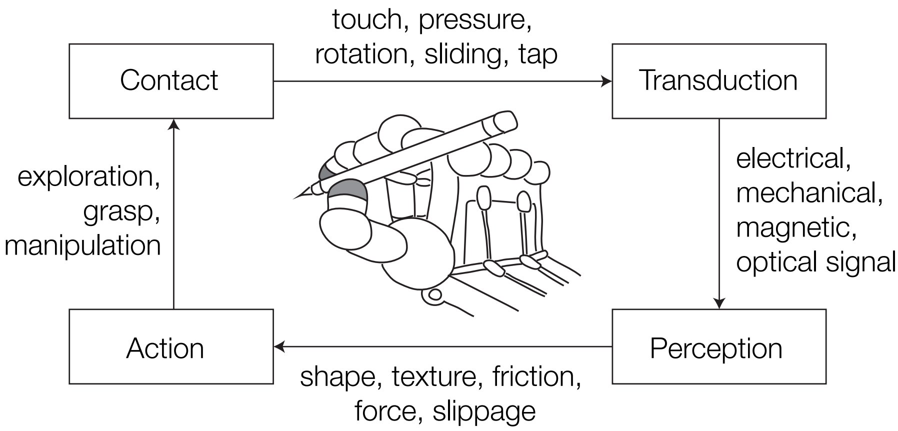


FIGURE 2.1: The relation between robot-object contact, tactile transduction, tactile perception, and robotic action

### 2.1.1 Human sense of touch

Humans sensitivity to tactile stimuli provides a gold standard for designing artificial tactile sensing abilities in robots. Human skin is an essential sensory system that allows sensing of contact, pressure, shear, temperature, vibration, and pain. The skin is composed of two primary layers: epidermis and dermis. The dermis transmits tactile information due to mechanical, thermal, or chemical stimuli [34].

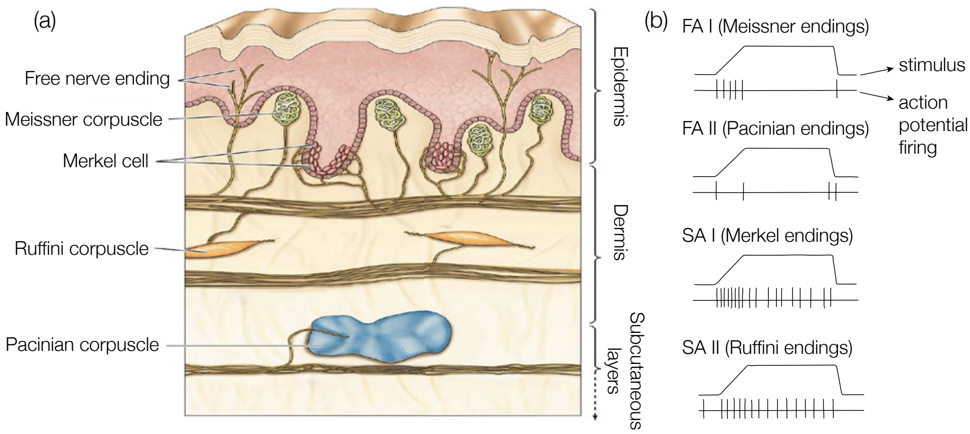


FIGURE 2.2: Mechanoreceptors in human's skin

Among all the skin areas, the glabrous skin of the hand is one of the most sensitive to tactile stimulation. Most of the nerve endings are embedded in the dermis of the glabrous skin. Some of these nerve endings function as nociceptors and detect pain, while some function as thermoreceptors and detect temperature. The mechanoreceptive afferents are relative to mechanical stimuli such as pressure, shear, vibration, and stretch [74]. They are mainly divided into four types: fast-adapting type I (FA I, Meissner corpuscles) and fast-adapting type II (FA II, Pacinian corpuscles), slowly-adapting type I (SA I, Merkel's cells) and slowly adapting type II (SA II, Ruffini endings) [75]. Meissner corpuscles and Merkel's cells are located toward the surface of the skin, and the other two are located deeper (Fig.2.2a). Each kind of receptor has their specific adaptation rate and perceptive field. The afferent neurons convert specific types of stimulus, via their receptors, into action potentials that propagate towards the CNS (Central nervous system). As shown in Fig. 2.2b. The slowly-adapting receptors generate continuous action potentials from the time the stimulus is applied until it is removed [178]. Merkel cells detect pressure and can sense the shape of the object. They have small receptive fields and produce sustained response to static stimulation. Ruffini endings respond to force and direction of skin stretch. They also produce sustained responses to static stimulation but have a large receptive field. In contrary, the fast-adapting receptors generate a burst of action potentials at the moment when stimulus is applied and when the stimulus is removed [178]. Meissner corpuscles deal with the low-frequency vibrations, slip and light touch on the skin. They have small receptive fields and produce transient responses to the onset and offset of stimulation. Pacinian corpuscles detect high-frequency vibration and are responsible for the perception of surface textures. They respond to rapid mechanical changes, an have large receptive fields.

Table 2.1 shows a summary of the mechanoreceptors and their corresponding afferent types.

| **Receptor** | **Detection** | **Adaptation rate** | **Location** | **Receptive field** |
|---|---|---|---|---|
| Pacinian corpuscles | high frequency vibration (100-300Hz) | rapid (FA II) | deep skin | large |
| Meissner's corpuscles | slip and light touch, low frequency vibrations (20-40Hz) | rapid (FA I) | superficial skin | small |
| Ruffini endings | force and direction of skin stretch | slow (SA II) | deep skin | large |
| Merkel cells | pressure and form of the object | slow (SA I) | superficial skin | small |

TABLE 2.1: Summary of the characteristics of human mechanoreceptors

Human mechanoreceptors are highly sensitive to a wide range of stimuli and researchers have attempted to replicate the performance of the human mechanoreceptors using a large variety of artificial tactile sensors. However, due to the complexity of the human sensory system, the development of the human-like transduction system still proves to be a major challenge for research and industry.

Despite the fast advancement in tactile sensing technologies, artificial tactile sensors aiming at robust dexterous manipulation still needs many improvements to achieve the capabilities of human beings.

### 2.1.2 Electromechanical transduction

Electromechanical transductionis achieved by taking advantage a host of physical phenomena such as piezoresistivity, electrtical capacitance, or piezoelectricity. Pressure sensing arrays are built by arranging multiple individual sensing cells in columns and rows. Building with soft layers, some sensors can be thin and stretchable. Thus the electromechanical transduction technologies are widely used to manufacture touch-sensitive skin.

#### Piezoresistive

The piezoresistive sensors transduce force variation into changes of resistance. The special material used for manufacture piezoresistive sensors react to deformations by changing its resistance.

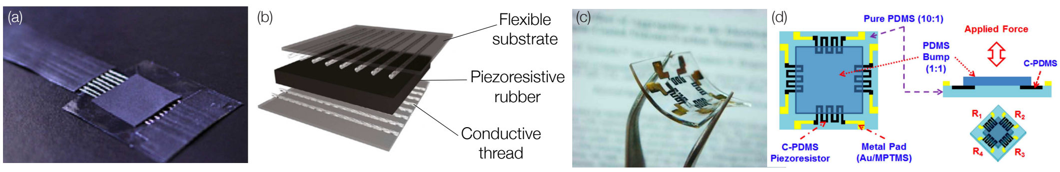


FIGURE 2.3: (a) A piezoresistive sensor proposed by [42] and (b) its structure. (c) A piezoresistive sensor [183] using carbon-based fillers for conductive layer, and (d) its structure.

Using strain gauges is a typical way to measure contact force in MEMS (Microelectromechanical systems) piezoresistivitive sensors. However, the lack of flexibility is the major drawback of rigid gauges. In recent years, because of the advancement in the fabrication of microstructures and nanomaterials, piezoresistive rubber made by mixing non-conductive polymers and distributed electrically conductive nanoscale fillers becomes the most used material in piezoresistive sensing [42, 16]. There are two widely used conductive fillers for piezoresistive tactile sensor: metal-based and carbon-based fillers. However, the difficulties in bonding metallic particles and polymers into a thin layer limit the application to soft electrical skin. The carbon-based fillers usually consist of carbon nanotubes (CNTs) [157, 183] or graphene nano-sheets [22, 5], which influence the mechanical and electrical properties of the sensor [54].

Piezoresistive sensors can be flexible, thin, and robust to noise. They are also relatively simple to manufacture. Thus many commercial solutions exist for robotic applications, such as Inaraba and Eeonyx. Nevertheless, the lack of reproducibility as well as the hysteresis remain the most considerable drawbacks of piezoresistive sensing technology.

### Capacitive

Capacitive tactile sensors vary the capacitance by changing the geometry of their capacitors. The most common structure of a capacitive tactile sensor consists of two parallel conductive plates separated by a compressible dielectric material. The capacitance is changed when the distance between the two plates changes because of the pressure applied onto the dielectric layer.

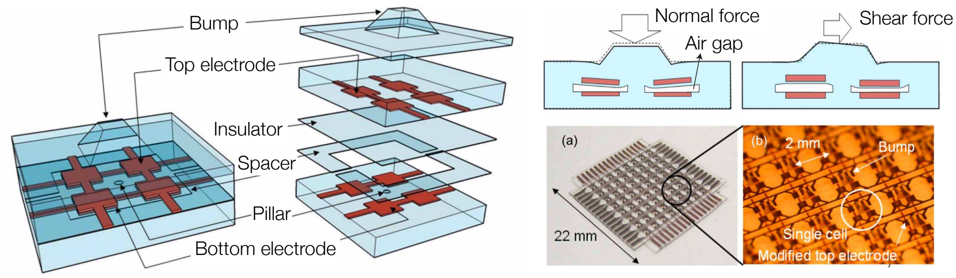


FIGURE 2.4: A capacitive tactile sensor capable of measuring both normal and shear stress [96]

Capacitive sensors can detect both normal and shear forces by embedding four electrodes in one unit and measuring the difference and co-effect of the four sensing cells [96]. The dielectric layer between the electrodes is usually made of flexible PDMS. The sensitivity of the capacitive tactile sensor can be increased or tuned by patterning the dielectric layer [156, 121]. There are also some other dielectric layer designs that can increase the sensitivity to small forces applied on capacitive tactile sensors, such as using air gaps [138], and liquids [1].

Because of the high sensitivity, high resolution, and large dynamic ranges, capacitive sensing is very popular among the tactile transduction technology. However, the hysteresis, the susceptibility to electromagnetic noise, and the sensitivity to temperature remain the main disadvantages of capacitive tactile sensors.

### Piezoelectric

Piezoelectric sensors are made of piezoelectric materials, which generate electrical charges in response to deformation applied by force or pressure.

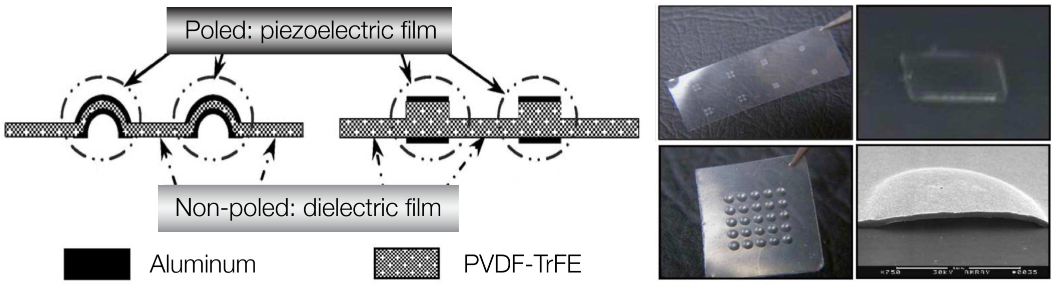


FIGURE 2.5: A piezoelectric tactile sensor using PVDF film presented by [102]

The piezoelectric layer is usually embedded between two electrodes on a soft substrate [200]. When pressure is applied to the sensor, the piezoelectric layer will be compressed, which converts its deformation to an electrical charge. Zinc oxide (ZnO) [7] and poled ceramic lead zirconium titanate (PZT) [92] are popular materials for making rigid sensing elements. Flexible sensing structures can be achieved by distributed nano particles. Polyvinylidene fluoride (PVDF) is the most widely used material to make the flexible piezoelectric layer [102, 109].

Piezoelectric sensors are highly sensitive to dynamic pressure with a frequency range of 1 Hz to 1 kHz, and they exhibit fast response speed [158]. Due to this advantage, they can be used to measure the vibrations associated with slip [31]. In spite of there impressive sensitivity, piezoelectric tactile sensors are not suitable for the measurement of static contact forces because the induced charge in piezoelectric materials dissipates very quickly in the sensing resistance. The sensitivity to temperature is also one of the main drawbacks of piezoelectric materials.

### Magnetic

Tactile sensors based on magnetism measure the change in magnetic flux or magnetic field density as a result of the applied force by the magnetic sensor such as Hall effect sensor [175] and giant magneto resistance (GMR) sensor [51]. Magnetic tactile sensors are usually constructed by embedding pairs of magnets in an elastomer body. The deformation of the elastomer changes the position of the permanent magnet, which leads to variation in the magnetic field. The direction and magnitude of the applied force can be then estimated by measuring the change of magnetic field [95, 137]. However, the size and spatial resolution are limited for this kind of design. Another kind of tactile sensor uses a magnetic nanocomposite hair-like cilia. The deflection of cilias caused by external force leads to changes in the magnetic field, which can be detected by a magnetic sensor. The flexible hair-like structure of the sensor resulting in high sensitivity to small surface texture changes [181, 2].

Magnetic tactile sensors exhibit physical robustness, high sensitivity, good dynamic range, and it has no measurable mechanical hysteresis. However, they can only be used in nonmagnetic environments.

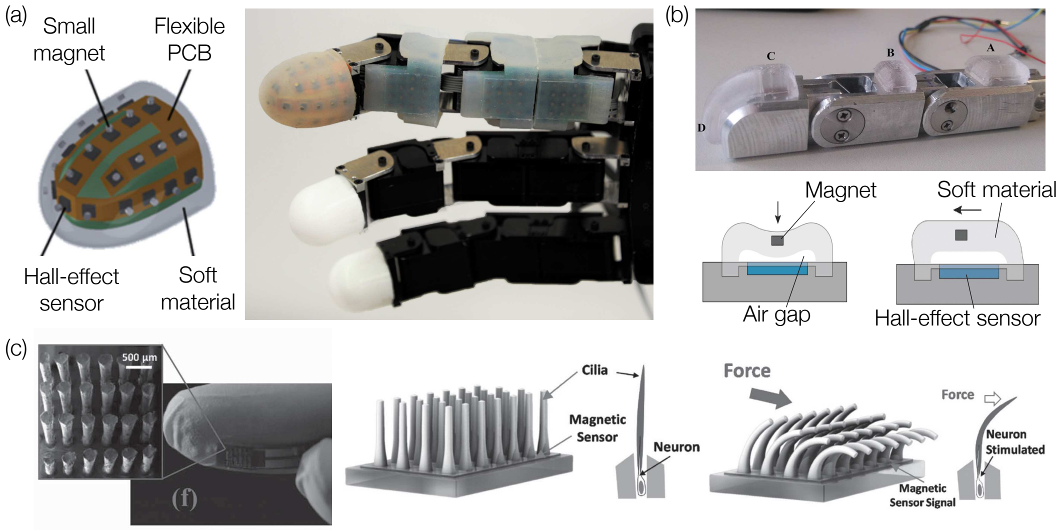


FIGURE 2.6: (a) A tactile sensor employing arranged magnetic transducers for robotic hand proposed by [175] and its structure. (b) A low-cost tactile sensor using hall effect [137] and its working principle for measurement of shear and normal force. (c) Structure and working principle of a hair-like magnetic tactile sensor for measuring surface texture [2].

### Multi-modal tactile sensors

Human hands have various types of tactile sensing modalities. The implementation of multi-modal tactile sensors allows the robots to match human's tactile sensing ability as much as possible.

BioTac is one of the multi-modal tactile sensors that are commercially available and widely used in research. It's a finger-shaped tactile sensor that can measure the contact forces, vibrations, and temperature produced during contact with an object [48]. Cranny et al. also proposed a tactile sensor for a prosthetic hand that provides slip, temperature, and force information [33].

The sensor developed by Mittendorfer et al. is able to provide whole-body-touch sensation using connected multimodal tactile modules named HEX-O-SKIN. It is a small hexagonal printed circuit board equipped with multiple discrete sensors that can measure temperature, acceleration, and proximity [124]. Kampmann et al. presented a three-fingered robot gripper that incorporates strain gauge sensors, piezoelectric sensors, and fiber optic sensors to measure absolute the dynamic forces and the force distribution, respectively [86]. Viola et al. reported a multimodal temperature and force sensor by using an ultrathin PVDF film, which has both piezoelectric and pyroelectric properties [180]. Recently, Yu et al. proposed a vision based multi-modal tactile sensor. The black and white grating pattern of the soft sensor allows the measurement of distributed pressure via Fourier Transform Profilometry. The whole sensing surface is covered with a Thermochromic Liquid Crystal (TLC) ink layer that changes color when temperature changes [199]. Another vision based multi-modal tactile sensor, named MultiTip was introduced by Soter et al [167]. By adding thermochromic powder in the sensing skin, the sensor is able to measure both temperature changes and deformation due to the contact.

Multi-modal sensors have the ability to sense different tactile features at the same. However, when a large number of modalities is integrated into the sensor, the reduction of sensor size becomes a main issue to solve.

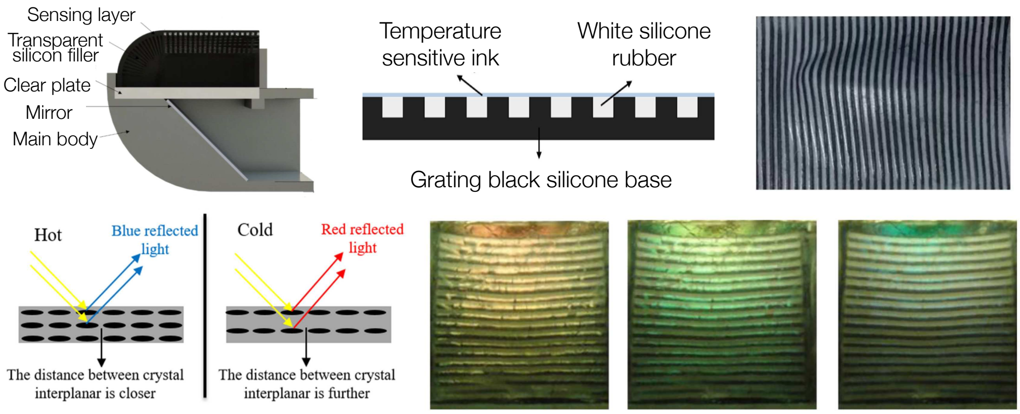


FIGURE 2.7: The structure and working principle of the multimodal tactile sensor proposed by [199] capable of measuring pressure and contact temperature.

### 2.1.3 Camera-based transduction

Tactile sensors based on electro-mechanical transduction could have a high sensibility and high dynamic range. However, the fabrication is complex if high spatial resolution is desired in such sensors due to the requirement of bulky sets of electrical interconnections. To obtain a high-resolution tactile sensor with simple manufacturing, employing a camera in the sensing system became a practical solution. The use of the camera in tactile sensors appeared for more than 30 years. Since then, more and more studies have focused on developing camera-based tactile sensors.

The transduction from tactile contact to vision problem benefit from the high resolution provided by the camera embedded in the tactile sensor. Because of the recent development in imaging technology, the use of mini camera becomes inexpensive and convenient. In addition, with the recent development of computer vision and machine learning, image processing becomes much easier and faster for real-time camera-based tactile sensing. Moreover, the camera and soft skin could be isolated, which leads to physical robustness. The shape of the sensor could also be more flexible. Due to all the above advantages, employing a camera into the tactile sensor is becoming a trend in recent years. Nowadays, the camera-based tactile sensors begin to appear not only in research but also for commercial use [50, 182, 29].

A camera-based tactile sensor is generally composed of two parts: the camera for imaging and the soft skin for contact. The camera captures images or videos according to different sensing needs. Different camera lenses can be used to control the angle of view to satisfy different requirements in the measurement area. The contact part is usually made by soft skin that converts mechanical tactile contact into light signals that can be captured by the camera. Most of the existing camera-based tactile sensors achieve the conversion from contact to light by using total internal reflection, embedded markers, or reflective skin.

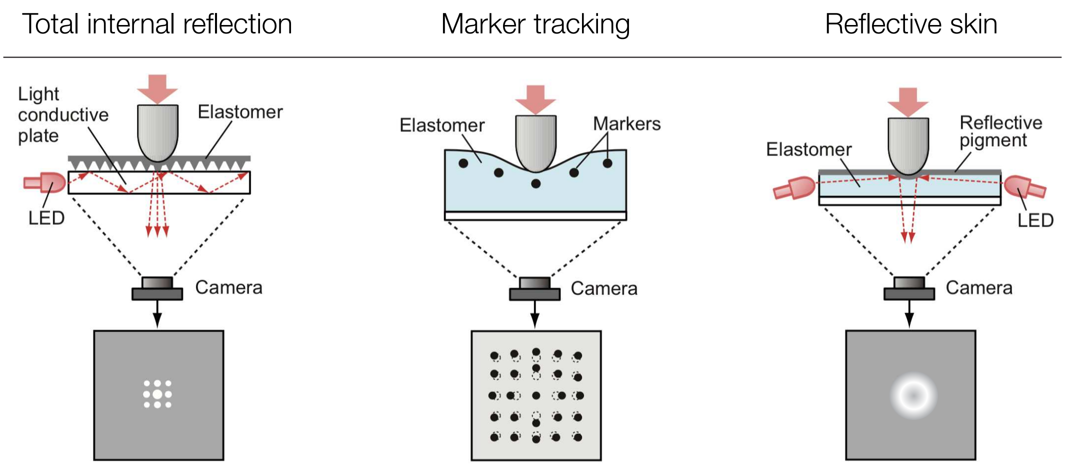


FIGURE 2.8: Three main methods for camera based tactile sensing [164] using total internal reflection, marker tracking, and reflective skin.

### Total internal reflection

The tactile sensing using total internal reflection (TIR) employs a light conductive plate. Various solid transparent materials can be used as the light conductive medium such as glass, acrylic plate, and elastomer. LED lights are introduced into the light conductive medium and will be reflected only inside the medium when the angle of incidence is larger than the critical angle. This phenomenon is called total internal reflection. If contact is made onto the transparent medium, the reflected light on the area of contact will be scattered. The intensity and size of the scattered light spot related to the contact force will be captured by the camera.

This method is used in many early studies of camera-based tactile sensing. In 1984, Scheiter and Sheridan designed and built a planar tactile sensor using the total internal reflection principle. The sensor consists of a flexible material covered by a white silicon rubber to reflect light. Two sets of optical fibers are embedded in the sensor to send light and capture images. The pattern generated by the reflected light can be used to detect slip and orientation of the object by calculating the centroid and moments of inertia from the image difference before and after pressure. The sensor design allows for extremely high spatial resolution as it has 2100 sensitive spots per inch$^2$ [154].

Tanie et al. developed a similar planar tactile sensor in the same year [172]. The sensor is constructed by a transparent acrylic plate and an elastic sheet. The elastic sheet under pressure leads to an increase in the size of the contact area. Lights on the region in contact are reflected. Instead of using optical fiber, a photo-transistor was employed as the imaging system. The photo-transistor captures the change of light to detect the pressure. Later on, Hiraishi improved the sensor by replacing the photo-transistor with a CCD camera, which largely increased the resolution of the sensor [55]. Then from 1990 to 1992, Maekawa developed three spherical versions of tactile sensors based on Hiraishi's planar one. The last version only has a finger-shaped size with 20mm in diameter and 44mm in length [128, 118, 116, 117].

Another TIR based tactile sensor was reported by Begej et al. in 1988 [10]. They manufactured a planar and a finger-shaped tactile sensor using TIR principle. The sensor uses plastic fibers to capture the tactile imprint. The latter was then transported to a remote display array. The sensor under pressure produces a gray-scale image that indicates the normal force of the contacted object.

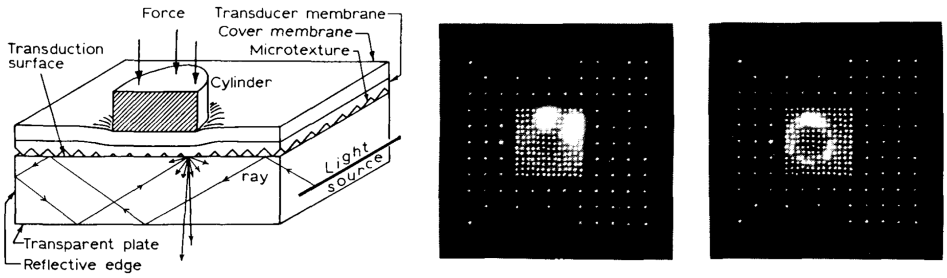


FIGURE 2.9: Tactile sensors using total internal reflection principle by [10], which use an elastic skin with irregular surface structure to scatter lights. The lighter region indicates where the sensor is under pressure.

### Marker tracking

Another popular method using the camera for tactile sensing is to track markers in/on a soft body. The typical structure of the sensor using marker tracking is made of several arranged markers embedded inside a transparent elastomer. When the elastomer is in contact with an object, the displacement of the markers under the deformation of the soft body is captured by the camera, which indicates the information of the contact force [177, 130, 69, 53, 146, 159].

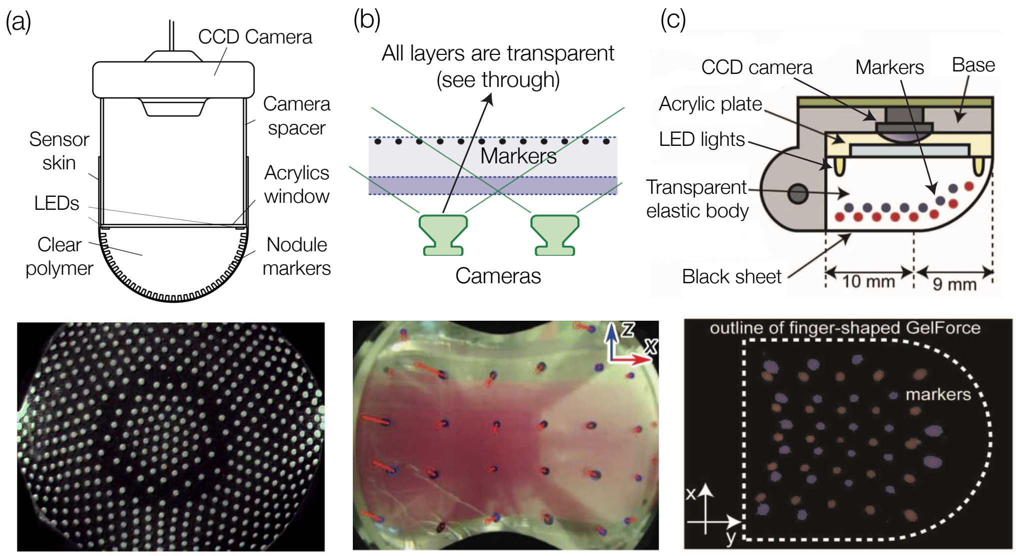


FIGURE 2.10: Tactile sensors using marker tracking methods: (a) Tactile sensor sensitive to edges and corners [26]. (b) Transparent tactile sensor presented in [196] capable of seeing the external scene. (c) Gelforce sensor with double layers of markers for measuring 3d forces [148]

In 2000, Hiristu et al. manufactured a finger-shaped tactile sensor covered by a dotted membrane [63]. The sensor has a metal housing to hold the camera and the transparent window. The inside of the sensor was filled with transparent gel to act as a sensing area. The deformation of the dots is collected by the camera and is used to reconstruct the shape of the membrane.

In 2001, Kamiyama introduced a camera-based tactile sensor [84] named GelForce. The sensor was made of a transparent elastomer embedded with two layers of spherical markers in different colors. 3D force vectors can be calculated from the spatial distribution of the double layers of markers. A detailed evaluation of the GelForce sensor was reported in 2004 [83]. Later on, the sensor was miniaturized into a finger-shaped version by Sato et al. [149]. The implementation of the finger-shaped sensor on a robotic hand was presented in [148].

Another popular camera-based tactile sensor was introduced in 2009 by Chorley et al. [26] in Bristol Robotics Lab. The sensor was made by a transparent gel covered by a papillae-shaped skin taking inspiration from the papillae structure in humans' fingertips. The markers are located on papillae nodules, which are proved to amplify the signal for edge and corner detection. This sensor was later improved and named as TacTip in 2012 [193]. Later, the manufacturing of the sensor was simplified using 3D printing technology [186]. The addition of a biomimetic fingerprint on was proved to be able to improve the sensibility of the sensor [32]. Based on the hemispherical version, Ward-Cherrier et al. developed two versions with different sensor shapes that are implemented in robotic grippers for operating manipulation tasks [185, 184]. Various tactile sensing applications were developed using Tactip sensors, including global slip detection [73], incipient slip detection [72], contour following [99, 101], pose estimation [100], and implementation on 3-fingered robotic hand for grasping [71].

Both GelForce and TacTip sensors make use of an opaque membrane to cover the transparent elastomer in order to block the light from outside. In 2016, Yamaguchi developed a new soft tactile sensor without covering opaque layer. The cameras can see the external scene through the skin. Thus this sensor is able to measure the lateral displacement field by tracking the markers in the elastomer, and can obtain visual information of grasped objects for slip detection [196].

Moreover, Lin and Wiertlewski developed a new tactile sensor in 2019. A layer of semi-transparent yellow markers and a second layer of opaque magenta markers are arranged and overlap in a transparent elastomer. The shear and normal deformation can be calculated by subtractive color mixing when the markers show blends of colors depending on the displacement of the markers [106].

### Reflective skin

Tactile sensing based on reflective skin is widely used in recent studies. The sensor is generally composed of a transparent polymer covered by a reflective membrane. The light introduces by LEDs is reflected by the membrane. When the object is pressed against the sensor, the deformation of the membrane leads to a shading image on the reflective skin due to light reflection. This shading image can be captured by the camera, and then used to compute the contact information.

In 2009, Johnson and Adelson developed a new tactile sensor named GelSight using the reflective skin, which is one of the most popular tactile sensors today. Since then, reflective skin becomes a widely used method for tactile sensing. The first version of GelSight was introduced as a retrographic sensor that can be used as a 2.5D scanner to measure the shape of the object [79]. The sensor is composed of a transparent elastomer sheet coated with a reflective skin. 3 LED lights in red, green, and blue color are located in a circle with an angle of 120 degrees between each other that illuminates the reflective skin. When the object is in contact with the sensing, the elastomer surface deforms, and a shading image reflecting these deformations appears in the image obtained from the camera, which can be used to estimate the shape of the objects. Later on, following the development of robotics and computer vision, different sensor designs and various tactile sensing applications based on GelSight sensor were developed for robotic use. In 2011, a portable version was reported by Johnson et al. [80]. In 2013 and 2014, a finger-shaped version and a hemispherical version were designed by Li et al. [104, 105]. In 2015, Yuan et al. improved the sensor by adding markers onto the reflective skin in order to detect shear and slip [204]. In 2018, a flat version named GelSlim was designed by Donlon et al. [40] based on Gelsight that used only white LED light to form reflected shading. Markers were added onto the reflective skin of Gelslim by Ma et al. in 2019 for measuring the 3d force vectors applied onto the sensor [115]. Recently, Romero et al. integrated the Gelsight sensor on a robotic hand that acts as soft fingertips for carrying out different manipulation tasks [145].

### Others

Besides the common methods mentioned above, there also exist several camera-based tactile sensors that use different technologies to measure the object in contact. For example, the work of Baimukashev et al. proposed a tactile sensor that measures contact force using the color change of a pigmented

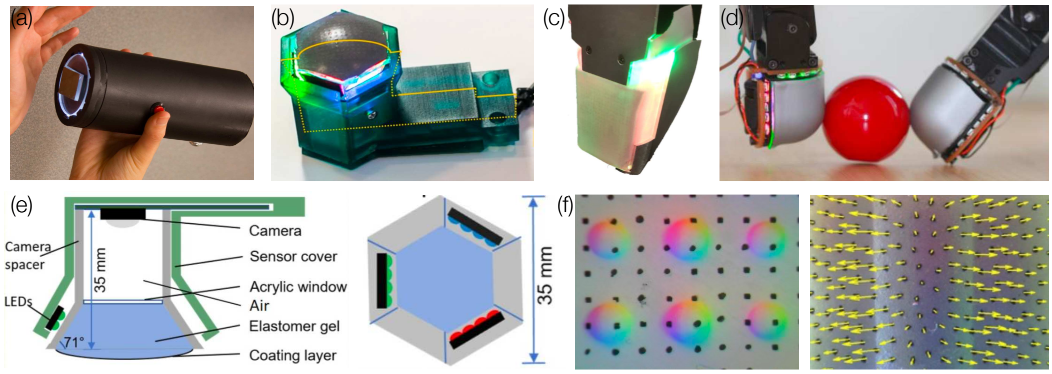


FIGURE 2.11: Gelsight sensors using reflective skin: (a)-(d) Different sensor design. (e) Basic structure of the sensor. (f) Tactile images obtained by the sensor

polymer due to the decrease in the thickness at the point of contact [6]. Zhu et al. also proposed a camera-based tactile sensor capable of detecting contact information using the color-changing principle of butterfly wings [209]. Bioinspired gratings similar to the micro-structure of Morpho menelaus were fabricated onto the surface of a transparent elastic film. The contact force applied on the film leads to angle change of diffracted light. The diffraction pattern on the film captured by the CCD camera predicts the location and magnitude of the contact force.

In conclusion, the first step to perceive the mechanical interaction is to make the transduction of the mechanical state of the artificial skin into signals. This transduction is an essential step in tactile sensing, which can be done via various methods. Electromechanical transductions may suffer from the complex manufacturing, cumbersome set of electrical interconnections, or conditioning electronics. In contrary, camera-based transduction allows tactile sensors to obtain high-density distributed tactile information with a simple structure.

## 2.2 Perception: making sense of the mechanics

After the transduction of mechanical touch to various tactile signals, robots could achieve the tactile perception of object properties and interaction information by interpreting the converted tactile outputs. According to the desired function of the robot, three types of information are most commonly extracted from the tactile data: object shape properties (including curvature, edge), object material properties (including softness, friction, surface texture), and interaction information (including forces, slippage).

### 2.2.1 Human perception

The contact between finger and object activates human's mechanoreceptors to provide inputs into the computation of object properties. Different contact motion activates different types of mechanoreceptors [178, 78].

For example, texture and roughness are measured by lateral movement of the finger over a surface. The lateral motion moves the skin tangentially, which enhances the responses of SA I mechanoreceptors for coarse roughness perception. The deep micro-vibrations caused by finger sliding activates the FA I and FA II units for finer roughness perception. These two neural systems are both used to compute the surface roughness and detect slippage.

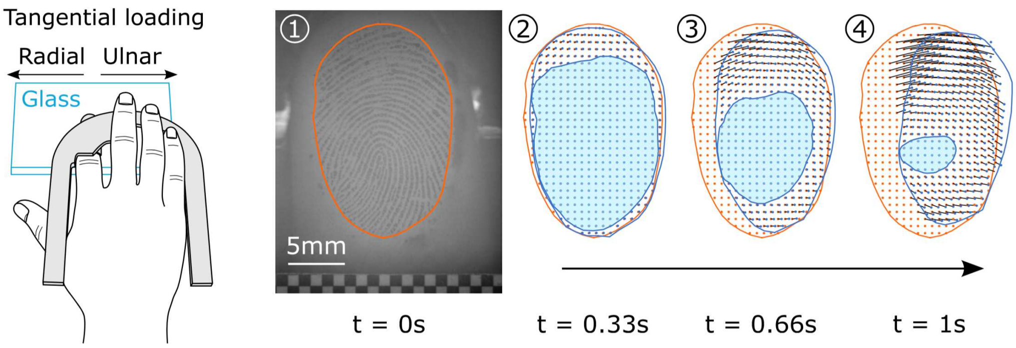


FIGURE 2.12: The incipient slippage of human fingertip under tangential load [8]

In addition, humans are able to detect the slippage before any relative motion between fingers and touched objects [8]. When the finger is sliding on a surface, the slippage does not happens suddenly but propagate from the edge to the center of the contact area. This incipient slippage can be perceived by human's extraordinary sense of touch, which allows human to adjust the grip force rapidly to prevent object from dropping during grasping and manipulation. Fig. 2.12 shows the incipient slippage of human fingertip under tangential loading. Johansson et al. [74] have shown that, 100ms before lifting an object, (so before that any tangential traction develops), humans already start to adjust their grip force according to the frictional properties. Thus, perception of friction will be possible in static, and this has recently been proven by Willemet et al. [192]. They found that by simply pressing the finger onto a surface, the skin stretch skin may also indicates the frictional properties of the contact surface without any lateral motion.

For the perception of stiffness, the contact area between the finger pad and the target object seems to be an important cue [131]. The contact area may be related to the activation of SA receptors sensitive to force and pressure. SA units are also in charge of sensing the curvature, edge, corner, and protrusion, while active exploratory motions such as contour following, are usually used for obtaining a complete knowledge of the global shape of the object. Human's exploratory motion for object perception will be reviewed in section 2.3.1.

Overall, how humans achieve the perception of object properties and interaction information using the sense of touch may inspire the development of tactile sensing methods [36].

### 2.2.2 Robotic perception of shape

Object shape perception refers to the ability to identify and reconstruct the shape of the object in touch with the sensor. This capability is essential for robotic grasping and manipulation tasks. For example, for a grasping task of a vase as shown in figure 2.13, the concave part of the vase would be a more stable grasping location because the gripper can have a larger contact area. The complete knowledge of the object shape allows the robot to better plan and execute stable and robust actions.

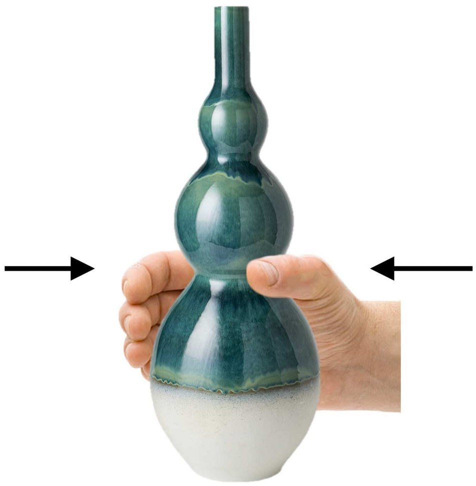

FIGURE 2.13: Concave part of the object for a more stable grasp

The object perception in today's commercial robots is usually achieved by vision. However, the vision-based perception is not possible when the object is occluded by the robotic hand or when the environment is too dark. The tactile sensor is more suitable in this situation to perceive object shape through the sense of touch.

The shape perception involves the local shape and the global shape of the object in contact. The local shape includes curvatures, edges, corners of a part of the object at the contact region. The global shape refers to the complete shape of the object, which is usually measured with tactile exploration.

### Local shape perception

For traditional single point tactile sensors, the local shape of objects can be estimated by combining the contact position and the surface normal during active exploration [126, 23].

In recent years, with the development of tactile sensing technologies, the pressure distribution measured by the tactile sensor with high spatial resolution can serve as a tactile image. Various methods were proposed to extract the object geometry information from the tactile images.

In some research, the normal strain distribution of the contact surface can be approximated with a second-order polynomial equation [44] or a Gaussian function [107] for calculating the local curvature of the object using contact theories. The edge of the object could be detected by finding the zero crossing line from the shear strain distribution [141, 27].

As the tactile array data can be considered as an image, many researchers applied feature descriptors adapted from computer vision to the pressure distribution map obtained by tactile sensors in order to extract object features. The latter is then fed into classifiers, such as neural networks, kNN (K-Nearest Neighbor), and SVM (Support Vector Machine), for recognition of object local shape. Several studies applied image moments [21] to compute shape features [57, 30]. The Scale Invariant Feature Transform (SIFT) [111] is proved robust to the change of object pose. Therefore it can be used for object recognition regardless of object rotation and translation [139, 114]. Some other descriptors are also used in tactile sensing, such as regional descriptors by Khasnobish et al [89].

Besides vision descriptors, PCA-based features are also used for shape recognition. Principal Component Analysis (PCA) was applied to tactile readings, and the acquired principal components (PCs) are taken as features [108, 110].

Despite the wide use of feature extraction mentioned above, sometimes it is not clear what kinds of features are useful for object recognition. Therefore, machine learning attracts increasing attention in recent studies, which allows learning self-organized features for object identification instead of manually choosing task-specific features. [152, 142, 147].

### Global shape perception

With the measured local shape information of the object at different contact locations, the global shape can be reconstructed. In early research, the distribution contact point obtained at different locations of the object is widely

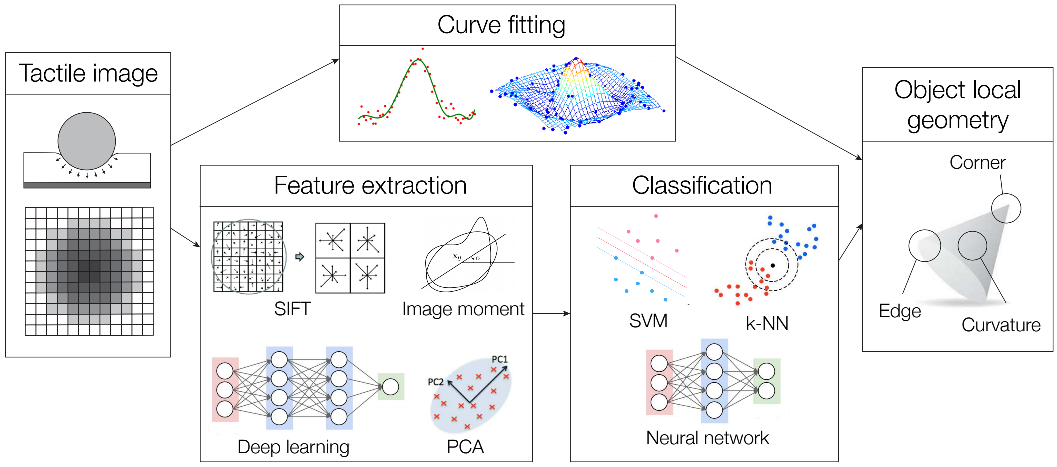


FIGURE 2.14: A summary of procedures for local shape perception

used by single point force sensors for reconstructing the global shape. The cloud of contact points can be fitted by geometric models to outline the contour of the object in the research of Casselli [20].

The Bag of feature (BoF) approach, which originates from the Bag of Word (BoW) for text classification, can be applied to the collection of tactile images. A vocabulary of object features learned from tactile observations of multiple objects is used to generate a histogram codebook. The global shape of an unknown object can be obtained by identifying from the codebook the distribution of features extracted from tactile images at different contact location [153]. A more recent approach associates tactile images with sensor locations for object global shape perception. The fusion of tactile and kinesthetic information is employed to classify object shape using machine learning methods [113].

However, as the global shape involves multiple local shapes at different locations, the robot should know where to get the local shape information in order to reconstruct the global shape efficiently. Tactile exploration is employed for such objective, which will be presented in detail in section 2.3.2.

### 2.2.3 Robotic perception of material properties

Tactile sensors can be used to perceive material properties, which is difficult for vision sensors. Among all the material properties, the texture, the stiffness, and the coefficient of friction of the object are the most crucial parameters for robotic use. The texture is important for object classification and recognition. The coefficient of friction of the object helps robots to avoid slippage during manipulation tasks. The stiffness is an important property widely used for tumor detection.

### Texture

Textures can be measured by sliding tactile sensors on the object surface and observing the vibrations and time serie signals [47, 194]. Classifiers such as k nearest neighbors (kNN), artificial neural network (ANNs), and support vector machine (SVMs), can then be trained to classify different textures [47, 198].

Besides, tactile sensors with a high spatial resolution (such as GelSight) are widely used for capturing tactile images containing microstructures of the objects. Figure 2.15 shows the examples of tactile images obtained by pressing the sensor against different clothing materials.

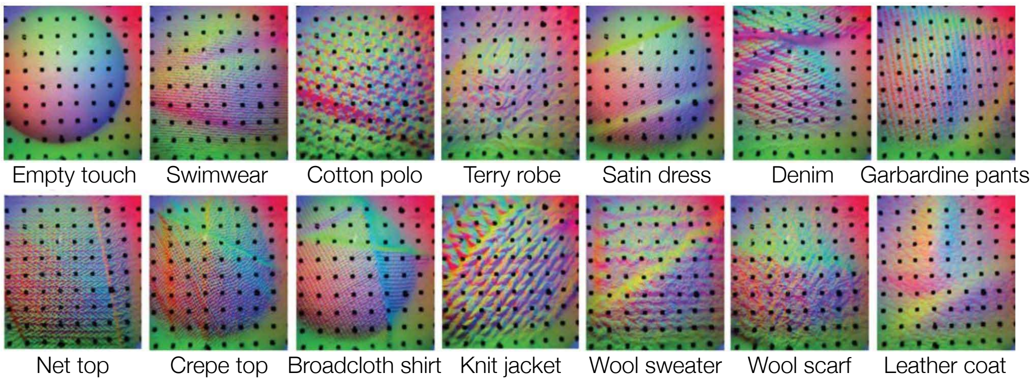


FIGURE 2.15: Tactile images of clothing texture captured with a Gelsight sensor [104]

Feature descriptors described in the previous section can be used on such tactile images for texture recognition. For example, the Local Binary Pattern (LBP) descriptor, which is locally invariant to rotation, is popular for texture recognition and classification in vision [140]. Li et al. employed this feature descriptor on the tactile images to extract textures of the surface in contact. The texture was then classified by comparing extracted features with the reference features using Hellinger distance metric [104].

In recent works, deep learning or Convolutional Neural Networks (CNNs) are also applied to tactile data to classify different textures. Yuan et al. trained a CNN for classifying clothing materials, which inputs the tactile images and outputs directly the clothing material properties [203].

### Coefficient of friction

The coefficient of friction is calculated by the ratio of normal and lateral force when two objects have relative motion. This parameter depends on the material of the object in contact. Measurements of the coefficient of friction can be achieved by calculating the ratio of normal and lateral force when sliding between two surfaces happens [62, 176].

However, the sliding is usually undesirable in manipulation and grasping tasks. As an alternative, a number of sensors have been proposed to measure the coefficient of friction when the sensor first contacts the object before sliding. In Maeno's work, the coefficient of friction is obtained without sliding by robot pressing into the object with a specified contact force and measuring the resulting displacement of a specific location under contact region [120]. Chen et al. reported an eight-leg tactile sensor on which legs were mounted with different angles with respect to the vertical. The coefficient of friction can be estimated by determining the number of legs that slip when the sensor is pressed against the object [24].

#### Stiffness

Stiffness is related to the material's elasticity and can be calculated by the ratio of force and deformation. It can be provided by pressing a sensor into the object with a specified speed and measuring the increment of contact force [206]. By using a BioTac sensor, the object stiffness can be estimated by investigating the ratio between force and indentation depth extracted from electrodes data [171]. In Drimus' work, by employing image moments of the tactile images as features, the k-NN classification method is used to classify objects into rigid and deformable [41]. A tactile sensing device is proposed with multiple indenting elements connected to springs with different spring constant. The stiffness of the surface in contact can be computed from the different indentation depth of each indenter [43]. In recent works, the hardness of objects can also be estimated by processing the tactile image sequences from a GelSight sensor [202, 205].

### 2.2.4 Robotic perception of interaction information

Robots equipped with tactile sensors can acquire information about the environment through interaction with its surroundings. The perception of interaction, including essentially force and slippage, is important for robots to plan stable and robust manipulation.

#### Contact forces

Perception of contact forces is essential in robotic interactions. All the robotic manipulation tasks involve the feedback and adjustment of forces. Some sensors only provide lateral or normal force, while others can measure 3d force vectors. Contact forces can be directly measured by single point tactile sensors that convert other forms of signals to forces [137, 151].

Although for tactile sensors with arrays of sensing elements, the contact pressure on each taxel can be estimated using simple calibration methods [70], it is still necessary to calculate the resultant contact force. Some research model the local pressure measured by each tactile sensing element as a linear function, and sum up local pressures to estimate the contact force [171]. However, as the soft elastomer of the sensor is nonlinear material, machine learning algorithms are widely used to learn the nonlinear relation [189, 201, 170]. Besides machine learning, other methods are also applied for mapping the local pressure or deformation array to resultant contact force. For example, finite-element methods have been used to model the nonlinear functions and estimate the force distribution using a Gelslim sensor [115]. Another research computes the contact force and torque from the deformation distribution of the sensor using the Helmholtz-Hodge Decomposition (HHD) algorithm [208].

**Slippage**

During the manipulation tasks, slippage should be avoided for ensuring a stable grasp. Therefore, the capability of slippage perception is particularly important for tactile sensors to correct grip force.

The slippage includes gross slip (when all parts of the contact interface slide against each other) and incipient slip (when part of the contact interface slides while other parts remain stuck). The gross slip detection is mostly based on sharp changes in signals due to the stick-to-slip transition [25]. Moreover, the micro-vibrations of the sensor induced by slippage is also widely used for gross slip detection [45, 170]. The sudden displacements of the markers in the slip direction can also be considered as the appearance of gross slip. This method is often used by camera-based tactile sensors embedded with markers of which the displacement can be captured by the camera. [73].

However, during the robotic manipulation, the gross slip should usually be avoided to prevent the object from dropping. Therefore, a large number of research proposed methods for detecting the incipient slip. Maeno et al. showed that the incipient slip always occurs near the edge of the contact area. The lateral strain distribution of the soft medium indicates the stick-slip pattern at the contact surface and can serve for incipient slip detection [119]. Therefore, the perception of incipient slippage is mostly done by soft tactile sensors with multiple distributed sensing elements.

For example, Canepa et al. designed a tactile sensor constructed by eight pairs of piezoelectric transducers embedded inside a silicone rubber. One transducer in each pair is sensitive to normal stress and the other to shear stress. Normal and shear stresses components inside the sensor are used to train a neural network to output the degree of incipient slip [19].

Watanabe and Obinata proposed a camera-based tactile sensor made of transparent elastomer painted with a grid of dots. The incipient slip can be perceived when the lateral displacement of the dots on the outer side of the contact region happens [187].

Yuan et al. have also proposed a method to measure the incipient slip using a Gelsight sensor. Markers are printed onto the surface of the soft sensor. When an object is pressed against the sensor, the entropy of the displacement field of the elastomer calculated by marker tracking indicates the degree of incipient slip [204].

In conclusion, tactile sensing capability is crucial for robotic perceptions of object properties and interaction information. Tactile sensors could be used in various applications such as slip detection, object classification, and material recognition. With the development of computer vision and deep learning, tactile sensor with high spatial resolution becomes a trend because many vision-based processing methods could be directly applied to tactile images to extract object features. However, despite the advantages of high-resolution tactile sensors, few commercial solutions exist for now. How to efficiently use the tactile data for an accurate and robust perception of the object properties and interaction information; how to map the distributed tactile data to 3d space; how to combine tactile data and kinaesthetic information; how to integrate tactile perception to other sensing modalities, still remain open issues in tactile perception.

## 2.3 Action: active interaction with objects

For most robotic applications, robots need to execute sequences of actions to carry out complex tasks, such as exploring, grasping, and manipulating. Industrial robots are able to act fast and reliably even without a tactile sensor because movements are predetermined and programmed in advance. Without knowledge of the object, accurate and automatic action is impossible. The perception of interaction information and object properties allows the robot to perform manipulations automatically on more general objects with unknown properties. However, while tactile sensors provide a rich perception capability, how to integrate tactile information into robotic control and develop robust action strategies for different tasks is still the main challenge for today's robots. According to different tasks, the required robotic actions variate. The most common actions include exploration, grasping, and manipulation.

### 2.3.1 Human hand action

Hands movements allow humans to perform an enormous range of actions, among which, object exploration is one of the most essential actions that are usually performed by hands. Humans can perceive object properties through active contact and movement of hand and fingers relative to objects, which was called exploratory procedures. This exploratory procedure involves both static and dynamic contact between hand and object. The thermal sensing is associated with static contact, for which there is no essential moment of fingers. Dynamic contact includes normal motion and tangential motion of the finger relative to the object surface. The normal motion induces pressure onto the finger. The finger skin deformation indicates the local shape of the objects. Pressure on the finger combined with the normal indentation gives cues of the object compliance. Lateral motion between finger and object surface allows the perception of textures and roughness. Contour following can also be performed by continuously moving the finger tangentially to the surface of the object, which is essential for perceiving the global shape of the object. Figure 2.16 illustrate the most investigated EPs for object perception [91]. (EPs) [94].

Besides exploration, grasping and manipulation are also essential actions of human hands. Human is able to adapt the grip force and holding gestures to grasp different objects without dropping them. The adjustment of grip force even begins from the first contact with the object [74].

While grasping is about holding the object steadily in hand, manipulation refers to the change of the object pose and rotation while keeping the contact. It can be classified as prehensile manipulation and non-prehensile manipulation, as shown in figure 2.17. The prehensile manipulation requires at least two contact points on the object to stably keep the object in hand, while the non-prehensile manipulation can be performed with only one finger. A manipulation task consists of a series of finger actions, especially for manipulations with within-hand motions. Actions to choose for a manipulation task depend on object properties such as shape, weight, and texture.

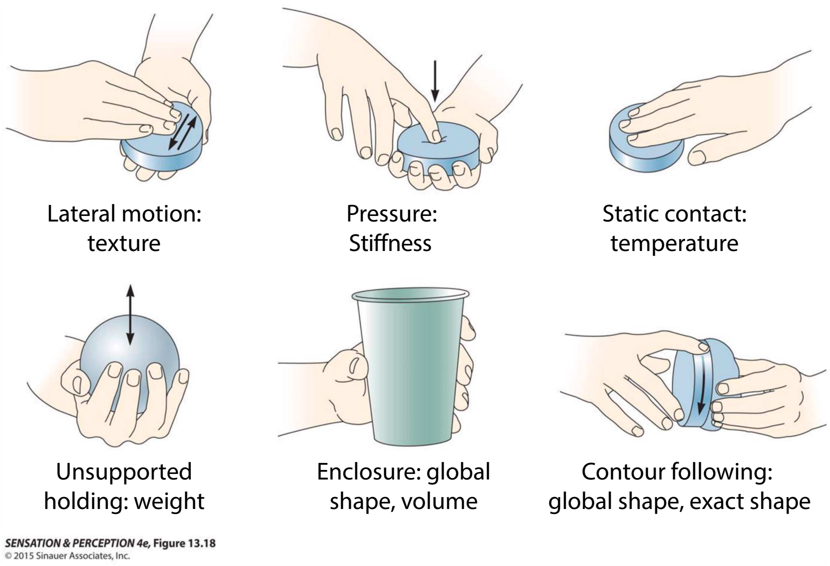


FIGURE 2.16: Exploratory procedures for active tactile perceptions of different object properties [94]

This requirement on object properties reveals the importance of humans' tactile sensing and perceiving ability. Besides, the task-related factors such as required movement pattern and manipulation performance demands also influence the choice of hand actions [90].

### 2.3.2 Robotic exploration

Tactile exploration is an effective way to extract properties of unknown objects such as material properties and object shapes as mentioned in the previous section.

During the exploration tasks, it is important to select optimal exploratory movements, which enable the robot to gain the most information. In the study of Xu et al. [195], objects with different textures, compliance, and temperature were explored and identified. The exploratory movements are intelligently selected using a process called Bayesian exploration developed in the previous work of Fishel et al. [47]. With this exploration strategy, exploratory movements that provide the most distinction between likely candidates of objects are automatically selected.

Another essential application of tactile exploration involves tactile servoing control, which computes robotic actions to maintain the desired contact pattern. Zhang et al. presented for the first time the tactile servo, which uses tactile sensing in the feedback control of robot contact tasks [207]. Using tactile jacobian and inverse sensor model, the proposed tactile servoing controller transforms the change from the tactile feature to a robotic task related

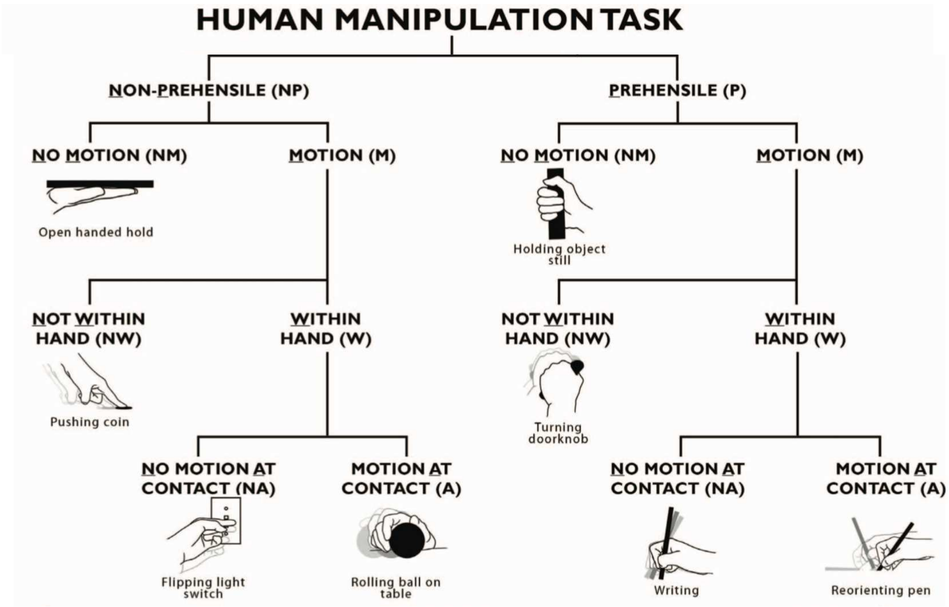


FIGURE 2.17: Human manipulation taxonomy proposed by Bullock et al. [15]

to the movement of the robot's end-effector. In the work of Li et al., a control framework is introduced to perform tactile servoing tasks [104]. The robot was able to follow the unknown shape of a cable by maintaining contact location, orientation, and force. Later, Lepora et al presented an algorithm that TacTip sensor to perform contour following [99]. With rotation, radial, and tangential movement of the sensor, their tactile servoing control maintains the same orientation and displacement relative to the edge perceived by the tactile sensor. The movement of the sensor was decided using evidence accumulation methods which is detailed in their previous work [98].

### 2.3.3 Robotic grasping

Grasping is one of the most basic and essential actions in robotic applications. In order to ensure a stable grasp, tactile feedback can be used to control the contact force and the contact location.

#### Grasp with slippage detection

Slip detection is a popular approach to control the grasp. Robots just need to increase the grip force when slippage is detected for ensuring a robust grasp. This strategy is widely used via different tactile modalities, such as vibrations, relative movement of markers, signal peaks of force, which indicate the appearance of total or partial slippage. McInroe et al. developed a pneumatic camera-based tactile sensor. When the shear deflection of the markers is detected, the pressure within the sensor is increased to regrasp the object and prevent slippage [122]. The grasp control with FingerVision sensor mounted on a two-finger gripper was presented by Yamagauchi et al. [197]. The sensor could detect slippage by measuring the object movement captured by the camera of the sensor. Using slip detection, the gripper was able to hold deformable and fragile objects such as tomatoes, raw eggs, and cupcakes without slippage or damage on objects.

### Grasp with estimation of coefficient of friction

The grasp control can also be achieved by estimating the coefficient of friction between the sensor and the object. The common procedure is shown in figure 2.18a.

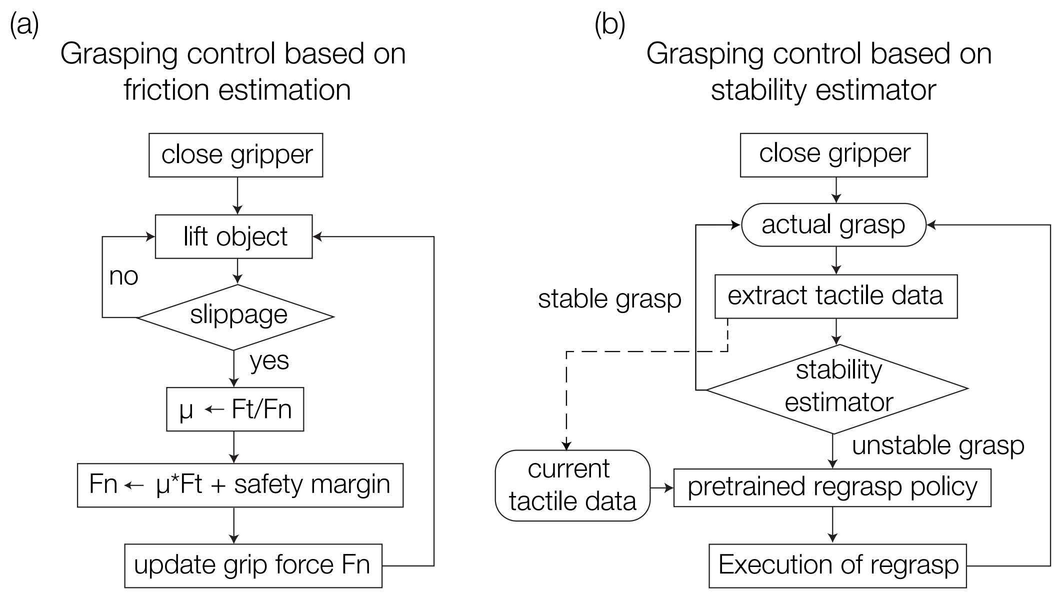


FIGURE 2.18: Basic algorithms for grasping control using friction estimation (adapted from [170]) and stability estimator (adapted from [35]).

Su et al. used a BioTac sensor to estimate contact forces, as well as detect and classify slip events [170]. The coefficient of friction was first set to an initial value and then updated by the ratio of shear to normal force measured by the BioTac sensor if slippage happens. This newly estimated coefficient of friction is then used for calculating the required grip force in order to lift objects of various weights and texture with minimal forces. Later, a grasping strategy employing the coefficient of friction estimation was studied in [81]. A three-finger robotic hand attached with OptoForce sensors was used to grasp objects with changed weight. During the increase of the object weight, the coefficient of friction was estimated as soon as the slip was detected. Then the coefficient of friction was used for regulating grip force. In order to avoid crushing the deformable heavy object, the grip force cannot exceed the limit. Thus, if the mass of the object continuously increases, the gripper will start rotating the object for compensating the weight. This strategy allows the gripper to prevent slippage with minimal grip force while grasping deformable heavy objects with dynamic centers of mass, such as containers with liquids.

#### Grasp with stability estimator

Constructing a grasp stability estimator from tactile reading is also a popular approach in grasp control, as shown in figure 2.18b.

In the work of Dang and Allen, in order to grasp objects with an uncertain pose, a control algorithm was developed using a BarrettHand. An SVM classifier was trained to estimate the stability of the grasp. By inputting the grasp features extracted from tactile data captured by the sensor, the classifier outputs whether the grasp is stable or unstable. If the grasp is unstable, a tactile experience database which consists of predefined stable grasps and their corresponding tactile contacts was used to adjust the gripper. The adjustment was performed by querying the database for stable grasps with tactile contacts similar to those of the current grasp using k-nearest neighbor algorithms [35]. Recently, with tactile data obtained from OptoForce sensor mounted on a three-finger robotic hand, Murali et al. developed a re-grasping policy that plans new grasp gestures based on the previous one. A grasping stability estimator was trained by deep learning to estimate the state of the grasp. Then the robot re-grasp the object if the grasp is unstable because of the wrong grasp position and the object slippage [127]. Calandra et al. used a two-finger gripper embedded with GelSight sensor to control the grasp. A convolutional neural network was constructed as a grasp stability estimator that predicts the success probability of the grasp. The input of the estimator is multi-modal which includes the tactile image obtained by the GelSight sensor, the RGB image obtained by an external camera, as well as the candidate re-grasping action. Once the estimator is built, the most promising re-grasp action which maximizes the success probability of grasp was then selected from randomly sampled potential actions using the Markov decision process [18]. Moreover, a re-grasping strategy was explored by Hogan et al. using the GelSlim sensor. They simulate the new tactile image that would be obtained from the regrasp motion by performing rigid-body transformations of the given tactile measurements of the initial grasp. A trained grasp-stability estimator evaluates the possible motion of the robotic gripper and chooses the one with the best stability score [59].

### 2.3.4 Robotic manipulation

Robotic manipulation tasks refer to the handling and state change of the object using a robotic hand. It includes not only in-hand manipulations, but also non-comprehensile manipulations.

#### In hand manipulation

Different from grasping tasks that only require firmly keeping the object in hand, for in-hand manipulation, the grippers or multi-fingered robotic hands should be able to preserve the grip and relocate the object at the same time. In such tasks, system models are usually used, which describe the finger-object contact as well as the mechanics of fingers and objects, for designing the control algorithm. The early literature assumes perfect knowledge of grasp properties, including the object center of mass and the contact friction. For example, Cole et al. studied the kinematics of two surfaces with arbitrary shape rolling on each other. The control of two planer multi-fingered hand manipulating an object was simulated by applying the kinematic model to the finger-object dynamic system [28]. However, the object properties are usually unknown without measurements when performing real manipulation tasks. The tactile perception of the object and the contact force could help to compute the appropriate action.

Li et al. proposed a control algorithm to search the local optimal contact points for grasping by exploring the surface of the object during the in-hand manipulation [103]. Using tactile feedback of contact location and force, the multi-fingered robotic hand is able to stably rotate a sphere by sliding one fingertip over the surface of the sphere to search the next optimal grasp location, while the other fingers are holding and slightly rotating the object. As tactile feedback is available in their simulation, a very simple model with only a few assumptions is sufficient for designing the controller. Shaw-Cortez et al. proposed a controller for manipulating unknown objects with the implementation of tactile force sensors in robotic hands. They proved that by integrating the tactile feedback into the control loop, the robotic hand was able to guarantee that the object does not slip within grasp during manipulations [162].

Lambeta et al. also introduced the DIGIT sensors mounted on Allegro multi-finger hand. A deep neural network model-based controller was trained allowing the in-hand manipulation of a glass marble with the robotic fingers [93].

The manipulation algorithms mentioned above involve a fully actuated system, where the number of degree of freedom (DoF) is equal to the number of actuators. However, in robotic hand manipulation, underactuated hands, where the number of DoF is larger than the number of actuators, are commonly used, as it can perform grasp and manipulation tasks with a small number of actuators and control inputs. Additionally, with the compliance and under-constrained mechanisms, such a system adapts better to the object pose uncertainties. In the work of Van Hoof et al., an underactuated robotic hand was used to perform in-hand rolling tasks. They employed deep learning to learn generalized policies for a rolling primitive based on Markov Decision Process. The robotic fingers were equipped with tactile sensors to provide tactile feedback in their control policy [179]. Moreover, a method using biomimetic active touch is reported by Ward-Cherrier et al. [184]. A 3d printed gripper is presented able to perform in hand cylinder reorientation while maintaining a stable grasp. Tactile feedback allows the control of the manipulation trajectory of the gripper using Bayesian active perception algorithms [97]. Instead of rotating the in-hand object only by finger motion, Lu et al. developed a soft gripper composed of 2 pressurized air cavities on each finger. The deformation of the cavities caused by pressure change allows the gripper to perform in hand rotations. The cavities act as soft tactile sensors for the measurement of contact pressure in order to provide control of grasping position [112].

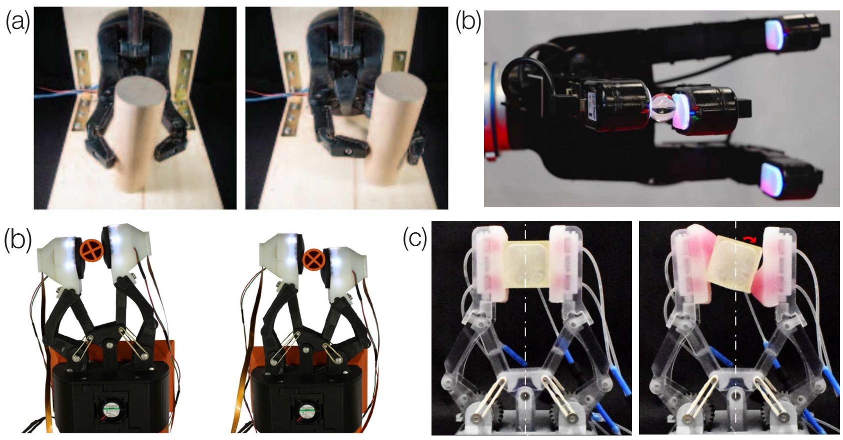


FIGURE 2.19: In hand manipulations using tactile sensing presented in (a) [179], (b) [93], (c) [184] and (d) [112]

### Non prehensile manipulation

Non-prehensile manipulations refer to interactions with objects without grasping, such as pushing, hooking, squeezing, and rolling. Different tactile information can be implemented in different non-prehensile manipulation.

In the work of Sutanto et al., tactile information was implemented to the control loop for a door opening task. The tactile feedback can help ensuing an accurate alignment between robotic fingers and the door handle [143]. Meier et al. proposed a method to use the slip detection capability of the tactile sensor for pushing tasks. The sensor was pressed onto the object's top surface and moved laterally to push the object. A convolutional neural network was employed to classify whether the object is sliding with the sensor or slipping from the sensor [123]. Recently, by decomposing complex manipulation plans into sequences of manipulation primitives with simple mechanics and efficient planners, Hogan et al. achieved various manipulation tasks using two robotic hands equipped with tactile sensors. The tactile information was used for object state estimation and contact state estimation in a close-loop controller to enforce the desired contact state and change the planned trajectory of the object in response to perturbations [58]. Another non-prehensile robotic controller was presented by Tian et al. for performing rolling tasks. They proposed a framework for learning to perform tactile servoing from raw tactile images. A predictive model was learned using the deep neural network to predict different action sequences with tactile observation as inputs to roll the objects on the table [174].

In conclusion, it is important for robots to know how to perform an appropriate action regarding different tasks. For doing this, the use of tactile sensors is beneficial as it can give feedback to robotic motion controllers about the contact location, object properties, and information of the interaction (e.g. direction and magnitude of the pressure, friction, and slippage). Nowadays, most of the off-the-shelf robots only use single-point force sensors or vision to guide the robotic motion. However, with the development of deep learning, the implementation of tactile arrays in robotic control loops for dexterous robotic actions seems to meet a bright future.

## 2.4 Conclusion

This chapter reviews the state-of-the-art from tactile sensing to robotic actions. Figure 2.1 illustrates the four most essential steps towards dexterous robotic manipulation. The first step is to sense the contact. Different types of tactile sensors and tactile sensing technologies were presented. With the tactile sensor converting contact signals to other forms of processable signals, the tactile perception could be achieved. Various processing methods can be adapted for extracting different interaction information (e.g. force, slippage) and object properties (e.g. shape, texture, friction). By integrating the knowledge of the interactions and object properties perceived by tactile sensors into the control loop, the robot is able to perform suitable actions on objects, including exploration, grasping, and manipulations. The robotic actions involve contact between the robotic hand and the object, which is detected and measured by tactile sensors. In this whole procedure from sensing to actions, tactile sensors play an indispensable role, which bridges the gap between the physical contact and the robotic perception of the external world. Tactile sensing provides robots a much complete knowledge of the object during interaction and seems to be a promising key towards dexterous robotic manipulations.

# Chapter 3

# Tactile sensing via color mixing

## Contents



Adapted from: Lin, Xi, and Michaël Wiertlewski. "Sensing the frictional state of a robotic skin via subtractive color mixing." IEEE Robotics and Automation Letters 4.3 (2019): 2386-2392.

## Preface to Chapter 3

To address the issue of low spatial resolution and lack of 3d measurements of many tactile sensors, this chapter introduces the design, manufacturing, and working principle of a new camera-based tactile sensor, which uses subtractive color mixing principle and marker tracking to compute both normal and lateral displacement field. With 100 overlaid markers that changes color under external load, the sensor is able to recover its 3d deformation map from 2d images. Experiments were carried out to calibrate the sensor and validate the sensing methods. Simulations show sensor robustness to pixel density and lighting condition. The same sensing principle is used in the following chapters of this thesis to measure the 3d deformation map of the sensor, estimate the curvature, and estimate the frictional property of of the object.

## Abstract

The perception of surface properties such as shape and adherence is crucial to ensure that the hand-held object is stable. Without touch, precise manipulation becomes difficult. Some robotic tactile sensors use cameras that observe the elastic deformation of a membrane to detect edges or slippage of the contact. Information about the contact state drive innovative control strategies. However, most previous methods on these lines do not include quantitative means of measuring the 3-dimensional deformation of the skin or suffer from a lack of spatial resolution. Here we present a tactile sensor based on a subtractive color mixing process designed to track the 3-dimensional displacement of an array of markers, using the information delivered by the color channel of off-the-shelf cameras. The distributed shear and normal deformation can be assessed from the spectrum of the light reflected and refracted by an array of diffusive and transmissive markers placed on two superimposed layers. The markers show various blends of colors, depending on the displacement at the surface. The color pattern of each marker can be tracked with little computation and remains robust external lighting. The ability to sense the 3-dimensional deformation field can improve robotics perception of frictional properties which have applications in the fields of robotic control and human-robot interactions.

## 3.1 Introduction

For both robots and humans, tactile perception is essential to be able to learn and perform appropriate hand gestures for grasping and manipulating objects [129]. In particular, humans' tactile perception of the state of contact between a finger and an object generates information on which the stability of the grasp depends [75]. The object might have to be moved reliably from one place to another without inducing any perception of relative motion with respect to the fingers. In other scenarios, the opposite problem might arise when the object has to be slid to a certain part of the hand in order to be properly lifted. These chains of events involve fine and dexterious control of the frictional contact between the object and the skin. In humans, the state of friction is thought to be assessed not by directly determining the normal and tangential components of the force, but rather depending on which part of the fingertip is stuck to the object and which part is starting to slide [3, 38]. The contribution of tactile sensing to grasping and manipulation has been well recognized [34]. Artificial skin based on piezo-resistive [169], piezoelectric [61], electrostatic [190], optical [82] and even ultrasonic transducers [165] have been previously tested. These tactile sensors convert the localized deformation of the surface into a signal that is stored and interpreted by a computer. These sensors can collect information that is not accessible visually, not only because the contact is often hidden from view, but mostly because the information about the contact, such as the adherence of the surface or the compliance of the material, requires mechanical interactions to be revealed.

Many of the latest methods designed for this purpose focus on measuring the pressure field applied normal to the surface, which suffices to recognize objects [195]. It has been established, however, that the lateral traction produced by friction is essential to controlling robotic grippers [119, 56]. Sensors with large number of sensing elements also requires a cumbersome set of electrical interconnections and conditioning electronics.

Some sensors use a camera to transduce the deformation of an elastic body or membrane [46, 186, 148, 79]. The usual procedure starts by locating the center of black or white markers. The lateral motion of each marker can be easily determined with computer-vision algorithms and the distributed measurements are sufficiently rich to recognize the nature and orientation of an object. However, these methods do not directly provide the normal and lateral pressure field at the interface. In particular, the local friction coefficient, expressed by the ratio between the lateral shear stress and the normal stress cannot be directly observed although this parameter is essential for characterizing the adherence of an object and its stability in the hand.

To address these challenges, we developed the camera-based sensor, shown in Fig. 3.1a and b, which not only tracks the lateral motion of an array of markers but also resolves the motion normal to the surface. The sensor recruits a double array of overlapping semi-transparent colored markers. The deformation of the markers, which are attached to the interaction surface, affects their shape and their color content, which makes it possible to reconstruct of the 3-dimensional deformation field at the interface.

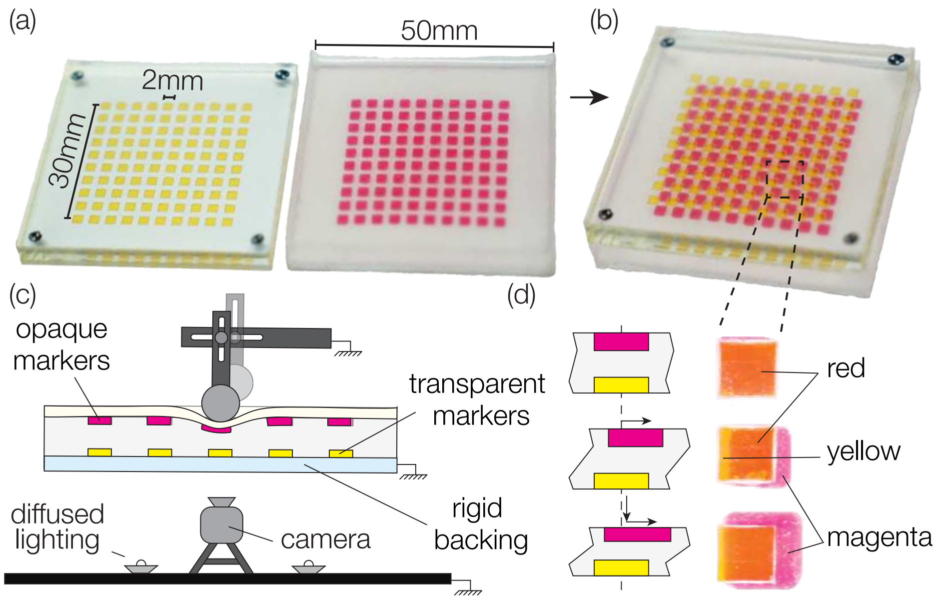


FIGURE 3.1: (a) Exploded view of the tactile sensor based color mixing. Yellow markers are rigid and magenta markers are deformable. (b) View of the sensor assembly. (c) Diagrams illustrating the deformation of each layer under an inclined external force. (d) Compressive and shear deformations can readily be determined from the color pattern.

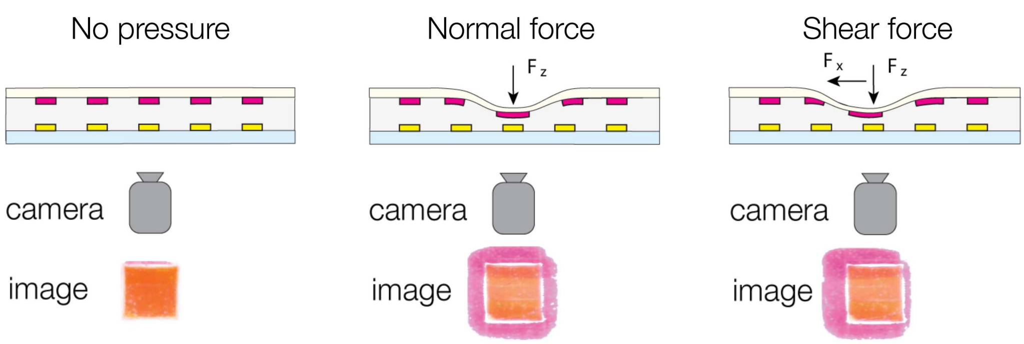


FIGURE 3.2: Illustration of the sensor without pressure, normal force and shear force captured by the camera, and the real image of the pressed marker captured by the camera.

## 3.2 Background on camera-based robotic fingertip

Since cameras are ubiquitous and provide a fast, reliable way of transferring real-time data to a controller, many artificial fingertips have included an off-the-shelf optical sensor, thus reducing the need for the custom-made electronics required in piezoresistive and capacitive sensor arrays.

Artificial fingertips are often made by including in a soft hemispheric membrane markers that can easily be tracked using state-of-the-art image segmentation methods. Once the membrane's elasticity and shape have been determined, the stress at the surface can be calculated by performing least-squares regressions [46]. Markers can be mounted on pillars to amplify the rotation of the membrane and improve the sensitivity of these sensors to edges [26, 186].

In these devices, the sensor encodes a 2-dimensional displacement field in which the local traction and the indentation are combined.

The GelForce sensor includes two layers of spherical markers of different colors to determine the full 3-dimensional stress field. Any stresses imposed on the surface will induce deformations of the solid, the intensity of which depends inversely on the depth of the markers. By performing a linear interpolation, it is possible to determine the lateral and normal stresses from the displacement of markers located at different depth [85]. The efficiency of this method has been established with an artificial finger equipped with a 5x5 grid [148]. However, as these markers are opaque, only a few markers can be seen at the same time, which reduces the spatial resolution of the system. In another interesting approach is based on the apparent sharpness of the marker when it moves out of focus [53].

The Gelsight sensor provides a picture of the deformation field using photogrammetric methods [79]. This sensor is composed of a thin layer of silver flakes, which diffuse light in all directions. The relief of an object that is touched can be reconstructed using three separate illumination sources and a Lambertian reflectance model. This setup gives the shape of the object with an unmatched level of precision, and hence the relative position of a tactile feature [105]. However, since the motion of artificial skin particles is not tracked, the stress field at the interface cannot be easily determined. The authors solved this problem by adding a layer of dots giving information about slippages [204].

Our own method focuses on uniformly sampling the deformation field at the surface of an elastic body. With this marker-based method, the shear deformation is determined via the centroid tracking of each, and the normal deformation, via the blend of colors between two layers of markers acting as a band-limited optical filter.

## 3.3 Sensor principle and manufacturing

### 3.3.1 Design rationale

Inspired from tactile sensing capability human fingertip, some basic design criteria can be formulated for tactile sensing in a general robotic system in order to ensure that the sensor collects meaningful information [34].

– *High spatial resolution*: Without any relative motion, surface defects as small as 1mm in a ≈10mm-diameter contact area can be detected by human touch alone [188]. Therefore the tactile sensor is expected to able to detect surface undulations which are at least 10 times smaller than the contact area. As the spatial resolution of human fingertip is as high as 1mm, the tactile sensors is suggested to have similar spatial resolution of 1-2mm in order to detect fine distribution of stress and deformation field.

– *Force sensitivity and dynamic range*: In robotics, the sensitivity and dynamic range are highly application dependent. However, in order to adapt various exploration and manipulation tasks, a high sensitivity and dynamic range is desired in tactile sensors [37].

– *3d force and deformation measurement*: Friction plays a crucial role in the stability of our grasp [11] and in the perception of materials [191]. In order to determine the friction and slippage, both not only normal but also shear components of the deformation field have to be determined by the tactile sensor.

– *Soft sensing skin*: The robotic tactile sensors are better to be soft in order to protect the sensor from damages and ensure safe human-robot interaction. The elasticity of the medium diffuses the stress throughout the solid so the deeper the markers are located, the more individual motion are smoothed out. To avoid this, the markers should be located close to the surface of the sensor [163].

– *Fast response and low hysteresis*: The robotic tactile sensors should be fast and respond quickly without visible hysteresis. This is particularly important, if the feedback from tactile sensor is involved in the robotic control loop.

– *Multi-functionality*: The tactile sensor with ability to measure more than one contact parameter is desired. According to the research of Okamura et al [133]. following modalities of an external mechanical stimulus are important for robotic manipulation tasks: contact detection, pressure distribution and slip detection. Robotic exploration tasks can be supported by following tactile information: object shape, object softness and surface roughness.

However, one of the consequences of having a large number of markers to improve sensor spatial resolution is that each individual marker occupies only a few pixels and changes of size and location are hardy perceivable. Our approach overcomes this issue by making use of the color channel available is off-the-shelf cameras. Instead of finding the normal motion from the change in size of a pixellated monochromatic blob, our sensor encodes the normal motion reliably via a change of color, even when only a handful of pixels are used.

### 3.3.2 Color mixing from partial occlusion

The new sensor is constructed around a soft transparent silicone body in which two separate layers of colored markers are embedded. Markers closer to the surface of the skin are soft and reflect magenta light (that has a spectrum containing both blue and red wavelengths). In the implementation shown in Fig.3.1a, the setup is comprised of one hundred 2mm-wide markers placed 1mm apart. The second layer of markers overlying the magenta marker array and consists of a material that is transparent to light with a wavelength greater than 500 nm. The high-passfilter gave these markers a yellow appearance to the naked eye and to camera sensors. When pressure is applied to the surface of the sensor, the magenta markers are brought closer to the yellow filter, see Fig.3.1c. Shear forces will shift the center of each marker relative to each another. The combination of stretch, compression, and a lateral shift creates a colored pattern, which specifies the direction and the magnitude of the displacement vector of the surface above the markers Fig.3.1d.

Fig. 3.3a and b are typical views of the two layers, showing the three colors magenta (which is white without any green), yellow (which is white without any blue) and red (which is white any green or blue). Marker arrays are flooded with diffuse white light, which can be either diffused by the magenta markers or the white layer and possibly filtered by the yellow markers on its

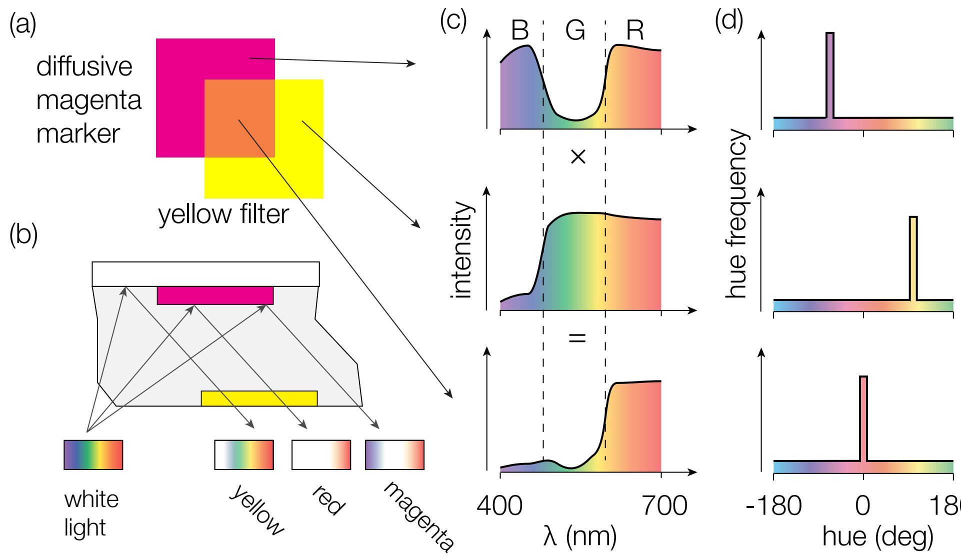


FIGURE 3.3: (a) Diagram of the image of the marker observed by the camera (b) The white light is scattered by either the background or the magenta marker. Some of the scattered light crosses through the yellow filter, which further filters the color spectrum (c) Color spectra of the light after the reflection by the magenta markers, of the light after being transmitted trough the yellow markers, and of the light which is both scattered by the magenta markers and filtered by the transparent yellow filter. (d) Corresponding histograms of the hue channel in the HSV colorspace.

way back to the camera. All four combinations of the color spectrum shown in Fig. 3.3b can be seen in the resulting image.

Physically, shifting from white to red occurs when the magenta markers reflect only the red and the blue parts of the spectrum and the blue is filtered out by the yellow layer, as described in Fig. 3.3c.

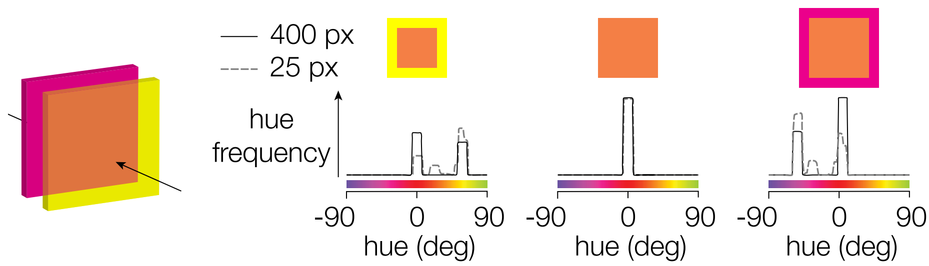


FIGURE 3.4: Effect of the change in the size of the magenta markers on the histogram of the hue channel. The histogram is only slightly affected by the number of pixels in the image.

Humans and cameras alike detect only three bands in the optical spectrum, in the blue (≈450nm), green (≈580nm) and red (≈690nm) ranges. Images detected in the Red-Green-Blue color space can be converted into Hue-Saturation-Value (HSV) color space, where the value and the saturation depend only on the illumination of the markers and the hue channel contains the color information. An example of the hue intensity of typical light rays is presented in Fig. 3.3d. The hue channel is presented in the form of a color, where the colors are shown at an angle with respect to an arbitrary origin, set at red. In the HSV color space, the center of mass of the histogram of the hue channel depends on the normal displacement of the soft marker with respect to the transparent marker, see Fig 3.4. Since changes in the hue of the image involve a large number of pixels carrying 24 bits of information (versus 1 bit in the case of segmented black and white images), these fluctations will be theoretically more visible in the case of small displacements than the apparent change in the marker size, which translates into greater sensitivity to the motion normal to the surface.

### 3.3.3 The opto-mechanical model

This section describes models for the optical and mechanical components of the complete sensor.

**Effects of the focal length on the resolution** The reliability of the measurements depends on the camera and lens used to detect the markers. A longer telephoto lens will reduce the apparent changes in the marker size, and a simple model shows that the shorter the focal length, the more pronounced the motion of the moving marker will be.

The model illustrated in the Fig 3.5a is based on the well-known pinhole camera model, in which light rays reflected by objects and reaching the image plane cross a point located one focal length from the image sensor.

The problem is constrained by the fact that $n$ markers have to fit into the field of view $\theta_t$ as shown in Fig 3.5. Each of the markers therefore has to cover a fraction of the field of view, $L_0/(d+t) = \tan(\theta_t/n)$. The pinhole model states that the angular size of the markers is the same on both sides of the focal point, $\tan(\theta_t/n) = l_0/f$. With these constraints in mind, maximizing the sensitivity of the sensor in the normal direction amounts to maximizing the relative changes in the apparent size $(l-l_0)/l_0$ with a given normal

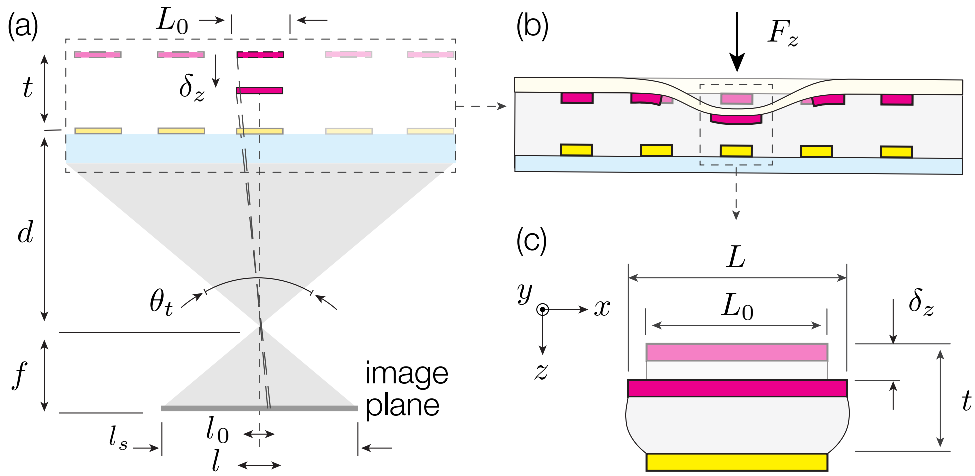


FIGURE 3.5: (a) The pinhole camera model explaining how sensor motion is correlated to changes in apparent size. (b) The large Poisson coefficient of soft material results in significant stretching of the soft marker, which increases the signal to noise ratio. (c) The optimum thickness maximizing the apparent change in the case of a given external force is presented here, depending on the camera's angle of view.

displacement of the marker $\delta_z$. Let us take Thales' intercept theorem:

$$\frac{l}{f} = \frac{L}{d + t - \delta_z} \tag{3.1}$$

$$\frac{l_0}{f} = \frac{L_0}{d + t} \tag{3.2}$$

Combining these equations leads to the relative change:

$$\frac{l - l_0}{l_0} = \left(1 - \frac{\delta_z}{d + t}\right)^{-1} - 1 = \frac{\delta_z}{d + t} + O\left(\delta_z^2\right) \tag{3.3}$$

The result of this equation is shown in Fig 3.6a. The smaller the distance to the object is, the more noticeable the changes will be. In addition, a camera with a short focal length is beneficial for creating a compact tactile sensor. Smaller focal length optics are therefore preferred.

**Mechanics and optimal thickness between layers** The top layer of the assembly is soft and the magenta markers can be stretched elastically. Stretching increases the actual size of the marker and therefore further enhances the sensitivity, see Fig 3.5b.

A simple model for the deformation of the marker can be drawn up, taking only the elasticity of the material sandwiched between the two layers. In this simplified model, which is presented in Fig. 3.5c, the behavior of the

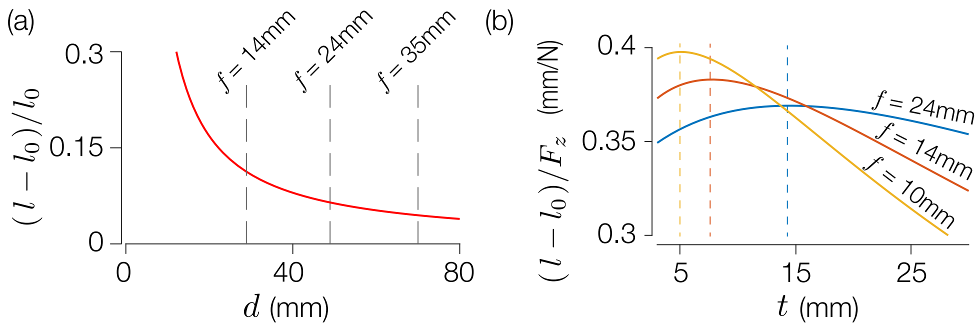


FIGURE 3.6: (a) The soft magenta layer is pushed down towards the yellow filter. (b) The model predicts that a wide angle lens will give greater magnification at a given normal displacement of the marker.

material boils down to a compression ratio that can be described by the material's Young's modulus $E$, the thickness $t$ and the marker size $L$, as well as a lateral extension corresponding to the Poisson's ratio $\nu$. The compressive elasticity of the material just below the marker can be obtained by deriving Hooke's and Poisson's laws:

$$\delta_z = \frac{F_z}{EL_0^2} t \tag{3.4}$$

$$L = L_0 \left(1 + \nu \frac{\delta_z}{t}\right) \tag{3.5}$$

We can see that a thicker sensor gives greater marker mobility at a given external force, at the expense of a smaller change in the apparent area. A thickness that maximized the compliance while keeping a large stretch was obtained by combining equations 3.1, 3.2, 3.4 and 3.5. Assuming that we have a Young's modulus of $E = 0.4$ MPa, Poisson's ration $\nu = 0.5$ and a marker size of $L_0 = 2$ mm projecting an image onto a $l_s = 35$ mm sensor, the results obtained with three different lenses are presented in figure 3.6b. The model argues in favor of a soft material with a low Young's modulus, which could be thin and deformable.

### 3.3.4 Robustness to pixel density and lighting conditions

One of the main advantages of using color channels is that the marker configuration can be resolved using just a few pixels. A simulation was run to verify the robustness of the method when only a few pixels were used. A single marker was first drawn using a vector graphics editor (Illustrator, Adobe, San Jose, CA, USA) to depict an opaque magenta marker underlying a yellow marker with an opacity of 50%. The size of the magenta marker was changed to provide a range of artificial normal displacements. Images were rasterized in a 512x512 image and a pyramid gaussian process was used to create smaller versions, with the goal to emulate the effect of having smaller markers. Once the small version was created, an anti-aliasing filter that leverages a Gaussian filter with standard deviation set to 1/8th of the size of the image was added to remove artifacts.

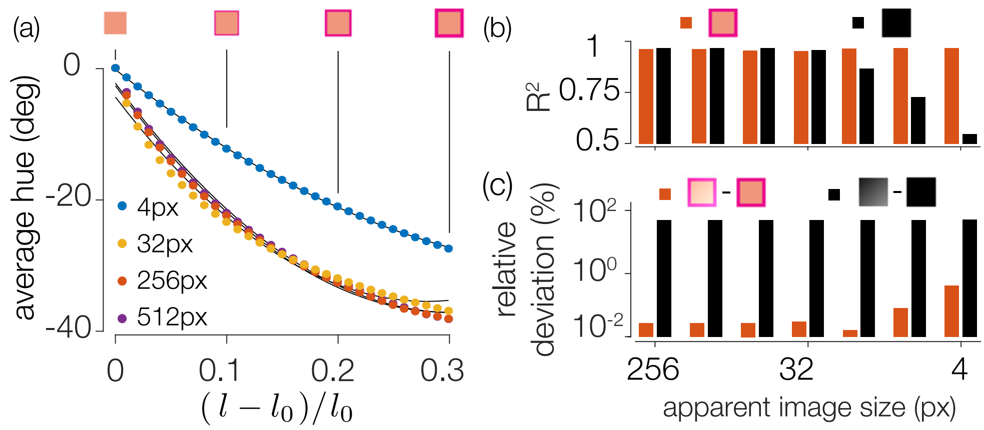


FIGURE 3.7: (a) The hue measurements of the marker are almost insensitive to the apparent size. The simulation showed that the mean hue shifts smoothly towards the hue of the flexible magenta marker. (b) Effects of the apparent size on the accuracy of the polynomial fit. (c) Effects of the non-uniform luminosity on the displacement measurements

Fig. 3.7a shows that even with a apparent size of 4x4 pixels, displacements can be satisfactorily approximated by a second order polynomial fit ($R^2 > 0.98$). We also ran simulations on the effects of changing the pixel density on the estimated size of black and white markers. Fig. 3.7b shows the dramatic effects of decreasing pixel density on the black and white markers, resulting in a steady decrease in the accuracy of the polynomial fit, which goodness of fit reach as low as $R^2 = 0.5$ when the apparent size is 4x4 pixels, while the hue-based method is only slightly affected.

Lastly, in order to gauge the robustness to illumination non-uniformity, we looked at the effect of adding a 25%-opacity gradient overlay. Figure 3.7c reports the difference value of the hue or luminosity for the color-mixing and the black and white method respectively, between the non-uniform and the uniform illumination, relative to the overall range of measurement. This metric compares both methods using a dimensionless number. The results show that the accuracy of the color-based method decreased by less than 1% under non-uniform illumination, whereas the black and white markers have relative error as high as 50%.

### 3.3.5 Manufacturing

Because it relies only on color and transparency, the sensor can be constructed with inexpensive off-the-shelf equipment and materials. The procedure used to make the two layers is presented in Fig. 3.8. First, a soft white compound (SortaClear 12 with Pigment Ignite, Smooth-On, Macungie, PA, USA) is poured into a 3-D printed mould (TPU95A, Ultimaker, Geldermalsen, Netherlands) to form the outer layer of the sensor. The soft material has a Young's modulus of $E = 0.4$ Mpa and a Poisson's ratio of $\nu = 0.5$. The white color serves to block out the light from the outside, while at the same time diffusing the white illumination. Once the outside layer has been cured, a rigid mask is set in place and a mixture of the same soft compound and a magenta dye is screen printed and heat-cured. A transparent layer (SortaClear 12, Smooth-On, Macungie, PA, USA) is cast on top of the magenta markers to fill the holes left by the mask. The transparent layer also protects the markers and sets the right thickness for the sensor, depending on the intended design. All the elastomer compounds are first degassed in a vacuum chamber before being poured into the mold. The rigid base is constructed by bonding a transparent yellow film (Color 410e, Luminis-Films, Peronnas, France) to a transparent acrylic substrate. The squares are cut by laser and the excess film is removed by hand. Lastly, the rigid and soft layers are bonded.

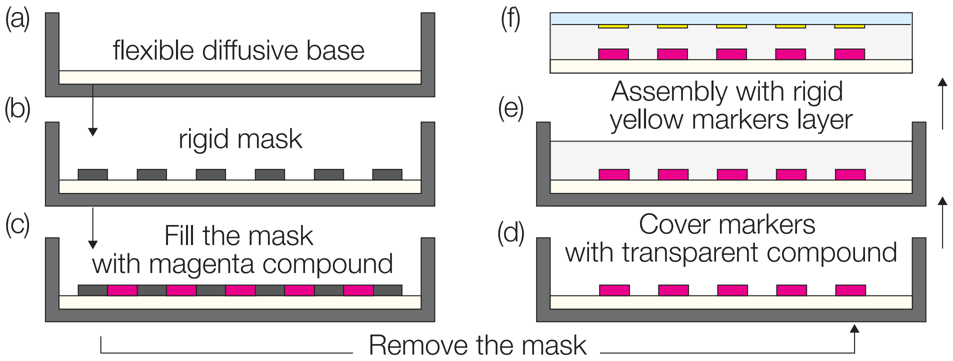


FIGURE 3.8: The production process. (a) A white light-diffusive soft layer is placed in a cast. (b) Once it has been cured, a rigid mask is applied, and (c), the magenta markers are screen printed. (d) After the curing process, the mask is removed and the remaining markers are covered with a transparent compound. (e) The soft part is mounted on the rigid backing support.

The entire process can be performed within 3 days, including the curing. The cost of the raw material is about 4.5 euros in the case of this specific configuration and the process involves only commonly used manufacturing techniques.

## 3.4 Experimental results

### 3.4.1 Experimental Apparatus

Experiments were conducted on a laboratory test bench, a diagram of which is shown in Fig. 3.1c. The soft sensor was fitted into a stack of transparent laser-cut acrylic plates leaving only the top surface accessible for stimulation. Light was provided by 3 LED strips (Neutral White, RS Pro, Corby, UK) mounted on the side of the acrylic support. The light was diffused by the white layer to minimized the presence of any colored shadows and increased the color saturation. A manually adjustable 3-axis translation stage moved a probe with a swappable tip to apply normal and lateral deformation loads to the surface of the sensor.

A high-resolution camera (A7Rii, Sony Corp., Tokyo, Japan) equipped with a zoom lens (24-70mm FE Zeiss, Sony Corp., Tokyo, Japan) set at a focal length of 24mm took high-resolution images of the markers with an aperture of $f/4$ and a locked white balance. With this setup, the deviation of the hue of 50 identical images was as low as 0.3 degree.

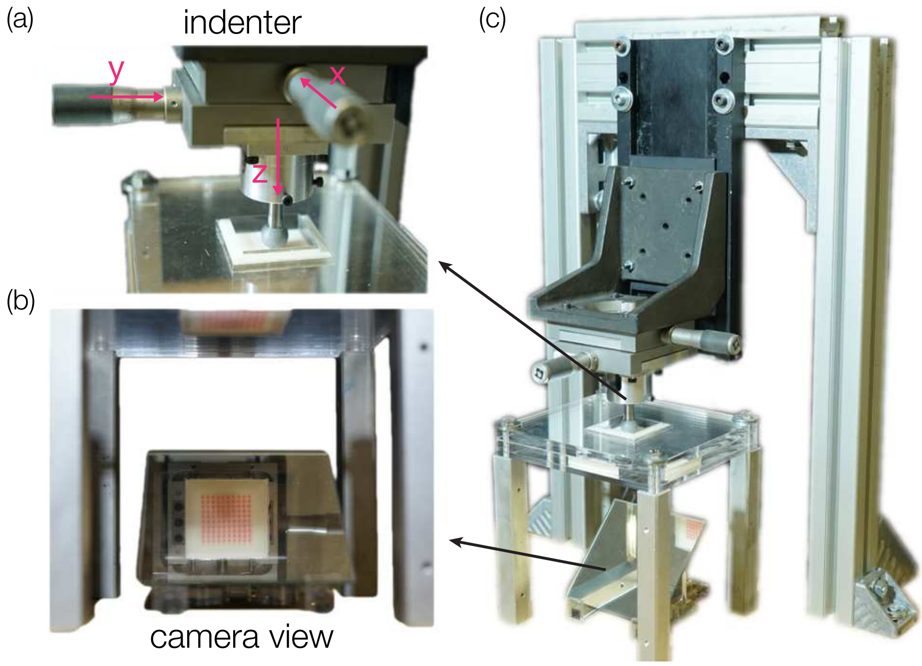


FIGURE 3.9: Experimental set-up. (a) spherical indenter for pressing the sensor in x, y and z directions. (b) Camera view of the sensor using a mirror put at 45 degree with respect to the horizontal surface. (c) Whole set-up.

### 3.4.2 Image processing method

The image processing was performed using Matlab (Mathworks Inc, Natick, USA). The raw images were corrected to even out the nonuniform lighting using a morphological *tophat* filter, and the contrast was then enhanced using histogram equalization methods. The locations of the markers were segmented and labeled using the centroid detection method *regionprops*. At this stage, the location of each marker in the image plane of each marker is determined. In order to assess the normal motion, the image is segmented into regions of interest around each marker. Each region of interest was transformed in the HSV colorspace using *rgb2hsv*. The hue of each pixel which level of saturation was above 50%, ensuring that white pixel were excluded, was averaged to produce the estimation of the mean hue.

### 3.4.3 Single marker calibration

The behavior of one marker was modeled from the displacement data recorded when it was subjected to a 3-dimensional localized external load. The model was then inverted to estimate the displacement field in the case of more complex load distribution, using the superposition principle.

In this experiment, the indenter was a 4 mm diameter sphere, matching the resolution of the marker grid. The normal displacement is correlated with the hue of the marker and the lateral displacement is determined by tracking the centroid of each marker.

To determined the effect of a normal displacement, the indenter was lowered onto the surface and an image was taken every 50 microns step over a 3 mm displacement. The results can be found in Fig. 3.10. The average hue is satisfactorily approximated by a linear trend ($R^2 = 0.99$).

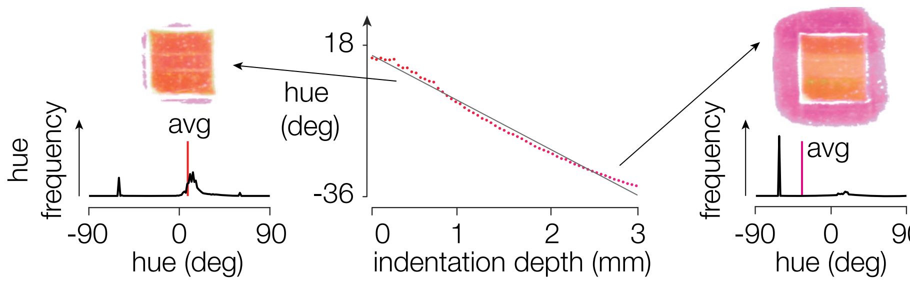


FIGURE 3.10: Direct measurements show the linear relationship between the mean hue degree and the normal displacement of the surface.

The changes in the position of the centroid of each marker also obeyed a linear relationship with the lateral displacement, see Fig. 3.11a. The lateral displacements were applied with a step size of 0.05 mm during a total displacement of 1 mm on the $x$ axis. 15 series of lateral displacements were made by varying the normal indentation depth from 1.5 mm to 3 mm in 0.1 mm steps. By calculating the movement of the centroid of the soft marker under pressure loading, the linear relationships between the lateral displacement and the position of the centroid were determined for all 15 series of lateral movements with various normal indentation depths, as shown in Fig. 3.11b. Since the area of the magenta marker is more visible when the normal displacement is large, the relationship between the lateral displacement and the motion of the centroid $G_{xy}$ was affected by the normal displacement applied to the surface. The value of the linear regression $G_{xy}$ was found to be linearly correlated ($R^2 = 0.93$) with the normal displacement of the surface, see Fig. 3.11c.

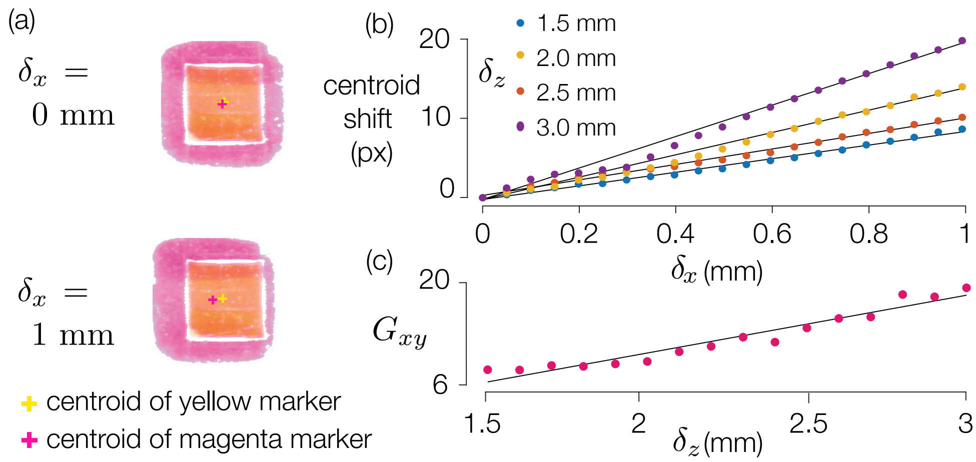


FIGURE 3.11: The direct measurement confirms the linear relationship between the position of the centroid of the magenta marker and the displacement of the surface.

The corresponding behavioral model can be summarized by the following set of equations :

$$h = G_z \, \delta_z + h_0 \tag{3.6}$$

$$c_{xy} = G_{xy} \, \delta_{xy} = (a\delta_z + b) \, \delta_{xy} \tag{3.7}$$

where $G_z$ is the slope of the hue-normal displacement function, $h$ is the hue value and $h_0$ the hue of the marker at rest. The gain $G_{xy}$ between the displacement of the centroid $c_{xy}$ and the displacement of the surface $\delta_{xy}$ is modeled by an affine relationship with a slope $a$ and an intercept $b$.

Once the behavior of a single marker had been measured, we inverted the model to make predictions based on the data recorded. Three series of lateral displacements were applied with normal indentation of 2, 2.5 and 3 mm.

At each step, the indenter pushed the marker along the $x$ and $y$ axes simultaneously in 0.1 mm steps. The calibration process used was specific to the camera and sensor setup used.

The inversion of the model starts by finding the average before determining the normal displacement of the surface. Once this has been done, the appropriate scaling factor is used to determine the actual lateral displacement as a function of the distance.

$$\delta_z = (h - h_0)/G_z \tag{3.8}$$

$$\delta_{xy} = c_{xy}/(a\delta_z + b) \tag{3.9}$$

Linear regression of the curves showed a good fit $R^2 > 0.94$ under all the conditions tested. The errors between the estimated $\hat{\delta}$ and actual displacements were less than 350µ$m$, which can be improved by using a non-linear approximation.

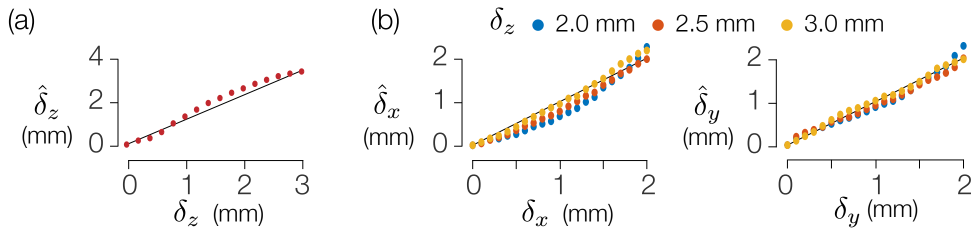


FIGURE 3.12: Validation of the model. (a) Normal to the surface (b) The estimated lateral displacement fit well the actual stimulation for different amount of normal pressure, regardless of the direction.

### 3.4.4 Reconstruction of the displacement field

The inverse model was then applied to the entire grid of markers. The effects of the parallax imposed on the corner markers were small and not compensated. Some examples of the entire scene can be found in Fig. 3.13. With the flat indenter, Fig. 3.13a and b, the maximum deformation occurred on the edge of the shape, in line with the theory of contact mechanics [77]. Likewise, the normal displacement induced by the spherical indenter shown in Fig. 3.13c was in line with the parabolic distribution predicted by Hertz's contact theory. Interestingly, the lateral deformation of the surface was also visible because of the large Poisson's ratio the of elastomeric skin. This lateral radially distributed field, which contains information about the frictional state of both objects in contact, has been used in several robotic applications [120] and is thought to be involved in the perception of adherence in human tactile perception processes [75].

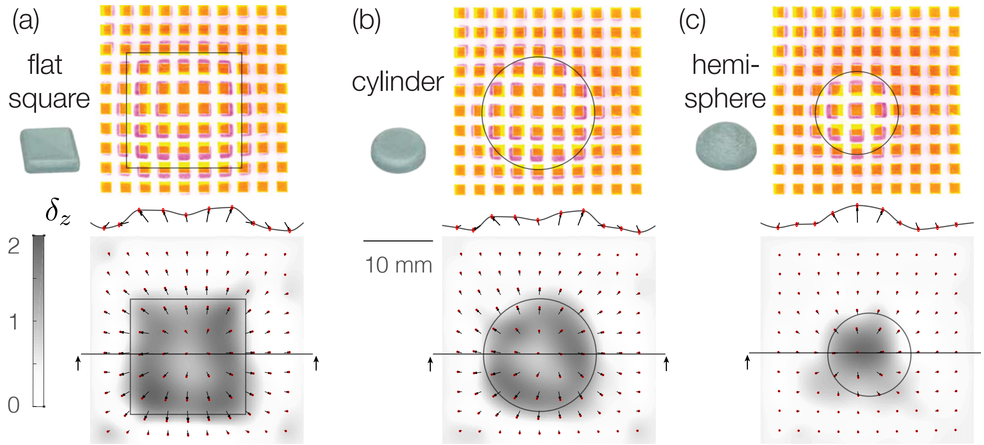


FIGURE 3.13: Experiment with a square (a), a cylindrical (b) and hemispherical (c) probe. The normal distribution is in line within the literature and the direction of the deformation vector hints at the work of friction. For all the estimated displacement map, interpolation was applied over inferred normal indentations over each marker.

## 3.5 Conclusion and limitations

We introduce a new approach to measure 3d displacement field with a camera-based tactile sensor. The fastidious process of encoding the normal displacement is done through the use of the color channels allowing to capture both the normal and lateral displacement of an array of colored markers with a precision that corresponds to 2% of the original size based on the color pattern produced when transmitted through a reference translucent array.

Finding means of measuring the distributed 3-dimensional interactions that occur in the contact area between a surface and an external object is crucial to determining the properties of the material such as its shape or its compliance, along with the dynamics of the contact, especially the occurrence of any incipient slippage. Tactile sensors have been found to be of great benefit in the field of robotic surgery [64, 196], and prosthesis [136].

The design principles and experimental results show that this sensor is suitable for gauging the distributed 3-dimensional motion of a surface to which complex stress field involving friction can be applied. However, suitable means of measuring the force applied to the surface still remain to be developed. A localized force applied at the center of the sensor will induce a displacement which has visible effects on all the markers and deconvolution methods [61] can be used to determine the stress and traction forces exerted at the surface from the markers data.

## 3.6 Future work

Further investigations will focus on perception of interactions and object properties, such as contact force, object shape and friction, especially in the scenario such as grasp adjustment after a perturbation, or measuring the compliance of an object. The silicone-based sensor is highly compliant, which is useful for the automatic control of grasping, human-robot interactions and teleoperation.

In the case of extremely large displacements, it can happen that the soft markers will be visible between two transparent filters. In this case, the single marker approach will not be appropriate. Since the sensor consists of two regularly spaced grids of markers, a large scale interference similar to the Moiré pattern will be observed. Viewed from afar, the colored fringes produced by the sensor provide information about the shape of the object and the friction forces at work.

## Acknowledgment

The authors would like to thank Julien Diperi and Stéphane Viollet for enlightening discussions.

Chapter 4

# Curvature estimation

## Contents



Adapted from: Lin, Xi, et al. "Curvature sensing with a spherical tactile sensor using the color-interference of a marker array." 2020 IEEE International Conference on Robotics and Automation (ICRA). IEEE, 2020.

# Preface to Chapter 4

The previous chapter proposed a camera based tactile sensor using subtractive color mixing principle for measuring 3d displacement field. Based on the same sensing method, this chapter introduces a hemispherical version, which is beneficial for exploring arbitrarily shaped objects. The manufacturing inspired from fabrication procedure of the spherical globe is detailed. Then a curvature estimation algorithm based on Hertz contact theory was proposed and validated by experiments, showing that the sensor is able to estimate the curvature of the object via a simple press. With this curvature estimation, the sensor could help the robot to find the optimal grasping location in future work.

## Abstract

The only way to perceive a small object held between our fingers is to trust our sense of touch. Touch provides cues about the state of the contact even if its view is occluded by the finger. The interaction between the soft fingers and the surface reveals crucial information, such as the local shape of the object, that plays a central role in fine manipulation. In this work, we present a new spherical sensor that endows robots with a fine distributed sense of touch. This sensor is an evolution of our distributed tactile sensor that measures the dense 3-dimensional displacement field of an elastic membrane, using the subtractive color-mixing principle. We leverage a planar manufacturing process that enables the design and manufacturing of the functional features on a flat surface. The flat functional panels are then folded to create a spherical shape able to sense a wide variety of objects.

The resulting 40mm-diameter spherical sensor has 77 measurement points, each of which gives an estimation of the local 3d displacement, normal and tangential to the surface. Each marker is built around 2 sets of colored patches placed at different depths. The relative motion and resulting hue of each marker, easily captured by an embedded RGB camera, provides a measurement of their 3d motion. To benchmark the sensor, we compared the measurements obtained while pressing the sensor on a curved surface with Hertz contact theory, a hallmark of contact mechanics. While the mechanics did not strictly follow Hertz contact theory, using the shear and normal sensing, ChromaTouch can estimate the curvature of an object after a millimeter-size indentation of the sensor.

## 4.1 Introduction

Robots interact with their surroundings by sensing and reacting to the mechanical behavior of the environment, usually through an impedance control feedback loop [60]. In a classical impedance control, the mechanical interaction with the environment is measured with a force sensor and serves as a basis to control the motion of the robotic arm at modulating its apparent stiffness. Yet, perceiving the mechanical world with only a single point of measurement discards the abundance of information that the mechanical scene has to offer. A single 6-axis force sensor can indeed be used to find the timing, location, and direction of a contact force [12, 65] but the limited spatial distribution of the data prevents the estimation of the shape and the surface properties of an object without active exploration [144].

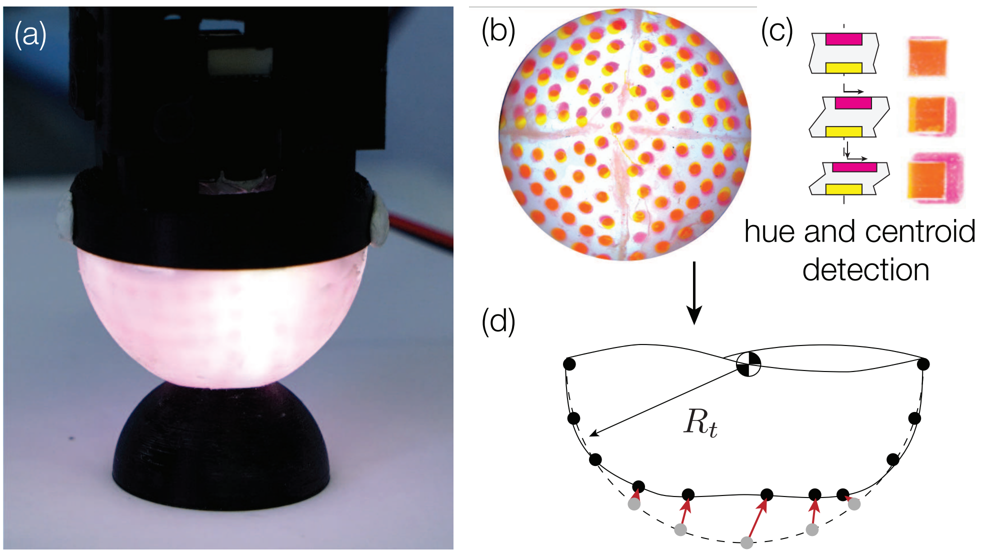


FIGURE 4.1: (a) The sensor, mounted on a robotic arm, explores an object (b) Typical image retrieved by the embedded camera (c) Effect of lateral and normal forces on the shape and hue of a marker. (d) After calibration, the lateral and normal deformation of each point is estimated.

Humans also use proprioception to gather kinematic information to control the impedance of their limbs, but what set them apart is that they are endowed with a rich sense of touch, mediated by a collection of mechanoreceptors, densely populated in the fingertips. This wide-ranging array of mechanoreceptors encodes the complex mechanical interaction that occurs at the contact between the skin and the object. The sense of touch captures surface features [191, 88], compliance of materials [168, 49] or the presence of edges [141]. Of importance for the present work, an estimate of the curvature of an object can be extracted from a single press [52] and guide the timing of motor commands required for grasping and object manipulation [14, 75].

Given the usefulness of touch in manipulation, it is not surprising that tactile sensors for robotics have shown great promise in providing a rich image of the mechanical interaction on a par with human perception. A large variety of strategies can be used to transduce the mechanical deformation into an electrical signal, for a full review the reader can refer to [34].

Amongst these techniques, camera-based tactile sensors attract increasing attention due to their higher spatial resolution and minimum wiring requirement compared to other tactile sensing technologies.

These sensors typically use a camera to track the displacements of markers embedded in a soft elastomer. This method delivers dense tactile images with a relatively fine temporal resolution when leveraging high frame-rate cameras [148, 115]. However, except for a few exceptions detailed in the next section, these sensors usually are limited to measuring lateral deformation, which provides valuable measurements but requires complex processing and approximations to gauge the normal motion of each marker.

The ChromaTouch sensor, introduced previously [106], solves the problem by encoding the normal motion of each marker in the color channels of the camera, effectively converting a 2-dimensional color image information into 3-dimensional deformation field. Each marker is made by 2 overlapping submarkers, one diffusive and magenta, the other translucent and yellow. The full 3d relative motion of the submarkers is found from both the centroid detection and the change of hue of the marker. We demonstrated the effectiveness of this transduction principle to detect dense 3d displacement fields on a flat sensing surface. The long-term goal of the work is to integrate this sensor in with a robotic end-effector with curved fingertips. In this paper, we introduce a new version of ChromaTouch that uses the color-mixing transduction principle on a hemispherical sensing surface, able to explore surfaces with arbitrary shapes, see 4.1a. The sensor embeds a camera equipped with a fisheye lens, which has the double benefit of amplifying the signal used to estimate the normal displacements as well as unwrapping the spherical projection of the sensing hemisphere, see 4.1b. Figure 4.1c, illustrates the sensing method. After calibration, the sensor retrieves the 3d deformation field at the location of the markers which can be interpolated into the full deformation of the body, see fig 4.1d.

## 4.2 Related work

### 4.2.1 Camera-based sensors

The success of camera-based tactile sensors can be attributed to the decades of engineering that refined camera sensors and allowed converting photons into digital data. By relying on off-the-shelf camera, these sensors bypass the electronic engineering that is required to make capacitive and piezo-resistive tactile sensors. For this reason, camera-based sensors often boast larger resolution and higher refresh-rate.

Camera-based tactile sensors rely on a deformable medium seen by the camera, which essentially converts the mechanical interaction into a visible change of the image. Therefore, the necessary inventiveness to extract data about the contact lies in the engineering of this medium. The simplest method is to place black markers on a white background on a soft elastomer and track the motion of these markers to infer the interaction at the contact. The biomimetic approaches suggest amplifying motion via an array of pins attached to a deformable membrane [186]. However, the transduction from the 2D optical image to a 3D mechanical deformation field remains a challenge [46], mainly because the distance from the markers to the camera is unknown.

GelForce developed by Sato et al. [148] employing double layers of rigid markers to compute the 3D stress field. The normal stresses are calculated from the lateral distribution of the markers. This implementation is effective but the spatial resolution of the sensor is limited, because the markers on both layers cannot be overlaid. The GelSight sensor measures the topography of an elastomer covered by a light-reflecting membrane illuminated from 3 sides by 3 lights of complementary color. The 3d geometry of the deformation of the gel is reconstructed from the shadow of the asperities in contact with the membrane. The sensor has been used with added markers to measure the slip and shear at the contact [204, 115]. Because of its working principle, these sensors can only be planar or have small curvature, and therefore accommodate well only with convex objects. In Kappassov's work [87], the tactile sensor uses the change of color to determine normal pressure with $3\times3$ markers.

The ChromaTouch sensor builds upon these principles and extends to the recovery of the full displacement field to gather a complete picture of the contact.

### 4.2.2 Spherical-shaped sensors

Soft spherical-cap artificial fingertips are popular in robotic grasping as they help stabilizing the contact with an arbitrarily shaped object. Therefore, a large body of research has created artificial fingertips with spherical or complex convex shapes.

A wide array of manufacturing strategies has been deployed. Casting the body of the sensor in a spherical mold, with grooves results in structures with soft and complex shape that can even incorporate markers if the grooves are included in the mold [146]. Another popular fabrication method makes use of 3d printing with soft elastomer. 3d printing offers a versatile method for producing complex-shaped sensors [186]. One of the downside of spherical sensors has to do with the fact that circular markers on a sphere will appear as ellipses when projected on the image plane. Several sensors subsequently require image wrapping to recover the proper shape of markers [146].

Alternatively, piezoresistive and capacitive sensors can be mounted on a flexible printed circuit board that is cut and wrapped around a rigid core, then covered with a rigid layer [150]. The cover filters and blurs the signal from the contact thus markers benefit from being near to the surface [163].

## 4.3 Convex sensor to measure flat, convex and concave objects

### 4.3.1 The case for spherical shape when exploring objects

Simple reasoning can highlight why a curved sensor is beneficial for the versatility of sensing with arbitrary objects. It allows the sensor tip to conform to the touched object with a larger contacting surface [44, 132]. The shape and size of the contact surface are determined by the relative curvature at the contact point. Assuming concave or convex spherical sensor and object, the relative curvature can be expressed as $C_r = R_t^{-1} + R_o^{-1}$, where $R_t$ is the radius of the sensor, and $R_o$ is the local radius of the object, near the contact point. The radius is positive for the convex object and negative for the concave object. When the object is flat, the radius is infinite and the curvature of the object is null. If both the sensor and the objects are flat, the relative curvature is null, and in this special case, the contact is made on the higher asperities of both surfaces, therefore, relying on stochastic properties and being ill-defined at macroscopic scales [67].

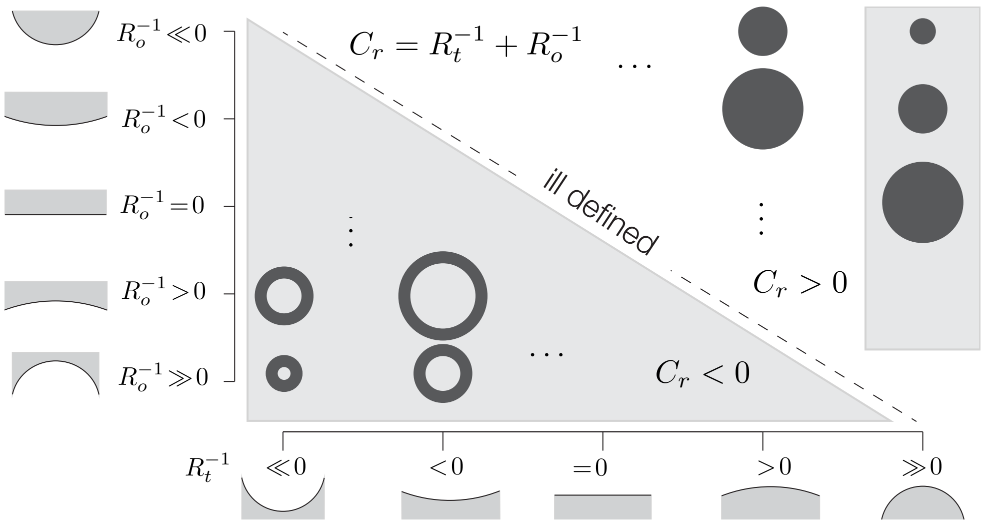


FIGURE 4.2: Shape of the contact between a sensor with curvature $R_t^{-1}$ and an object with curvature $R_o^{-1}$. When relative curvature $C_r$ is null, the contact topology is ill-defined. Since the environment of the robot contains objects of undefined curvatures, a small radius will provide the best versatility. The shaded area shows the operating range of curvature that spherical sensors can typically sample.

On the other hand, when the relative curvature is negative — the concave object has a smaller radius than the convex object — the contact is made at the edge of the convex object and therefore the mechanical interaction is discontinuous. From a sampling point of view, in order to have an uninterrupted contact surface, the best choice is to have positive relative curvature (see Figure 4.2). In this case, the contact follows Hertz theory and the contact area is elliptical. A summary of Hertz contact theory could be found in Appendix A.

This result is well known by the mechanical community and is the reason why surface scanning instruments have small diameter tips and can capture the small-scale changes in curvature [67].

### 4.3.2 Flat to curved projection

The manufacturing of the double overplayed layer needed for ChromaTouch requires the alignment of magenta and yellow dots on two different planes. This sensitive operation is relatively straightforward to process on flat surface but challenging when the alignment must be done on a curved surface, such as a sphere.

Gauss' *Theorema Egregium* provides an opportune framework to understand how to design a flat part that can be folded. The remarkable theorem states that the gaussian curvature $\kappa$ — defined by being the product of each principal curvature — of a surface is invariant under bending. A flat plane of gaussian curvature $\kappa = 0$ can be bent along one dimension for which one of the principal curvatures will be non-zero, but cannot be deformed into a sphere for which both principal curvatures will be the reciprocal of the bending radius $R_b$, i.e. $\kappa = 1/R_b^2$. Since bending and folding are not sufficient to make the sphere, in our production process, the surface has to be stretched or cut.

To work out a way around this fundamental constraint, we used a production method that is popular for making spherical globes from flat maps. The sphere is divided into $n$ gores (i.e. segments), each of which can be worked on as it is a flat surface. In globe production, each of the gore contains a part of the map so that the shape and linearity of the meridian are preserved. Once the gores are printed, they are folded into a sphere to make the globe. The fold introduced a small distortion as the flat gores still must be bent in both directions. However, as the number of gores increases, the bend along the equator is less pronounced and the distortion induced by stretch is reduced. In our case, because we are using compliant elastomers which forgive some stretch, cutting the sphere in 4 gores was enough to ensure an easy manufacturing process, while reducing the number of seams.

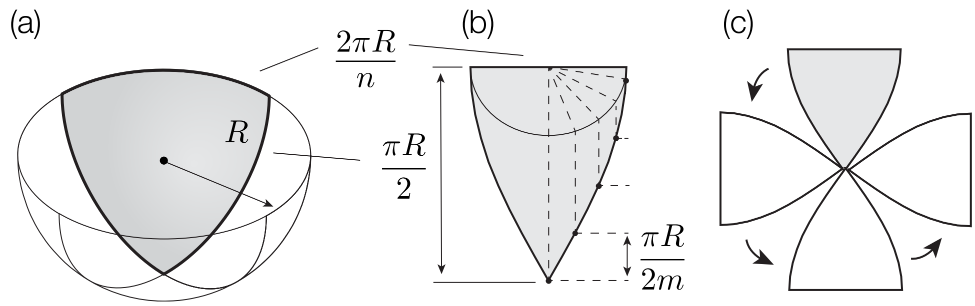


FIGURE 4.3: Construction of the polyconic pattern. (a) One of the $n^{\text{th}}$ segment — called gore — of the sphere (b) is constructed by projecting $m$ regularly spaced points of an inner circle whose diameter is the equator of a segment onto a regular line grid spaced by $\pi R/2m$ (c) The segment is then copied $n$ times and rotated around its apex to produce the final flat pattern.

Figure 4.3 illustrates the process used to create the shape of the gores and assemble them into a spherical cap of radius $R$. The shape of each gore is found by constructing a semicircle with a diameter the equatorial edge of length $2\pi R/n$. Then we divide the inner circle in $m$ radii and project the vector field onto a regularly spaced grid of which extend from the equator line to a parallel line spaced by $\pi R/2$. Placing the markers onto the flat gores is effortless compared to assembling them on a spherical surface. Regular manufacturing techniques such as printing, laser cutting, molding can be used to create the required pattern.

### 4.3.3 Manufacturing process

The manufacturing process illustrated in figure 4.4 is an update from the original flat version. First, the base is cast from transparent elastomer (Sortaclear 12, Smooth-On, Macungie, PA, USA) in a high-resolution 3d-printed mold. The grooves left by the cast are filled with the magenta markers, made from the same elastomer in which a dye is added. Then, a protective layer is molded, on top of which the yellow filter is placed. The yellow elements are laser cut and the rest of the film are discarded. A protective transparent layer embeds the yellow transparent submarkers. The whole operation including curing takes approximately 2 days.

At this stage, the manufacturing process requiring the part to be flat are completed and the pattern is folded onto a rigid and transparent sphere made of acrylic. Lastly, the white outer layer is cast onto the exterior of the sphere to ensure the proper cohesion of the gores. The last external layer also acts as a barrier for external light and as a diffuser for the marker

### 4.3.4 Assembly and optical image correction

Within the current limit of our off-the-shelf manufacturing process, we can create spherical sensors with 77 markers measuring 2 mm in diameter and distributed on the meridians of a sphere of radius 40 mm. A USB-camera (Aria A15S-C, Alkeria, Cascina, Italy), with a 1/2.9″ image sensor, is placed at the center of the sphere. The camera is fixed onto a mounting fixture that is linked to the force sensor of the robot arm. The overall assembly of the sensor is shown in figure 4.5a.

The camera is equipped with a f = 2.2 mm fisheye wide lens (Lensagon BF5M2223S129, Lensation GmbH, Karlsruhe, Germany). As found previously [106], the interference of the marker is most notable when the lens has a short focal length, which provides a better signal to noise ratio. The fisheye lens has a 180° field of view, which usually creates a characteristic distortion due to the equidistant projection. However, in this case, each marker is at the same distance from the focal of the lens and cancels exactly the distortion made by projecting the markers onto a plane. The image created by the combination of the fisheye lens and spherical marker array creates an image without needing post-processing for image distortion.

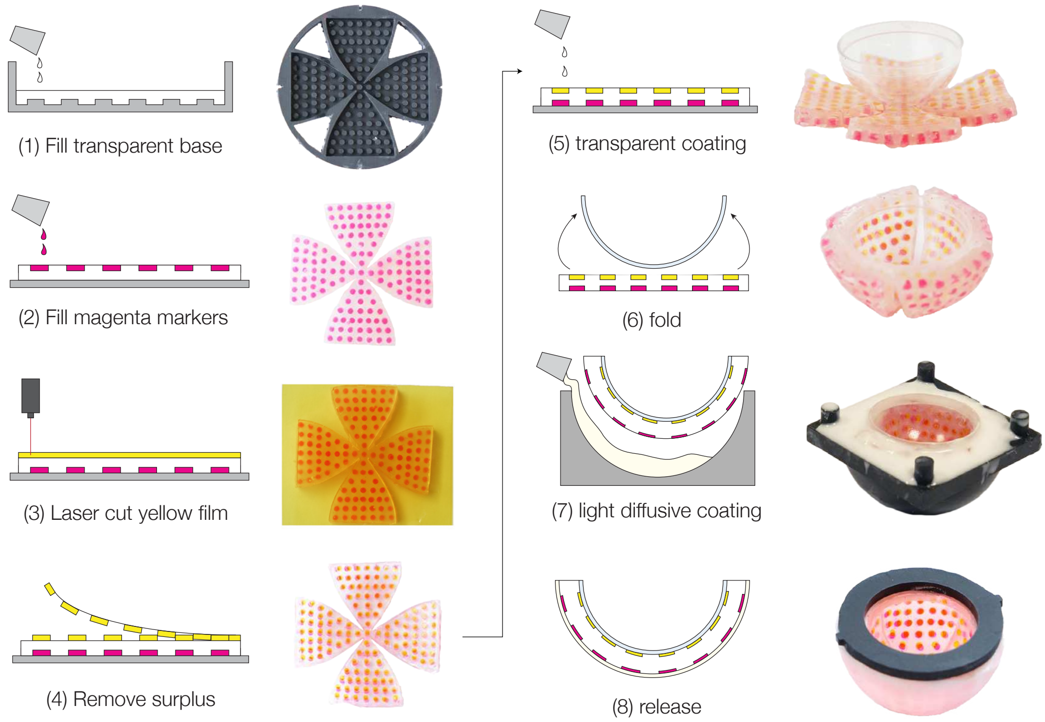


FIGURE 4.4: Manufacturing process. A flat mold makes alignment of the magenta and yellow marker easier. Once the flat pattern is completed, it is folded into a spherical shape, and held in place by curing additional elastomer, which acts as a diffuser for the illumination.

### 4.3.5 Signal processing

The 3-dimensional displacement of each marker with respect to the camera depends on the observed lateral displacement of the centroid and the change of hue of their projection on the image sensor. To convert the image into a vector field, a processing pipeline is as follows. First, the raw images from the camera are cropped using a circular mask to remove everything outside of the edge of the sensor. Then a *tophat* filter is applied to mitigate the effect of non-uniform lighting and the contrast is enhanced. Once the correction is done, the images are converted from RGB to HSV color space. The hue channel is used to segment the markers by thresholding around the yellow and magenta hue. The centroid of each magenta marker is detected from the binary images using the *regionprop* function in Matlab. The mask is used to isolate the marker in the original image. For each marker, the average hue is stored. At this stage, we have the hue, which reflects the normal displacement, and the motion of the centroid in 2 dimensions, which reflects the lateral displacement of the markers.

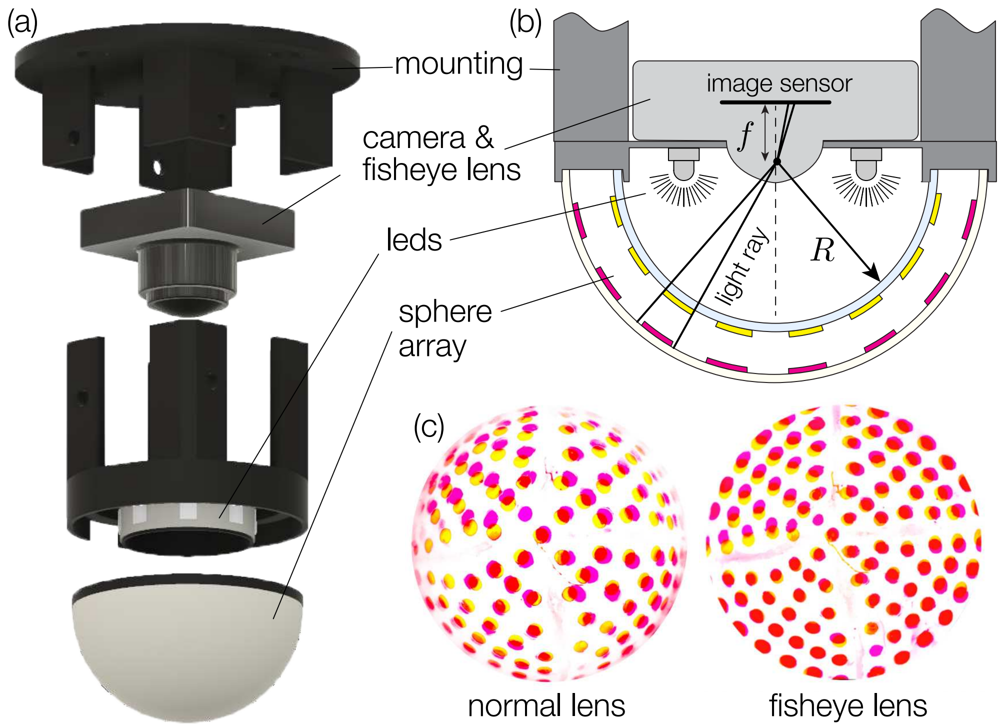


FIGURE 4.5: (a) Exploded view of the assembly. (b) The fisheye lens creates a flat projection of the spherical array, canceling the distortions. The markers have similar area throughout the image.

## 4.4 Experimental validation

### 4.4.1 Calibration

The link between the hue of the marker and the actual displacement it experiences is influenced by the construction, illumination, and camera parameters. Therefore, this relationship needs to be calibrated against a ground truth.

The calibration is done by pressing the sensor onto a flat plate, with a robot (UR3, Universal Robots, Odense, Denmark) equipped with a force-torque sensor (FT300, Robotiq, Lévis, Canada) to measure interaction forces. During a normal loading experiment, the force and the displacement of the robot are recorded to provide ground truth for the load curve of the system. At the same time, the state of each marker is determined to find the distribution of the displacement over the contact area.

As shown in figure 4.7a, the external force $P$ applied by the robot will induce a deformation $\delta_r$ of the soft sensor if the contacting surface is infinitely stiff compared to the compliance of the soft elastomer of the sensor. This deformation $\delta_r$ also corresponds to the maximum of the deformation field measured by the tactile sensors, independently of the curvature of the object.

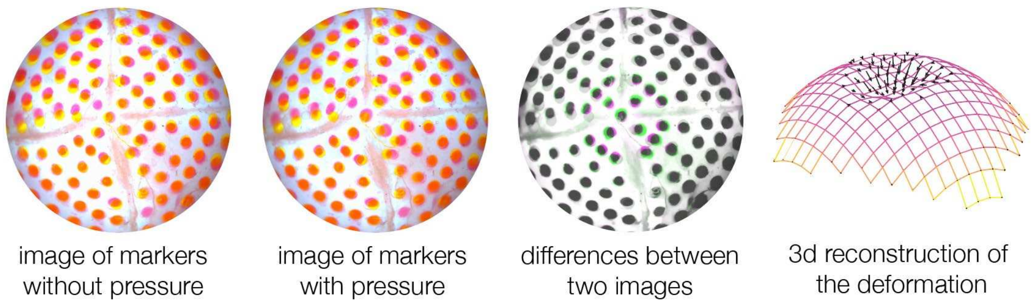


FIGURE 4.6: Comparison of the sensing image before and after pressure, and the reconstruction of 3d displacement field.

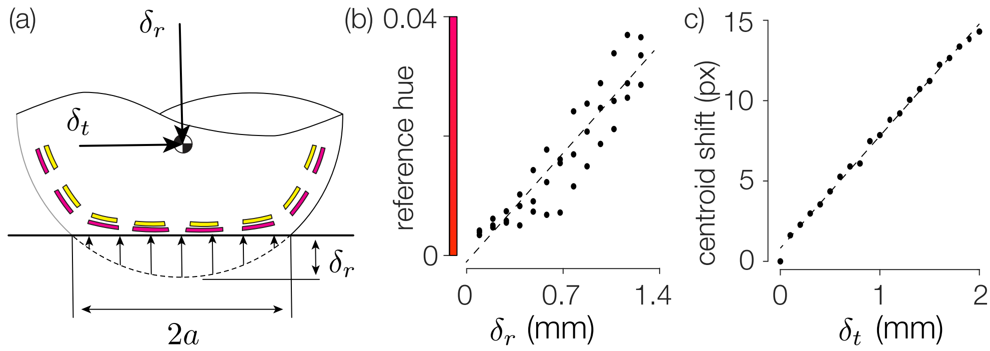


FIGURE 4.7: (a) Effect of pressing the spherical sensor on a plane (b) The reference hue as a function of the normal displacement of the robotic arm, and its linear fit in dashed line. (c) Results from the tangential calibration.

Therefore, we can use the ground truth values to calibrate the variation of observed hue.

Figure 4.7b, shows typical traces obtained during calibration. The relationship between the hue of the marker that experiences the maximum deformation (i.e. located in the center of the contact patch) and the displacement recorded by the robot is invariant with the curvature of the contacting object. A linear fit gives the coefficient to extrapolate the displacement from any arbitrary observed hue. The goodness of fit on the sampled data is $R^2 = 0.89$. A similar procedure is done for the lateral displacement with the goodness of fit $R^2 = 0.99$, see figure 4.7c.

### 4.4.2 Example application: model-driven curvature estimation

Once the relationship between the observed hue and the displacement is established, we can reconstruct the 3d displacement field of the sensor from the observed images sampled at the location of the markers. The data is then interpolated again to provide a regularly spaced sampling.

The contacts with two curved objects of radii $\pm 80$ mm and a flat surface are illustrated in figure 4.8. The image reveals a difference in the extent to which the markers are disturbed. The measured displacement field reveals the nature of the interaction. The field shows a peak at the center of the contact that tapers as the edge of the contact in a monotonic fashion. It is interesting to note that the local contact force is not strictly normal to the surface but has a slight angle due to the work of friction and elastic stretch. The measurement of the lateral motion has importance in evaluating the shape of the normal deformation since the markers moved. The red dots in Fig 4.8 show the normal displacement at the original radial location of the markers.

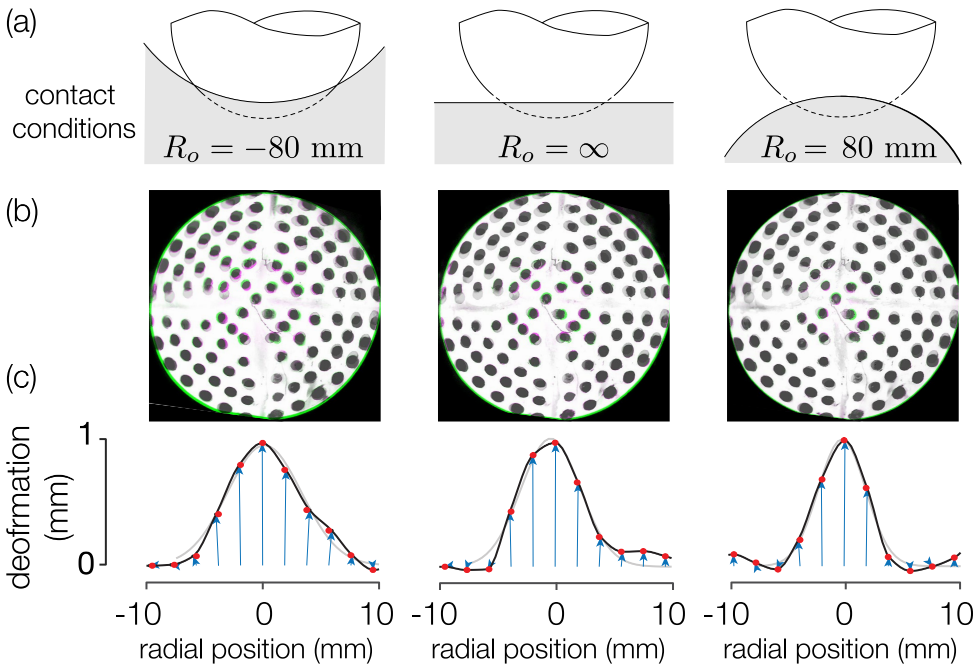


FIGURE 4.8: (a) Comparison between Hertz contact theory and measurement given by the sensor when pressing on a negative, null and positive curvature object. (b) The image difference between the normal state and the deformed state is affected by the curvature of the object. The negative difference is in magenta and the positive in green. (c) The resulting profile of the displacement of the middle cross-section of markers. The vectors show the actual displacement of each marker, the red dots highlight only the normal motion and the gray curves show the result of curve-fitting with a filtered Hertzian contact.

The Hertz contact theory can be used to analyze the measured displacement and extract the radius of the contacting body [77]. In the following paragraph, the assumption is that the object is infinitely rigid compared to the soft fingertip. The theory first observes that the contact area between two spherical objects will lead to a circular contact area of radius $a$. The relative displacement of the two bodies $\delta_r$ is related to the contact area $a^2$ by the equivalent radius $R = (R_s^{-1} + R_o^{-1})^{-1}$ such as:

$$a^2 = R\delta_r \tag{4.1}$$

where the effective radius is calculated with the radius of the sensor $R_s$ and the radius of the object $R_o$ in contact. This equation can be reversed to find the radius of the object from the displacement and the area of contact, knowing the radius of the object.

According to Hertz theory, the contact at the surface should lead to normal displacement $u_z$ of the soft body which follows a parabolic shape such as:

$$u_z(r)|_{z=0} = \delta_r \left(1 - \frac{r^2}{2a^2}\right) \tag{4.2}$$

where $r$ is the radial coordinate. Curve fitting this relationship to the displacement field of the contact surface, could in theory resolve from tactile data the displacement of the sensor and the area of the contact patch. However, the measured displacements from ChromaTouch come from the markers that are embedded deeper in the elastomer. The elastomeric layer that covers the markers acts as a mechanical filter and blurs the contact distribution. Figure 4.9a illustrates the filtering done by the soft tissues, which can be estimated from Boussinesq-Cerruti equations that are widely used for solving half-space contact problems at any point of an elastic body under a pressure. Using the pressure given by Hertz contact model by $p(r) = p_0 \left(1 - \frac{r^2}{a^2}\right)^{1/2}$, where $p_0$ is the maximum pressure given by $p_0 = \frac{3P}{2\pi a^2}$, the displacement field at a certain depth of the elastic body could be expressed by a function which is difficult to fit with the estimated displacement of the markers because of its complexity. In order to simplify this fitting procedure, the distribution under the filtering effect is approximated by a gaussian curve:

$$u_z(r)|_{z=2\text{mm}} = \delta_r e^{(-r^2/a^2)} \tag{4.3}$$

from which the amplitude is the global displacement and the deviation is related to the area of contact. The gaussian approximation has a goodness of fit with the theoretical deformation of $R^2 = 0.96$.

We conducted measurements on three spherical objects mentioned earlier. Figure 4.9b shows the estimation of the area of contact $a^2$ extracted from the gaussian fit, when the normal displacement of the robot increases. The radius of the contact area increases with the applied normal displacement. The equivalent curvature is computed from the deformation field. Figure 4.9c reveals that the equivalent curvature converges to the actual curvature when the normal displacement increases, although some discrepancies exist. For indentation lower than a millimeter, the noise of measurement has a significant influence on the quality of results. After a normal displacement of 1 mm, the estimation converges to the real value. When the total displacement reaches 1.4 mm, the estimations of the effective radius $R$ corresponds well the desired values, which are $R = \{26.7\text{mm}, 20\text{mm}, 16\text{mm}\}$ for the sensor with the radius of $R_t = 20$ mm in contact with objects with the radius of $R_o = \{-80\text{mm}, \infty, 80\text{mm}\}$ respectively.

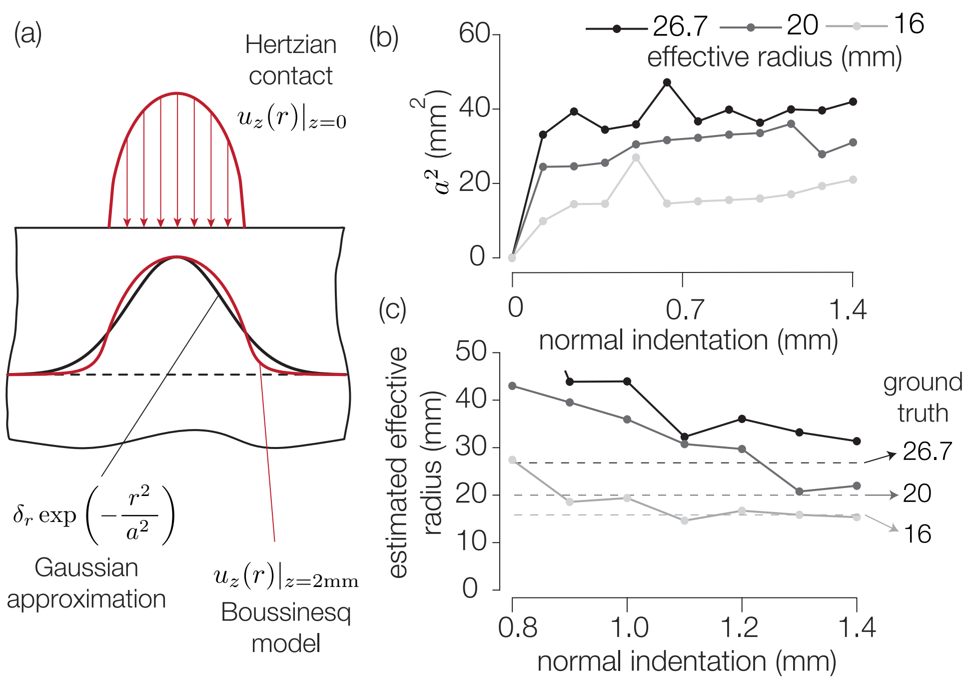


FIGURE 4.9: (a) Sensors embedded in the elastomer inherently observe a blurry picture of the contact. (b) Evolution of the contact area as the sensor is pushed into a curved object. (c) Results of the estimation of the curvature at the beginning of the press. The estimated effective radius (plain lines) converge to the real value (dashed lines).

## 4.5 Discussion and conclusions

### 4.5.1 Discussion

Tactile sensors are essential tools to enable robots to haptically explore their surroundings, perceive changes in contact conditions and subsequently accomplish dexterous manipulation tasks. The spherical shape associated with the use of soft elastomer offers tactile sensing as well as intrinsic stability when grasping. The color subtraction method, presented in this work, enables access to the shear as well as the normal components of the deformation, which is theoretically enough to reconstruct the stress pattern at the surface. The current work shows that the deformation of the sensor is in good agreement with the Hertz contact theory despite showing some striking differences.

During the experiment, we made sure that the contact was lubricated, therefore as close to frictionless as possible, to follow the assumptions underlying Hertz contact theory. Upon contact, the section touching the object expanded laterally to maintain its surface area. The displacement of individual points did not follow a pure normal path but was also shifted toward the outside of the contact patch contrary to the prediction of Hertz theory in which the displacement is purely normal. The discrepancy with the linear small-strain theory of Hertz is most certainly due to large deformations of the soft layers of the sensor. The lateral motion could be used to estimate slipperiness of the surface without having to slide the sensor laterally. Some evidence shows similar capabilities of friction perception while pressing in humans [120, 125].

Lastly, the lateral calibration is performed only at one normal force, but it appears to be affected by the indentation depth, which translates into an underestimation. Finer calibration procedure should lead to even more accurate results.

### 4.5.2 Future improvements

The analysis of the experimental results suggests several essential improvements. First of all, the rigid core inside the sensor should be removed to have a more linear deformation pattern and to avoid saturation of the sensor at higher loads. Along those lines, future sensors will use a softer compound to maximize the deformation and color changes of the markers inside the sensor.

Second, in this study, the sphere was made using four gores which is practical from the standpoint of folding but still induces too much stress and distortion when wrapped around the spherical core. The sweet spot between low distortion and ease of manufacturing might be closer to 6 or 8 gores. Increasing the number of markers to provide better spatial resolution will offer the possibility of digital spatial filtering that can improve the signal to noise ratio.

Lastly, the calibration procedure will be replaced by a machine-learning approach in the hope that it considers the deviation from the calibration of each marker.

### 4.5.3 Conclusion

This work presents a new hemispherical version of the camera-based tactile sensor developed before. The sensor can measure the 3d deformation field of the contact via marker tracking and hue detection. With the hemispherical configuration, the sensor is suited to explore surfaces with arbitrary curvature even if the object is slightly concave. We proposed an algorithm to estimate the curvature of the object with a 1 mm indentation on the object. Experimental results show a good agreement between the estimated effective radius and the real value despite using Hertz contact in the presence of friction. Future work will solve the existing limitations of the sensor and extend the application of the sensor to robotic manipulation tasks.

# Chapter 5

# Friction estimation

## Contents



This chapter will be submitted under the title: X. Lin, P. Kulkarni, M. Wiertlewski. One-touch Sensing - Tactile perception of friction and shape on initial contact

## Preface to Chapter 5

The previous chapter proposed a hemispherical shape of the sensor for estimating the curvature of the object by a simple press. Taking the advantage of the estimation of local curvatures, robots could adjust their grasping points to maximize grip stability. However, this estimation did not take into account that concave sections of the object might be slippery, leading to unstable grasps. In this chapter, we present a method for estimating the friction of a surface via simple press along with the topography of the surface. Taken together, these results could endow robots with the ability to adjust grip force in the instants following the initial contact. The sensor used in this chapter was improved from the planar sensor presented in chapter 3 with 4-times higher spatial resolution. The calibration of the sensor was performed using a convolutional neural network (CNN) to derive a more accurate measurement of the normal displacement field used to estimate the local shape. Another CNN model was trained to predict the local coefficient of friction from the tactile images. Experiments were carried out, showing that the sensor is able to distinguish different frictional states on the same contact surface. This sensing capability could allow robotic hands and gripper to adjust the location of their grip to a less slippery area if the target object has a nonhomogeneous frictional property.

## Abstract

Successfully grasping and manipulating an object with a robotic gripper depends strongly on the ability to regulate the grip force, to allow for some controlled slippage while avoiding catastrophic sliding. To this end, an early estimate of the coefficient of friction of the object-skin is paramount to achieve this delicate balance. Here, we present a tactile sensor and calibration procedure, permitting an estimate of the frictional interaction at the very instant the finger comes into contact with the object.

The sensor comprises 441 marker points, composed of two overlaid layers of colored markers. The relative motion and the color change of the overlaid markers, captured by an embedded color camera, encode the 3d deformation of the sensor under pressure. After the calibration, the visual variation of the marker is used to infer its motion within the surface and estimate the local friction. When pressed against a high-friction object, the membrane of the sensor remains attached to the object, limiting the amount of lateral motion of

the markers. Conversely, in low friction conditions, the membrane is allowed to slide, creating more noticeable movement. Convolutional neural networks are employed for calibrating the sensor and training the friction estimation model. After the training, the algorithm learns to use the lateral deformation to estimate complex frictional patterns, such as a curved shape with both high and low friction region, at the initial contact between finger and object.

## 5.1 Introduction

Modern robots and grippers boast new perceptual capabilities, owing to the information retrieved by tactile sensors. These sensors provide crucial knowledge of the state of contact and the physical properties of the object that vision alone cannot provide. While vision allows to globally estimate the shape and orientation of an object – useful for reaching–, the tactile sensors provide a sense of the pressure, friction, and material properties that are unique to touch. These tactile cues are essential to capture a rich haptic scene of the contact, conveying potential slippage, the stability of the contact and the robustness to external perturbations. More importantly, they are the bedrock for solving one of the outstanding challenges in robotics: automated grasping and manipulation of arbitrary objects.

In contrast to robots, humans can manipulate arbitrary objects effortlessly, as long as cutaneous sensations are present [4]. Every time we grasp a glass of water or a pen on a table, a complex sensorimotor dance is being unconsciously operated by our nervous system. The object is identified and located, the arm extends to reach, and, at the very instant of contact, a complex ensemble of neural impulses coming from mechanoreceptors embedded in our skin informs the brain about the shape, presence of edges, and nature of surface [14]. Within a tenth of a second, motor commands are modulated to accommodate the orientation of edge [135] or the presence of a slippery surface [74]. During grasping, the nervous system regulates grip forces so that it creates a friction force slightly larger than the load on the object, providing a safety margin of about 10% of the maximum permissible friction force, to be robust to unexpected perturbations.

Robotic grasping algorithms, on the other hand, regulate grip forces by either relying on prior knowledge of the frictional behavior [13] or formulating assumptions about the coefficient of friction [161]. Because the knowledge of the coefficient of friction is necessary to find the optimal grasping force that balances the load on the object coming from gravity, inertial force, or external perturbations, with the friction force applied by the fingertips. However, to be robust to the potential uncertainties of its estimation, the value of the coefficient of friction is often assumed to be lower than its actual value. This underestimation leads to a grip force larger than the optimal force. While this assumption of low initial friction ensures a robust grasping behavior, it may cause damage to the fragile objects, or leads to loss of mobility as the object cannot rotate around the contact point during force closure tasks. More dramatically, in the few cases where the object is more slippery than anticipated, the absence of the real-time estimation of the frictional state leads to a failure to grasp and lift. Sensing the coefficient of friction early in a grasp-and-lift task is therefore crucial for controlling robotic hands, especially during the interaction with fragile or slippery objects.

Several groups have recognized the intrinsic need for precise and timely measurements of the frictional state during grasping and manipulation and suggested original approaches for estimating the frictional state from tactile sensors. For instance, gross slip between the sensor and the object surface is straightforwardly detected using the transient tactile signal change when the stick-to-slip transition happens [25], by measuring micro-vibrations of the sensor induced by gross slip [45, 170], or by observing sudden displacements of the markers on a membrane [73].

However, to keep the object stable in hand and prevent falls, gross slippage should be avoided. As a consequence, the previous methods based on detecting gross slippage of the object are triggering adjustments too late. To gain warning signs of incipient slippage, several methods rely on detecting the fast transition from stick-to-slip by measuring the evolution of the characteristic pattern of deformation inside the area of contact on a spherical fingertip. This pattern evolves with the progression of the slippage, the outer edge of the contact is first to slip while the center remains stuck. Progressively, the stuck area disappeared, leading to a full slip.

The incipient slippage can be detected using a membrane covered with hemispherical nibs. When the edge of the contact breaks free, the nibs near the periphery vibrate and create a transient signal that can be recorded by an accelerometer embedded in the elastic body [176]. The incipient slippage can also be estimated from fitting an ellipse to the optic flow image of the contact area and measuring its eccentricity [66]. Other methods detect the increase of shear strain in an elastic membrane at the edge of the contact area [120, 19], or compare the lateral shift of the markers near the periphery of the contact area [68]. Lastly, the inhomogeneity of the displacement field, measured by its entropy, can provide a powerful metric of partial slippage [204]. By detecting incipient slippage, the controller is able to adjust the grip force earlier before the total slippage, greatly improving the robustness of grasping tasks.

However, the regulation grasping force based on the detection of the incipient slip can occur too late. In cases where the dynamic coefficient of friction is smaller than the static coefficient of friction, the stuck region can disappear catastrophically, leading to the sudden slippage of the object if the grip forces are not adjusted quickly enough [173]. The regulation of grip force in humans makes use of the incipient slip for reacting to external perturbations, but one other cue is likely to inform about the slipperiness of a surface from the moment when the finger comes into contact with the surface. It has been shown that, when voluntary lifting an object, participants regulated their grip force with a similar safety margin to slippage that was independent of the coefficient of friction of the surface [74, 17]. The grip forces are increased for slippery surfaces such as velvet but smaller for surfaces with more adherence, such as sandpaper or glass. A surprising finding of this research is that the adjustment of grip force begins within 100 ms of the contact being made, preceding the appearance of the tangential load. The regulation is illustrated in Fig.5.1a. The variation of rate of increase of grip force at initial contact indicates that humans use early estimates of friction by applying a simple normal pressure onto the object to adjust their initial grip force. One of the hypotheses put forward is that the friction of the surface is encoded in the magnitude of the lateral strain of the skin when the finger is pressed onto the surface. High friction surfaces limit the lateral mobility of the skin during the contact, and therefore the total amount of lateral strain of the skin is lower for surfaces with a lower coefficient of friction [75].

Few years before the hypothesis of a lateral strain pattern emerged in the neuroscience community, roboticists have developed sensors to measure the coefficient of friction between the two surfaces by applying only normal pressure. First Shinoda et al. then Maeno et al. demonstrated that the gradient of the shear strain at the center of an elastic body under normal pressure is a function of the value of the coefficient of friction between the two contact surfaces. [120, 166].

Despite promising results, the early estimate of friction in the robotic control still remains a curiosity. Chen et al. proposed an eight-legs sensor to estimate the coefficient of friction by a simple press. Despite its simple principle of measurement, the sensor is only able to estimate the range of coefficient of friction [24, 134]. But more importantly, because the number of elements is low, it cannot resolve fine details of the haptic scene such as the presence of edges, corners, and the spatial variation of elasticity, which also contribute to the regulation of grip.

To overcome this limitation, we present a method for sensing the distribution of coefficient of friction within the area of contact, mapping the resistance to motion onto observable surface features before any lateral motion is observed, while retaining the ability to capture a dense representation of the tactile scene. The ChromaTouch is a camera-based tactile sensor that uses 441 distributed markers, each of which measures the local 3d deformation of an elastic membrane. Using convolutional neural networks, we are able to estimate the deformation of the membrane under the indentation of various objects and reconstruct their shape as well as the distribution of the coefficient of friction. This dense reconstruction required only 1.5 mm of normal indentation with the object. The estimation of the local shape and friction coefficient could directly be used for re-positioning the contact between the fingers and the object for optimal grip (i.e. making use of edges and high friction area). The early knowledge of the amount of adherence that the surface also provides information to design feedforward regulation of grasp force.

## 5.2 Perception architecture

The objective of this work is to develop sensing and processing method able to tactually extract:

- the global curvature at the location of the contact
- the shape of small features within the contact region
- local distribution of friction

In our previous work, we demonstrated a tactile sensor which used color-mixing of an array of marker to capture the 3d deformation field and to use the information embedded in this vector field to measure the global curvature [106, 107]. However, the markers of these two previous sensors measures 2 mm in length or in diameter, which shows inaccuracy in measuring small features of the objects. A higher spatial resolution could improve the sensing ability for small geometry changes on the object, so allows a more precise measurement of the object shape.

### 5.2.1 Dense deformation sensing

The tactile sensor used to estimate the distribution friction derives from our previous implementations of the color-mixing principle [106, 107]. The number of markers is increased to 21 by 21, which offers 4.5 times more resolution than previous devices. The experimental apparatus alongside an illustration of the inner-working are shown in Fig.5.1b. For each marker, the camera sees the transparent yellow markers on the top layer. The opaque magenta markers placed closer to the surface partially overlap the yellow marker on the image. Where this overlap occurs, the color seen by the camera appears red, resulting from the combination of yellow and magenta. Applied forces on the surface of the sensor shift and stretch the magenta markers, which leads to an apparent change in size and of color content of the image of the markers. The pattern made by markers is unique to the 3-dimensional displacement of the magenta marker, which is itself affected by the stimulation on the surface. A

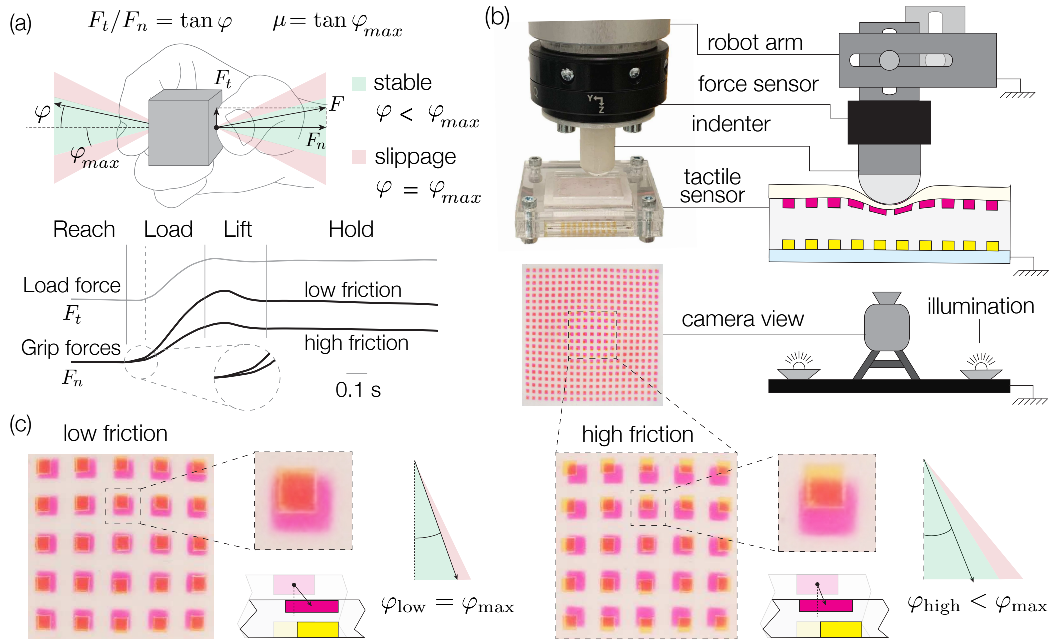


FIGURE 5.1: (a) Grip regulation in humans involves reacts to various frictional conditions at the instant of contact, even before a lateral force is observable. Larger grip forces are engaged for slippery objects. Adapted from [75]. (b) Experimental apparatus and sensor used for estimating the frictional interaction at initial contact. The indenter presses against the elastic membrane of the sensor, fixed on a rigid base. The stretch and motion of magenta markers relative to the yellow marker were captured by a camera. (c) When in contact with high friction surfaces, the lateral motion of the marker is smaller than when in contact with low friction surfaces, for which local slippage appears. The sensor uses this effect to estimate the frictional state during initial contact.

calibration of the marker's change of shape and color allows the estimation of friction between the contact and the 3d deformation of the sensor.

### 5.2.2 Apparatus for dataset creation

The dataset used for calibrating the sensor, estimating topographical features of the object and the friction between the contact surfaces was obtained using the apparatus shown in Fig.5.1b. The sensor was clamped on its edges between transparent acrylic plates and supported on the bottom. LEDs mounted under the acrylic support provided diffuse illumination limiting the shadows and influence of external light sources. A high-resolution camera (A7Rii, Sony Corporation) set at 24-mm focal length, with manual focus and manual white balance, captured images of the marker array. During the experiments, 3-dimensional displacements were applied by a 3d printed indenter or glass lenses mounted on the end effector of an industrial robot

(UR5, Universal Robots). The force sensor (FT300, Robotiq), mounted on the end effector of the robot, measured applied forces. A sliding procedure after the initial contact provided ground truth of coefficient of friction.

### 5.2.3 Shape perception

The pattern formed by the markers directly informs about the topography of the surface. When the object is pressed, the surface of the sensor deforms, stretching and moving the soft magenta markers. The pixel shift of each marker on the sensing image is directly linked to its relative lateral displacement. In addition, the observed size of the magenta marker increases under normal pressure. This change of size might not induce pixel-sized motion, but it does induce a visible change in color when combined with the overlaid marker patch. The change of color provides a direct measure of the normal displacement of each marker. Once the lateral and normal displacements are known, the local shape of the object can be recovered by bi-linear interpolation of the normal displacements, to consider the lateral movement of each marker.

### 5.2.4 Estimation of local friction

The friction of the surface has a dramatic effect on how much the marker is stretched for a given force. A high friction surface restricts the deformation of the surface, and consequently, markers experience only little stretches. However, when the sensor is in contact with a convex and slippery object, the markers laterally stretch due to the Poisson effect, the phenomenon by which a material tends to expand in directions perpendicular to the direction of compression. The same behavior can be seen on the entire contact with larger lateral displacement of the magenta marker for the low friction case due to local sliding. Friction produces a pattern of deformation that is markedly different under different frictional conditions, even if the normal pressure distribution is the same. The images in Fig.5.1c illustrate the effect of friction of the object on the stretch and shift of the marker.

Therefore, the friction between the indenter and the tactile sensor can be estimated by observation of the behavior of the marker. To estimate friction, we trained a convolutional neural network to derive an estimate from the tactile images captured by the camera of the sensor. This network takes into account the size and spatial distribution of the markers to derive a friction estimation.

## 5.3 Data-driven shape estimation

Previously we estimated the displacement field of the marker from the change of hue which is correlated to the normal displacement, and we used center tracking of the marker to retrieve their lateral displacement. While the lateral displacement was directly proportional to the actual deformation at the surface, the estimation of the normal displacement at the surface required a complex non-linear model. This model also shows a dependency on friction and softness of the indenter and tends to underestimate the normal displacement for high friction surfaces.

To remedy these limitations and improve the estimation of the normal displacement, instead of calibrating the sensor from a single marker as what has been done before, a convolutional neural network (CNN) was employed to calibrate the relationship between marker shape and color and its normal displacement. To train the network, it was fed with real images of the markers as input and simulated deformation found with finite element models.

### 5.3.1 Training and testing datasets

The convolutional neural network model for shape estimation was trained using supervised learning. To build the dataset that links the images seen by the sensor to the deformation of the surface, we used real measurements made with the apparatus and compared them to the displacement simulated with a finite-element model, shown in Fig. 5.2a. Four rigid hemispherical indenters with radius $r = \{10\text{ mm}, 15\text{ mm}, 20\text{ mm}, 25\text{ mm}\}$ were used to press the sensor in both the real and the virtual environments. Each indenter was lowered at the center of the sensor with a step size of 0.5 mm during a total displacement of 2.5 mm on the $z$ axis.

**Finite-element simulation:** The simulation was achieved using COMSOL by a model of the sensor comprising a rubber of Young's modulus of 0.5 MPa which matched the Young's modulus of the material used in the real sensor. The boundary conditions were also set to mimic its real counterpart, where all edges and faces were set to be fixed (i.e. displacements are null), except for the top surface which was left free (i.e. forces are null). An array of 21 by 21 marker points spaced with 1 mm distance was set at 0.5 mm depth from the top sensing surface. Interaction with two coefficients of friction $\mu = 0.4$ and $\mu = 0.1$ at the contact surface was simulated, matching the experimental conditions. The simulator is able to model the distributed 3D contact forces and the deformation of the sensor for each indentation test.

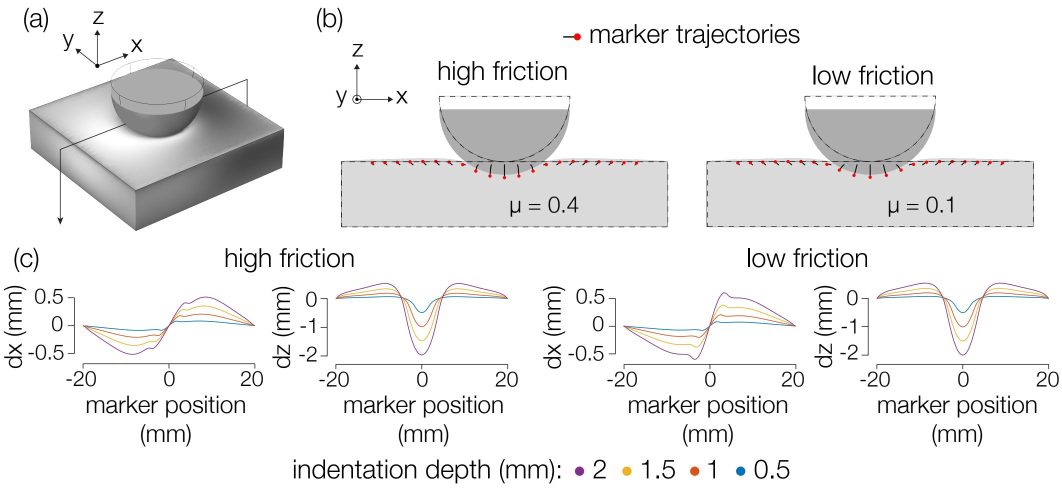


FIGURE 5.2: Comsol simulation of a indenter of 20 mm in diameter pressing on the sensor with an indentation depth of 2.5mm. Red dots shows the displacement of the markers under different frictional conditions. Under low friction, the lateral displacement of the marker is slightly larger.

Fig. 5.2b shows the middle cross-section of the sensor under 2 mm normal indentation applied by a hemispherical indenter of 10 mm in radius. Differences on the displacement vectors caused by different friction can be observed in the figure. Fig.5.2 shows the lateral and normal displacement field of the cross-section for different indentation depth. The lateral shift of the marker around the contact region is larger for high friction surfaces than for slippery surfaces. The simulation is consistent with the previous remark that high friction surfaces limit the lateral shift of the marker.

**Experimental measurements:** Input images from the real experiments were collected when the sensor was pressed with spherical indenters at the center of the sensing surface. To be consistent across the real and virtual environments, the size of the indenters, made from glass lenses, and their indentation depths were matched to the one of the simulations. To obtained a low friction condition of $\mu \approx 0.1$, we applied oil onto the surface of the indenter. The high friction ($\mu \approx 0.4$) condition is achieved by directly press the indenter onto the sensor after the glass was degreased. During each of the trials, a camera captured the shift and stretch of the markers. For each different contact condition, the robot pressed along the normal of the surface with a speed of 10cm/s followed by a 5-second relaxation period. The isometric procedure was repeated 8 times to collect enough data for the training and estimate the variability to uncontrolled factors. The images fed to the network consists of the image of the sensor under load to which the unloaded image was subtracted.

### 5.3.2 Calibration to recover displacement fields

To calibrate the sensor, conventional marker tracking method was used to extract the lateral deformation of the sensor. But for normal deformation, a CNN model was trained to convert the sensing image to marker displacements. To train the network and derive a measurement of normal displacement field which is invariant to the local coefficient of friction, we partitioned initial images into numerous smaller subimages. To this end, the raw images with 441 markers were cut into 289 subimages of 3-by-3 markers with a size of 85×85 pixels for each subimage. The coefficient of friction strongly influences how the magenta layer is stretched and therefore, the hue value of a single marker can be different even under the same normal pressure. Using the 8 neighboring markers, the accuracy of the regression greatly increased. The underlying reason is that the surface of the sensor is a continuum medium, and a localized stimulation diffused throughout the body, therefore, markers away from the contact are affected. More importantly, the subimages contain redundant information about friction which affects the stretch of the central marker but also with the inter-marker spacing. Therefore training the network with these subimages allow for providing the deformation data, while negating the influence of the frictional contact.

Fig. 5.3a demonstrates how the training dataset was constructed. Illustration of the construction of the subimages is shown in Fig. 5.3b and is match with the simulated normal displacement value illustrated in Fig. 5.3c.

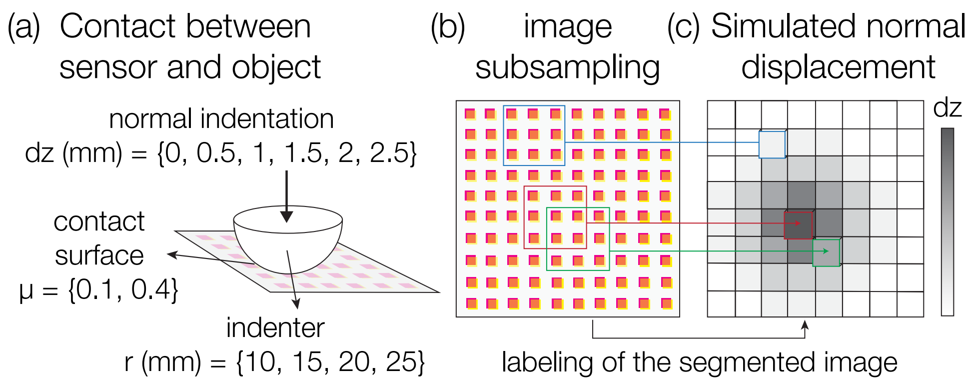


FIGURE 5.3: (a) Experimental and simulated conditions used to produced the input training dataset from real images and virtual displacement vectors. (b) Subimage creation uses 8 adjacent markers to each marker. (c) Displacement labels simulated via finite-element method. (b) and (c) show how the experimental images were labeled with the simulated results

The structure of the convolutional neural network used for calibrating the observed image of the sensor to the displacement of its surface, is shown in

Fig. 5.4. 384 tactile images, for a total of 110976 subimages, were captured in the experiments for training the CNN model. 80% of the images were used to train the network, 10% for validating the results during the training, and 10% for testing the accuracy after convergence. The network was trained with a fit goodness of $R^2 = 99.2\%$ for training and $R^2 = 98.4\%$ for testing.

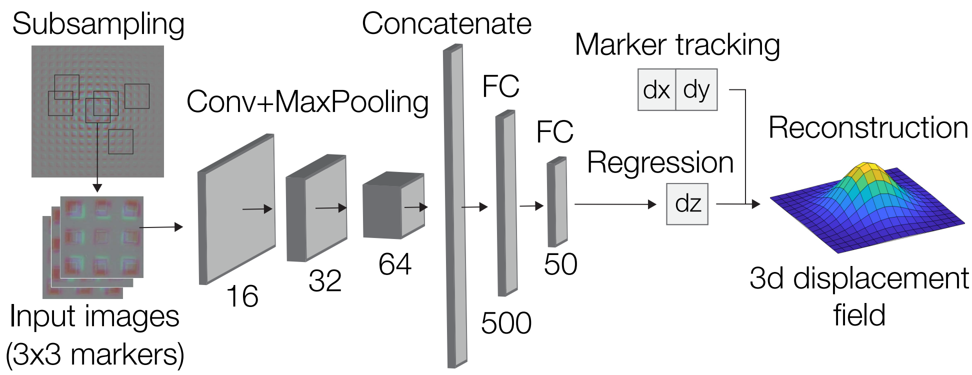


FIGURE 5.4: Structure of the CNN for estimation of the normal displacement field. The input images were subsampled from the tactile images captured by the camera and then trained by 3 convolution layers followed by 2 fully connected layers. A regression layer was used to output the normal displacement.

### 5.3.3 Friction-invariant shape estimation

The results of the estimation were put to the test using two indenters not seen before by the network during training: a flame-shaped indenter and a barrel-shaped indenter. To reconstruct the 3d displacement map, images of the sensor under pressure were captured and subsampled in order to be sent as input images into the network obtained in the previous section. The network outputs the normal displacement of the marker located in the center of each 3-by-3 markers array subimage. The lateral displacement of the marker in the middle of each subimage was obtained by marker tracking. The 3d displacement vector related to each subimage was formed by the normal displacement predicted by CNN and the lateral displacement of the marker in the middle of that subimage. Then the 3d displacement field was reconstructed by rearranging the displacement vector into the original 21 by 21 markers array. The whole displacement estimation procedure is shown with the convolutional neural network structure in Fig.5.4.

The results of 3d displacement field estimation for the two indenters are shown in Fig.5.5a. Results on normal displacement for both indenters show that estimation of normal displacement using the convolutional neural network shows much less noise and better accuracy comparing with estimation using the hue value of a single marker.

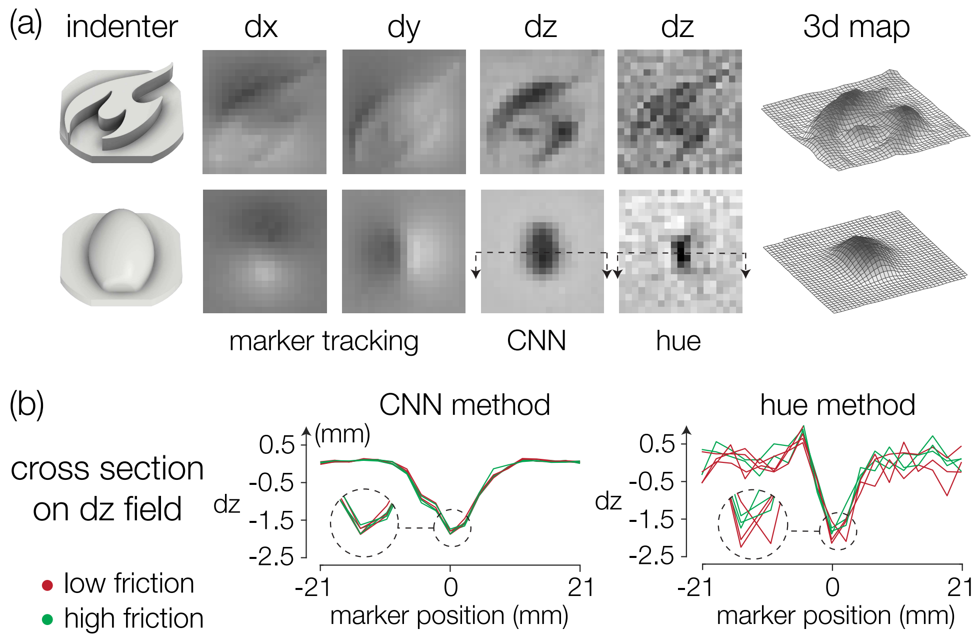


FIGURE 5.5: (a) Estimation of the displacement field and the 3d reconstruction map when pressing a barrel-shaped object and a flame-shaped object onto the sensor. (b) Comparison of the normal displacement field estimated by the convolutional neural network and by the hue changes, in the high and low friction conditions.

We compared the convolutional neural network to the previously used hue method on the barrel-shaped indenter. The results can be observed in figure Fig. 5.5b. The object was pressed at the center of the sensor with an indentation depth of 2 mm. Two frictional conditions were tested with coefficient of friction $\mu = 0.1$ and $\mu = 0.4$. Each test was repeated 3 times, and the normal displacement field was estimated using both network prediction and hue change. With the hue method, the displacement with high friction shows underestimations for all the three repetition tests, while the displacement field estimated by the CNN is invariant to the coefficient of friction, which demonstrated the power of the convolutional neural network using 3-by-3 to solve the underestimation problem which regular calibration from the simple variation of hue suffered from.

### 5.3.4 Effect of friction on the displacement field

To test the generalization of the calibration to different frictional conditions, we experimented with estimating the deformation pattern on a barrel-shaped object with a mixed friction pattern. We coated half of the part with oil to create an object where one side was slippery while the other maintains a high level of frictional resistance. The image of the marker deformation was measured upon pressing the barrel-shaped object on the sensor with an indentation depth of 2mm. The results of the estimation of three frictional conditions, *high* and *low friction* and *mixed friction* is shown in Fig. 5.6a. The three conditions corresponded to the indenter degreased, fully coated with oil, and for which oil was applied on only half the surface. Fig. 5.6b shows the estimated displacement field on x-axis for the split case. Fig. 5.6c plotted the lateral displacement at the middle cross-section obtained from all the three frictional conditions. The lateral displacement with the split coefficient of friction shown in the dotted blue line coincides with the displacement for the high-friction side on the left side of the figure, and with the displacement for low friction side on the right side of the figure. This observation on lateral displacement field demonstrated the capability of the sensor to correctly recover the 3-dimensional deformation of each marker even in the presence of arbitrary frictional pattern.

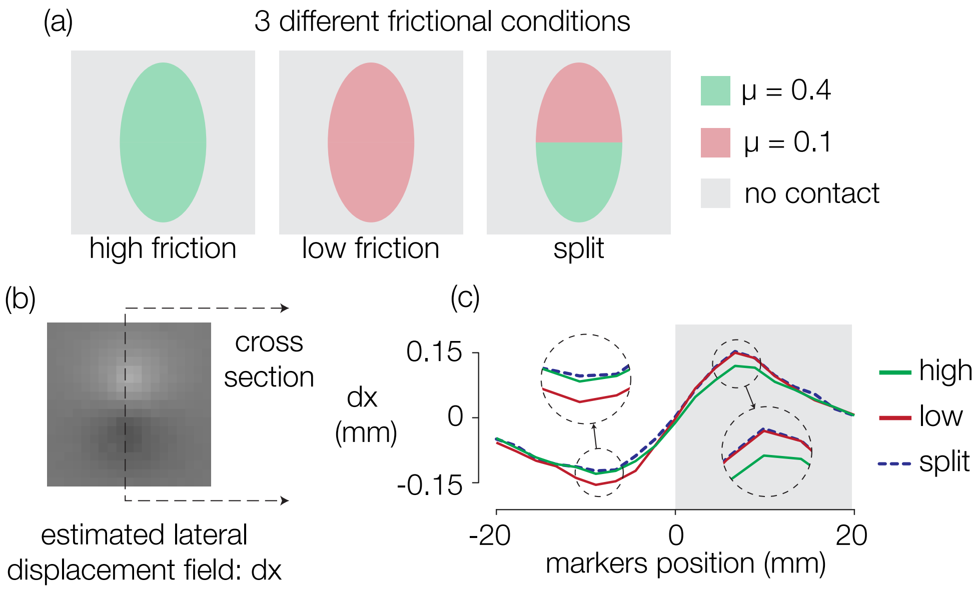


FIGURE 5.6: (a). The generalization of the calibration network to friction was tested on three different frictional conditions. (b) The cross-section shows the lateral displacement of the markers on the main vertical axis. (c) The green, red and blue lines show the displacement for the *high*, *low*, and *mixed friction*. Note that the blue line coincided with the green line on the high friction side and with the red line on the low friction side, demonstrating the discriminability of the approach.

## 5.4 Learning to estimate friction

The second set of experiments is design to take advantage of the friction-dependent behavior of each marker to derive an estimation of the distribution of the coefficient of friction throughout the contact surface. When the sensor is pressed on an object, the markers deform, and the pattern of deformation is affected by the local frictional constrained. High friction surfaces impose a non-slip condition of the surface of the sensor, limiting the lateral displacement of the embedded markers and conversely, when the surface of the object has low friction, the surface of the sensor is free to move laterally and markers shift toward the outside of the contact. The approach lay down in this section reverses the relationship by extrapolating from the lateral displacement and deformation of the markers an estimate of the local coefficient of friction using another convolutional neural network.

Figure 5.7 shows the displacement map on x, y, and z directions resulted from the simulation and the displacement estimation. The sensor was pressed by an indenter of 10 mm in radius at 2 mm indentation depth. The images on the top were captured with $\mu = 0.4$, and the images below were with $\mu = 0.1$. The middle cross-section of the displacement field on x-axis shows that, when the friction between the sensor and the indenter is low, the lateral displacement of the marker is obviously larger than high friction. Therefore, the pattern of the markers under pressure captured by the camera indicates the friction of the contact surface, which was used to build the CNN model for friction estimation.

### 5.4.1 Training dataset

For collecting the training dataset for friction estimation, the same sensor images used for training the network for shape estimation were used. To add the diversity of the dataset, the sensor was pressed by a flat square indenter with 20 mm in length, and a cylinder indenter with a radius of 10 mm. These two new indenters promote the sensitivity to edges and sharp corners not seen in the spherical indenter. Similar to the collection of the rest of the dataset, these two indenters were lowered with a total indentation depth of 2.5 mm in 0.5 mm step size at the center of the sensor. Two coefficient of friction $\mu = 0.4$ and $\mu = 0.1$ were applied using oil. Each test was repeated 8 times to provide redundancy. These additional experiments added 96 new images or 27,744 subimages into the training dataset.

To collect the output labels for the training dataset, we incorporated the displacement estimation. All the input images for friction estimation were

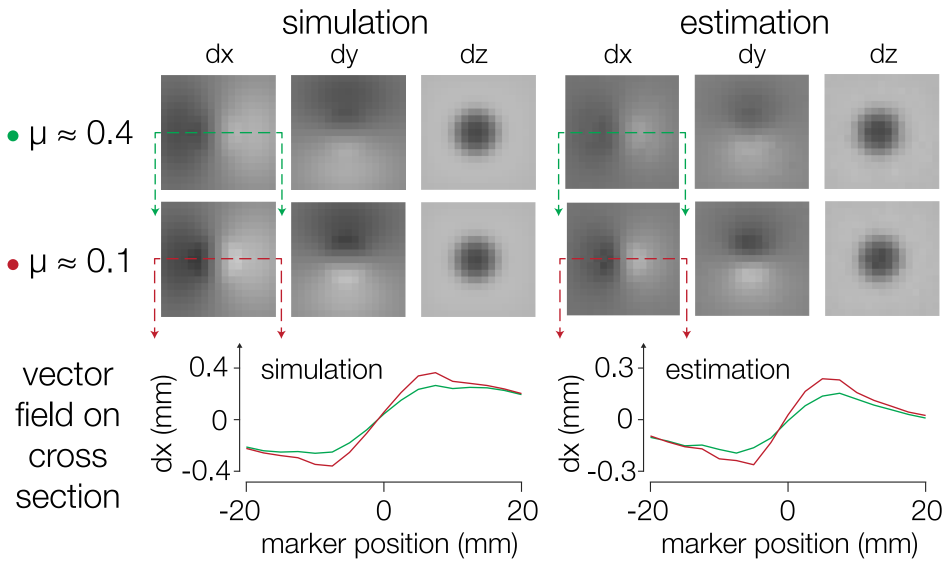


FIGURE 5.7: Displacement field for a spherical object pressing on the sensor. The lateral displacement field along the cross-section highlights the difference for different frictional conditions. High contact friction limits the lateral motion of the marker, resulting in small lateral displacement magnitudes of the marker.

first sent to the first network to estimate the displacement and to reconstruct a 3d displacement map of each image. Then, for each estimated displacement map, the regions where the normal displacement of the marker smaller than 0.1 mm were labeled as *no contact*. The reminder areas are labeled as $\mu = 0.4$, or $\mu = 0.1$, depending on the coefficient of friction applied for each indentation test. For the training dataset, the labels at the contact region were either $\mu = 0.4$ in the case where the object was degreased or $\mu = 0.1$ when oil was applied on the entire indenter surface.

### 5.4.2 Convolutional neural network for friction estimation

Before training, the raw images captured by the camera were cropped into subimages containing a 5-by-5 markers array with a size of 145×145 pixels for each subimage. The subimages were used as training input, and the corresponding local coefficient of friction on each marker was used as output data for labeling the training images. Fig. 5.8a shows the contact conditions contained in the training data, Fig. 5.8b illustrates the image crop of raw images and Fig. 5.8c shows the output labels.

The network used to estimate friction contains 3 convolution layers, a concatenate layer, followed by 2 fully-connected layers. The outputs of coefficient of friction are classified into 3 categories: $\mu = 0.4$, $\mu = 0.1$ and *no contact*,

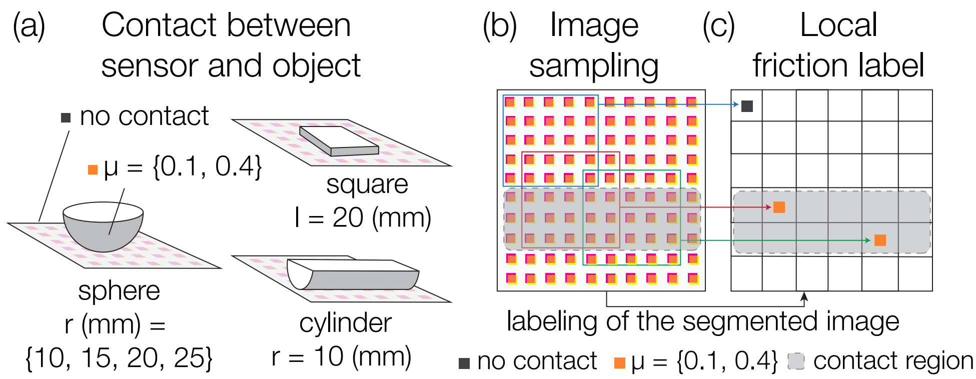


FIGURE 5.8: (a) Contact conditions and indenters used for experiments and simulations for collecting the input training images and the local friction labels. (b) Image partitioning into 5-by-5 markers subimages. (c) Illustration of the local friction labels. The *no contact* area was threshold from the displacement map. The friction labels in the area under contact were set by the coefficient of friction applied during the experiments. (b) and (c) shows how the experimental images were labeled with the simulated results

using a Softmax layer. The solver for the training network is a stochastic gradient descent with momentum (SGDM) optimizer. The validation accuracy and loss were calculated with a frequency of 30 iterations per epoch to find the optimal weights for the convolutional filters. The training has 10 epochs, and the data was shuffled after each epoch. 480 raw images in total were captured and segmented, leading to 138720 input images, among which 80% were used for training the weight and biases, 10% for validating and refining the training, and 10% for testing the trained network. The validation and the testing results reach an accuracy of 92.5% and 91.2%, respectively.

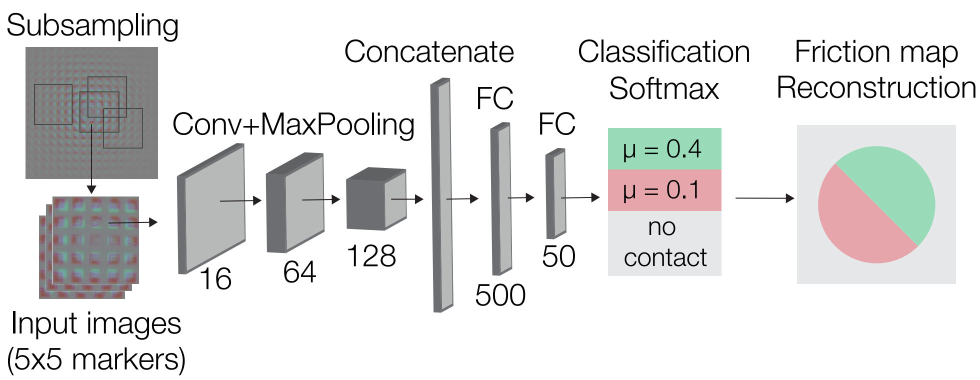


FIGURE 5.9: Structure of the convolutional neural network for friction estimation. The outputs are classified to *high friction*, *low friction*, and *no contact* using a Softmax layer.

### 5.4.3 Generalization of the estimation of friction

The procedure for estimating friction from an arbitrary sensor image is illustrated in Fig. 5.10. The images captured by the camera are partitioned into subimages, which contain 5-by-5 markers arrays. The subimages were used as input of the trained network. With these input images, the desired estimated friction map should be half with high friction and half with low friction, and is projected back to the grid map.

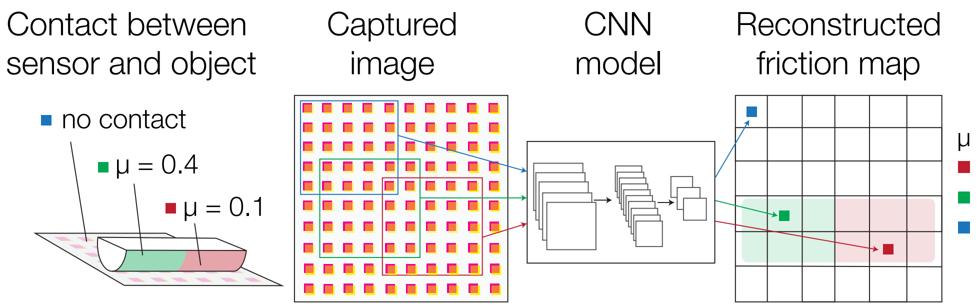


FIGURE 5.10: Procedure for the estimation of the coefficient of friction. The object with the split frictional condition (half surface applied with oil) was pressed against the sensor. The obtained tactile images were subsampled to 5-by-5 markers array and sent to the CNN model to output the local friction classified by: no contact, $\mu = 0.4$ and $\mu = 0.1$. The output values were then rearranged to form the friction map.

While the training dataset involved a spherical object, a cylindrical object, and a flat square object, the network can generalize its estimation of the frictional resistance to other shapes. To illustrate the generalization capabilities, five objects shown in Fig. 5.11a were pressed against the sensor with an indentation depth of 2 mm. These objects were 3d printed in polylactide (S3, Ultimaker) and coated with oil on their right side only. The results of the estimation of friction are presented in Fig. 5.11b. Overall the network correctly predicts that the coefficient of friction is high ($\mu \approx 0.4$) on the left part and smaller ($\mu \approx 0.1$) on the right part, regardless of the shape of the object. The shape itself however is not correctly interpreted, showing the limitation of the network. The prediction result shows a mean accuracy of 76.1% for all the indenters tested in this experiment.

Additionally, we compared the estimation of the cross shaped indenter with uniform low and high friction. The result are shown in Fig.5.11c. In the uniformly high friction case, where the indenter is degreased, the prediction is correct for the most part but fails on the edge of the object probably because of local slippage. On the other end, the uniform low-friction condition is correctly predicted as the friction coefficient equals to 0.1 over the

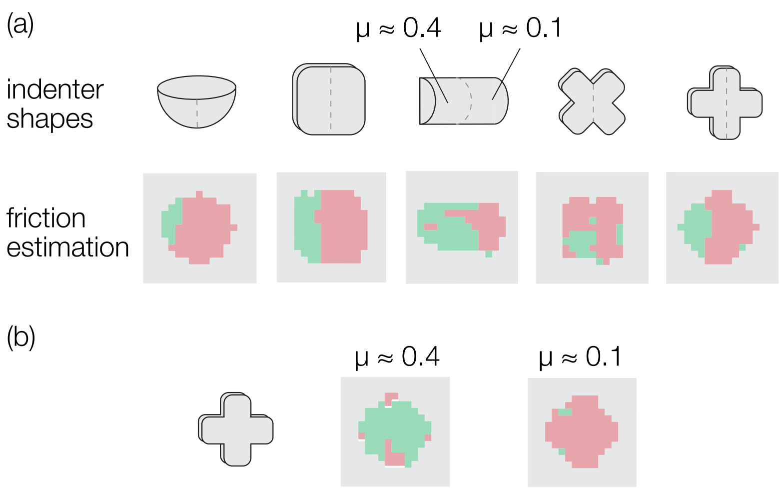


FIGURE 5.11: Friction estimation results when pressing different objects onto the sensor. Yellow pixel shows the region with high friction, light blue shows the region with low friction, and dark blue means regions with no contact. The friction estimation method allows the detection of two frictional states on the same surface for different object shapes. (a) Mixed friction distribution. (b) Uniformly distributed friction.

entire contact area. The difference between the two conditions might result in a bias towards low friction estimation built in the network. Nonetheless, the results demonstrated that the sensor is able to estimate the coefficient of friction on different objects via a simple press. More importantly, the sensor can distinguish different friction value when the coefficient of friction on the contact surface is not uniform.

## 5.5 Discussion

Tactile sensing in robotics has been mainly concerned with detecting contact events. Recently, its true potential as a source of information about the state of slippage and robust shape detection has been exploited[73, 170, 39, 204, 79, 46]. Building upon previous work, we introduce a new method that uses convolutional neural networks to estimate the distribution of friction and the 3-dimensional deformation field that the sensors experience when pressed with an arbitrary object. While the shape reconstruction depends on a relatively small number of sensing elements and is not as precise as solutions using retrographic sensing [79], it provides a unique look on the state of frictional resistance that the skin experiences as well as sufficiently well-defined corner and edges that are essential for estimating the pose of the object in hand. To illustrate this unique capability, the friction estimation and displacement field are merged in Fig. 5.12, where the color represents the local coefficient of friction. The high friction region, shown in green, provides an optimal location for grasping the object stably without recruiting large grip forces.

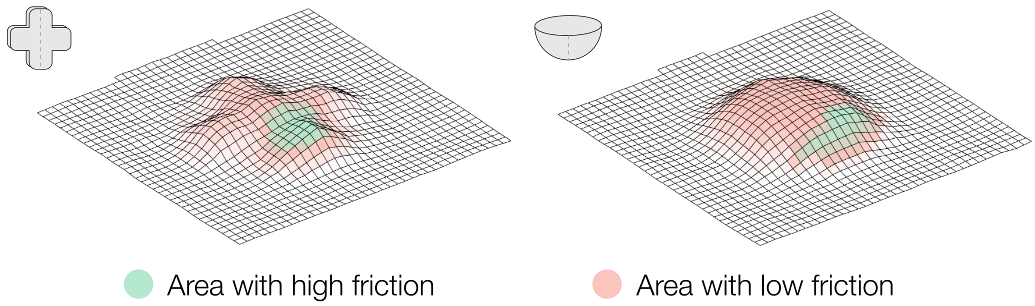


FIGURE 5.12: Merged displacement field and friction map.

To the best of our knowledge, this is the first demonstration of the ability to measure the distribution of friction only with a single contact, which helps locate the area of high friction and could inform new grasping strategies. Previous works have shown estimation of friction on a spherical contact [165, 120], but could not resolve differences in adherence inside the contact area. By estimation not only the global adherence of the contact, but also a map, a gradient of friction can be computed to help predict the direction of slippage and potential area where the skin might detach first. Human grasping behavior takes advantage of the knowledge of friction to maximize the stability while minimizing the grip force, for example, when grasping a pen on the rubbery part, or holding a half soaked soap bar on the dry side. Taking inspiration from these behaviors, the estimation of friction distribution may potentially help to guide the motion of robots towards an optimal grasping location in order to ensure a more stable manipulation.

The sensor used in this work has 441 sensing markers, which improves the spatial resolution from the 100 and 77 markers sensors we used in previous works in [106, 107]. This resolution improvement increased the ability to estimate the displacement field and the shape and feature of small objects. This is particularly important to find edges and corners which could be used to secure grasping and locate objects. However, small details of the complex shape, such as the flame, are not well resolved. Increasing the density of marker and increasing the training data on various objects could improve the shape perception. In addition, today the friction map possesses a crude quantization, and can only resolve two level of adherence. Maeno et al. [120] reported detecting about 5 levels of friction, using the entire contact area.

Building on this, larger subimages with more resolved deformation could potentially increase the quantization of the friction. To achieve a finer accuracy, a new training dataset containing various levels of friction needs to be created.

One common criticism of machine-learning methods is their lack of transparency of the way they reach certain results. This work is no exception. While we are confident that the pattern of the markers is used to estimate deformation and friction, the way the network operates to reach a conclusion is still largely unknown. Future work will use tools from the field of explainable artificial intelligence to further the understanding of the inner working of the networks.

This work investigates the development of friction during the initial contact. However, slippage and shear forces are not yet captured. Several works have shown that the lateral displacement of the markers on an elastic membrane can be used to detect incipient and full slippage [73, 39]. Such approaches can straightforwardly be implemented alongside the current work. At the moment, the method measure what we call the *frictional capacity*, representing the amount of shear traction that a single element can support. Future works will endeavor to quantify how much of this capacity is currently being used.

## 5.6 Conclusion

Inspired from the early grip adjustments in humans during lifting tasks [74], we proposed a method to estimate of the frictional state between the object and the sensor at first contact via a simple press. This method uses a bespoke tactile sensor that employs an embedded camera to capture a dense picture of the 3-dimensional deformation of an elastic body.

We improved the sensing design by increasing sensor spatial resolution with 441 arranged markers, which is around 4.5 times more than the first version. This improvement allowed us to train a convolutional neural network to calibrate the estimation of the normal displacement and lateral displacement and subsequently recover the shape of the object. Comparing with the first version using a direct change of hue, the proposed convolutional neural network eliminated the influence of friction on normal displacement estimation. This method produces a tactile image with less noise and better accuracy with $R^2 = 99.1$ for training and $R^2 = 98.4$ for testing. The 3-dimensional shape of the object could be reconstructed using the trained network.

We also trained another convolutional neural network to estimate the frictional condition upon the initial contact with the object. To detect the area of low and high friction, partitioned markers array were used as input images. With the proposed algorithm, the sensor is able to estimate the frictional state at first contact via a simple normal pressure with an accuracy of 76.1%. This early estimation of friction would allow the robot to adjust the grip force at the earlier state of grasping, even before any shear forces or slippage occurs. This improvement is likely to be paramount for enabling stable and robust manipulation. Moreover, the sensor is able to distinguish different frictional conditions at the same contact surface, which can further help the robot to choose the optimal grasping location to prevent slippage. Future work aims at the implementation of the sensor on a robotic hand to provide tactile feedback for robotic manipulation control.

# Supplementary Material

## Sensor fabrication

The manufacturing process is built upon previous works. First, the base is molded from a transparent elastomer (SortaClear 12, Smooth-On, Macungie, PA, USA) in a high-resolution 3d-printed mold (PLA, Ultimaker, Geldermalsen, Netherlands). The grooves left by the cast are filled with the magenta markers, made from the same elastomer in which a dye is added. Then a protective layer is molded, on top of which the yellow filter is placed. The yellow elements are laser cut, and the rest of the film discarded. A protective transparent layer embeds the yellow transparent marker. The whole operation takes approximately 2 days, including the curing time.

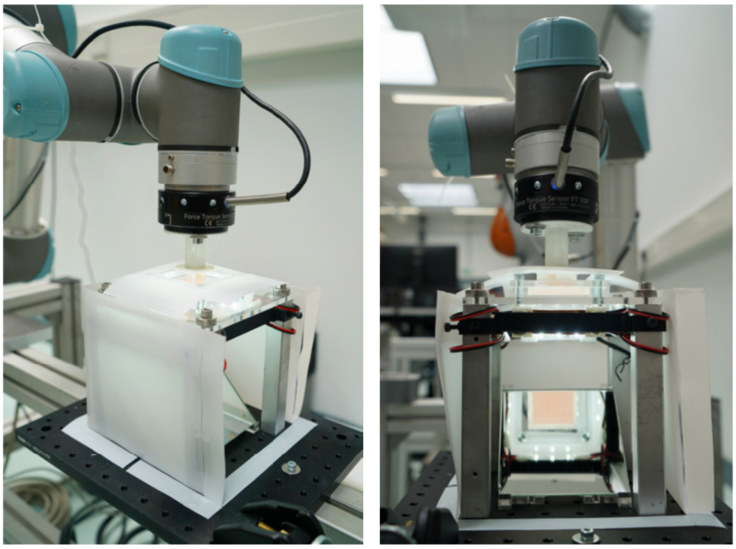

FIGURE 5.13: Experimental set-up. The sensor is fixed on a rigid base and illuminated with LED lights. The 3d printed indenter is mounted onto the robot to press the sensor. The sensing image is reflected by a mirror installing under the sensor at 45 degree. The reflected image was captured by a Sony a7Rii camera for post-processing.

## Measurement of ground-truth coefficient of friction

To find the actual value of the coefficient of friction, we used the robotic arm as a tribometer by sliding the end effector across the surface and measuring the normal and tangential forces. The coefficient of friction between the sensor and the indenter are calculated by the ratio of applied lateral force to normal force measured by the force sensor while sliding the indenter onto the sensor. Each test was repeated 5 times with 3 different indentation depth as shown in figure 5.14 to calculate the average value of the coefficient of friction. The coefficient of friction is found to be approximately 0.1 and 0.4 for the surface with oil and without oil, respectively.

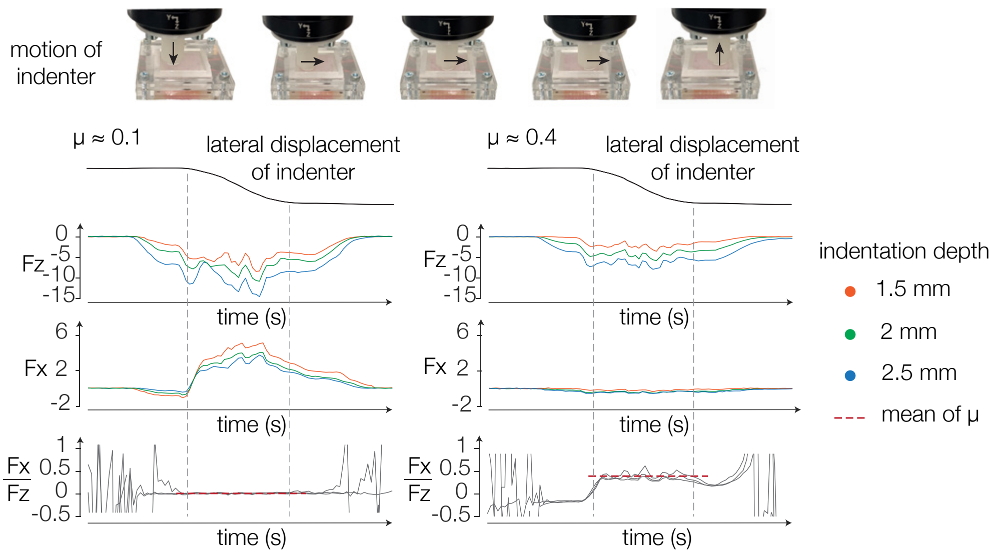


FIGURE 5.14: Images and time series of the sliding procedure to gather the ground truth value of the coefficient of friction.

## Image processing

The image processing was performed by Matlab. The top-hat filter was used to correct the non-uniform illumination of the image. Then, the contrast was adjusted to enhance the variation of the color. The image was then transformed from RGB to HSV color space. The *regionprops* function was then used on the hue channel to detect the centroids and the region of interest of each marker. The boundaries of the region of interest of each marker were then used to define the boundaries of the subimages with 3-by-3 or 5-by-5 marker arrays.

## Hertzian curvature equivalence

Human and robot fingertips are spherical and soft. The shape and compliance allow them to grasp a wide variety of objects, by conforming to all sort of shapes and surface curvature. However, with our current manufacturing techniques, the high-density tactile sensors could only be manufactured in a planar form. To remain in a Hertzian contact condition, and ensure that the area of contact develops in a continuous surface, we reversed the roles and the object had a spherical form. According to Hertz contact theory, when two elastic body is in contact, only the relative radius $1/R_{\mathrm{eq}} = 1/R_{\mathrm{sphere}} + 1/R_{\mathrm{plane}}$ and indentation depth impacts the size of the contact area. Simulation in Comsol, shown Fig.5.15 , confirmed that the displacement field was similar when the sensor was spherical or flat as long as the average curvature of the contact was identical.

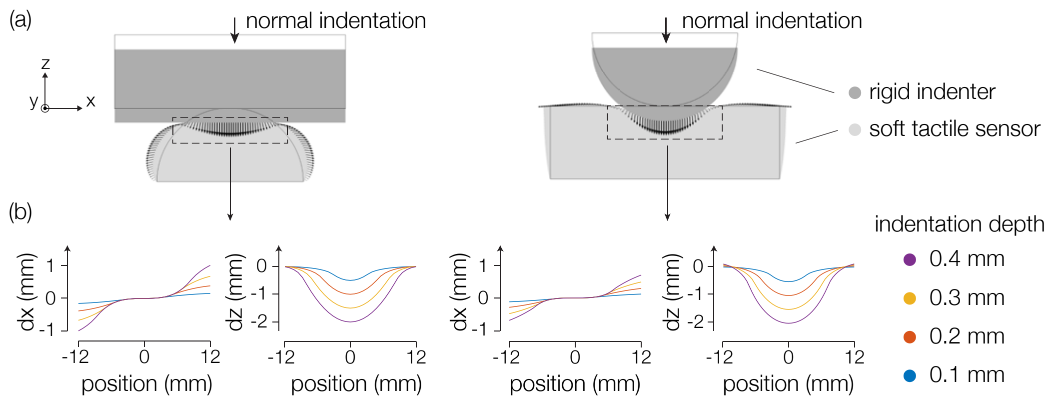


FIGURE 5.15: Simulation of a rigid spherical object pressing against a soft planar sensor develops a similar displacement field as pressing a rigid planar object against a soft spherical sensor.

Chapter 6

# Conclusion and future work

## Contents

THe thesis set out to build a tactile sensor able to provide a rich representation of the tactile scene that lives under robotics fingers. The research led to a novel tactile sensor based on embedded cameras, which is able to perceive important mechanical properties of the object in hand. The sensor uses color-mixing principle of a overlaid markers array to convert the mechanical interaction into a visual image captured by the embedded camera. Using inverse models, we show that we can compute the 3-dimensional displacement field with a fine spatial resolution directly from the image. This sensing design solve the common problem of the commercially available tactile sensors: low spatial resolution and lack of 3-dimensional measurements which are central to sensing contact information such as friction and slip. The main contributions of this research addresses: (1) the design and development of new tactile sensor for converting mechanical interaction into interpretable tactile data; (2) extraction of interaction information and object properties from the tactile data.

## 6.1 Camera-based transduction

A family of tactile sensors, named ChromaTouch, was developed in this research and rely on the color-mixing process. This sensing concept showed the possibility of converting the contact information into a change of color which can be used to subsequently reconstruct the 3-dimensional deformation of the soft membrane of the sensor. We then extended the concept to a hemispherical shape which conforms with a wider set of objects. This new sensors was able to estimate the global curvature of the object with few millimeter of indentation. We also improved the spatial resolution of the planar sensor that allows measurements of small object features. The sensor with high resolution is used to estimate the friction distribution of the contact surface. A representative sample of the numerous sensors fabricated during my studies are shown in Fig. 6.1.

The survey of the literature illustrates very well that robotic manipulation and grasping can fundamentally benefit from having tactile feedback. However, the relevant physics and metric that allows to depict a clear picture of the tactile interaction is still subject of debate. In this work we focused on extracting the meaningful mechanical information, that is not only an information about contact and interaction normal to the surface, but also lateral deformation that occurs due to frictional effects. But measuring the interaction in 3 dimensions is only useful if the spatial sampling of the contact scene is fine enough to resolve the subtle events that occurs inside the area of contact.

The sensor proposed in this research solves these two problems of dimensionality and density. The deformation induced by the "touch" of external objects is captured as 2d color images, from which information of the interaction and the object could be extracted. By embedding markers inside the elastic body, a deformation map with high spatial resolution could be reconstructed through marker tracking method. However, it is difficult to extracted the normal displacement of the markers from the 2d image captured by the embedded camera. ChromaTouch overcame this drawback by a method using color mixing principle. Two separate layers, one with opaque soft magenta markers and another with transparent rigid yellow markers of colored markers, are overlaid and embedded inside the elastic body of the sensor. When an external force deforms the sensor, the magenta marker is stretched, leading to color change of the overlaid marker patch. The normal displacement of each marker was found approximately proportional to the change of hue in HSV color space. One of the main advantages of using color channels to compute the normal displacement field is that the markers configuration can be resolved using just a few pixels. Comparing to methods that extract the normal deformation by counting the number of pixels containing in each marker, The change in color due to the stretch of the marker is not influenced by the resolution of the camera and the pixel density of the marker. Moreover, as in HSV color space the hue is independent to the brightness, using change of hue to compute the normal displacement shows good robustness to illumination non-uniformity. This process of encoding the normal displacement reach a precision of 50 $\mu$m. However, the calibration using hue value was later proved to lead underestimation on normal displacement of the markers due to the influence of coefficient of friction. To address this issue, a convolutional neural network was built to estimate the normal displacement of the marker. This model provides a goodness of fit of $R^2 = 99.2\%$ with the training data and $R^2 = 98.4\%$ with the testing data, which demonstrate the ability of generalizing to unknown data. This approach eliminates the influence of surface properties on normal displacements estimation and shows less noise compared to the method using the variation of hue. Besides, from the first version to the last version, the spatial resolution of the sensor was improved from 100 sensing points to 441 sensing points. This higher resolution enables a much denser measurements and the detection of smaller geometry variations of the object.

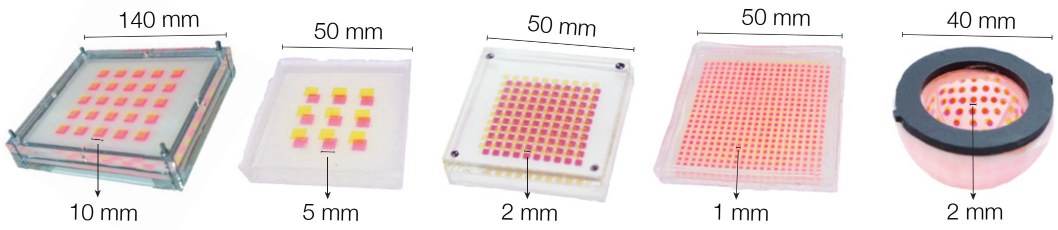


FIGURE 6.1: ChromaTouch Zoo: A representative subset of all the sensors fabricated during this thesis, from planar to spherical, from low resolution to high resolution.

## 6.2 Tactile perception

The hemispherical sensor is beneficial for exploration tasks as it allows the sensor tip to conform to the touched object with arbitrary shapes. For example, when the object has a concave shape, the mechanical interaction is discontinuous using flat sensor as the contact is made at the edge of the sensor. In contrast, a spherical sensor can ensure a continuous contact while pressing against an concave object if the sensor has a smaller radius than the convex object. With this hemispherical sensor, the curvature of the object was estimated by curve fitting the displacement field of the markers to the Hertz contact model. Imagine the task of grasping a calabash which has both concave and convex part. The concave part of the object would be a more stable grasping location because the gripper can have a larger contact area. Also, as the contact between the concave surface of the object and the convex surface of the sensor is similar to a spherical joint, a grasping location at concave region might limit the degree of freedom of the object and avoid dropping of the object. The curvature estimation method proposed in this work allows the sensor to estimate the curvature of the object after a 1 mm normal indentation, without needs of sliding motion. This estimation may provide the shape properties to robots as soon as the contact is made, and guide the grasping location of the robot to ensure a stable grasp.

However, we observed that the displacement of individual points did not follow a pure normal trajectory under normal pressure, which contradicts the prediction of Hertz theory. In addition to a normal motion, the markers also shifted toward the outside of the contact area due to the lateral expansion of the soft sensor under pressure. More interestingly, we found out that the lateral shift of the markers depends on the friction of the contact surface. Using the third version of the ChromaTouch sensor which has a planar sensor head and 441 sensing points, we demonstrated that this small lateral motion of the markers could be used for estimating coefficient of the surface without having to slide the sensor on the object. A high coefficient limits the lateral motion of the markers due to the adherence between two surfaces, while a low coefficient of friction allows the marker to move laterally following the lateral deformation of the soft sensor under only normal pressure. Based on this effect, a convolutional neural network was trained to predict local coefficient of friction of the contact surfaces using the images containing the pattern of the markers under normal load as input data. The proposed method allows the sensor to estimate the frictional state of the object via a simple press during the first contact. This early estimation of friction would allow the robot to adjust the grip force at the earlier state of grasping, even before any shear forces or slippage occurs. A more remarkable advantage of this method is that, it allows an estimation of the local coefficient of friction, such that the sensor is able to determine friction variations at the same contact surface. Experimental results shows that the sensor is capable of distinguishing two coefficient of friction existing on the same contact surface at first contact via a simple normal press. The fusion of the estimated displacement field and the coefficient of friction of each marker may show potential optimal grasping location for robot, because under the same grip force, the slippage is less possible to happen in the region with high friction. More importantly, using the method proposed in this work, the estimation of the curvature, the displacement field and the coefficient of friction could all be done via a simple normal pressure without any need of lateral sliding. It can provide robots an early estimate of the contact properties, in order to plan appropriate grip force and location for a stable grasping.

## 6.3 Future work

The sensor has shown its efficacy at perceiving shape and the coefficient of friction of an object at first contact, without requiring long and complex exploration of the tactile scene. As no tangential force or slippage is necessary to capture rich tactile data, this sensor could provide robots an early estimation of the object properties and ensure a stable manipulation. Future work will explore how the early perceptual cues can inform the control of complex robotic manipulation.

### 6.3.1 Manufacturing improvements

The spherical version of the sensor shows the most promise as it can conform to arbitrary shapes. However the current manufacturing capability limit the achievable resolution. We demonstrated that high resolution can be achieved on the planar sensor which is useful for fine measurements. The next step in sensor manufacturing will aim at combining the spherical sensing design with the high spatial resolution for implementation on robotic hands. Embedding a dense array of markers could largely improve the spatial resolution of the sensor, but also create manufacturing challenges.

At the time of writing, we are exploring multi-material 3-d printing which could help simplify the manufacturing procedure. In particular this would be beneficial for spherical sensors, which to date requires complex folding to ensure the overlapping of the markers. Softer material could also be used in future work, allowing the sensor to deform more easily and make a contact with arbitrary objects over a larger area. Also, softer material will improve the sensibility of the sensor as softer markers would be more stretched under the same force.

### 6.3.2 Machine learning improvements

Two methods for estimating the 3d displacement field were developed using color mixing and convolutional neural network, respectively. The convolutional neural network could eliminate the effect of friction on the estimation of normal displacement of the marker. However, the sensor is not sensitive enough to small details of complex shapes. Object features such as textures, small protrusions, and holes cannot be precisely detected by the sensor. Increasing the density of the markers and decreasing the size of the marker could improve the performance of the sensor on shape estimation. Enriching the training dataset using various objects could also be an effective way to increase the sensitivity of the sensor on small shape features. Also, in our work for friction estimation, only two different values of the friction were used in the experiments to test the proposed method. However, the coefficient of friction takes values ranging from 0 to $\approx$1 in real scenario. In addition, the friction estimation shows inaccuracies when the object has an irregular shape. In future work, more friction values should be included in the training data, so that the sensor would be able to estimate the friction in real manipulation tasks. Adding training data using more objects with different shapes could also increase the accuracy of friction estimation for different contact conditions. Lastly, to gather understanding of the set of feature that are relevant to classify and discriminate frictional patterns, future work will explore the use of explainable artificial intelligence to gather deeper understandings of the inner working of the networks.

### 6.3.3 Signal processing improvements

In this work, the sensor only measures the displacement of the markers. As a localized force applied at the center of the sensor will induce a displacement that has visible effects on all the markers, suitable means of measuring the force applied to the surface remain to be developed. Deconvolution methods [61] might be a way to determine the stress and traction forces exerted at the surface from the distribution of the markers.

In addition, for all the experiments carried out in this research, the images of the markers were firstly captured by the camera, and then processed offline using Matlab after gathering all the necessary images. The offline image processing allowed us to test the sensing designs and the estimation algorithms. However, real-time processing should be developed in order to use the sensor in real scenarios in the future.

## 6.4 Outlook

With this work, we demonstrated the possibility of gathering information about the state of the contact at the earliest instant of the interaction. This new outlook on tactile sensing allows understanding the contact conditions that constrain the interaction between the robotics finger and the object. This understanding will drive new perceptual capabilities to extract information about the nature of the object but also help plan complex and dexterous motion.

With this new sense, robot capabilities will expand to new and challenging tasks which are still unreachable today: Human-robot interactions will be safer with a soft touch applied by the robotic interface; surgical robots with the sense of touch would be able to sense local region of increased stiffness; robots could use their hands to explore dangerous areas that human cannot access and do different tasks without human interventions; assistive robots will be able to achieve dexterous manipulation to help elders and people with disabilities.

I foresee that, in a not very distant future, robots equipped with new generations of tactile-based control will play crucial roles in our society, allowing greater flexibility to unknown environments and help create a seamless collaboration between machines and humans.

# Appendix A

# Summary of Hertz contact theory

Hertz contact theory is a classical theory of contact mechanics, which provides a set of simple analytical equations relating the properties of the system to the developed stress of any two curved bodies of different radii of curvature in contact. The theory was presented by Heinrich Hertz in 1881 and is based on the following assumptions:

- The surfaces are continuous, smooth, nonconforming and frictionless,
- The size of the contact area is small compared to the size of the bodies,
- Each solid can be considered to behave as an elastic half-space in the vicinity of the contact zone,
- The gap h between the undeformed surfaces can be approximated by an expression of the form:

$$h = Ax^2 + By^2$$

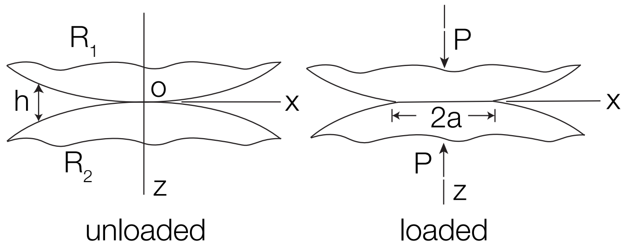


FIGURE A.1: Two objects in contact with or without loading force

For two elastic objects 1 and 2 of radii $R_1$ and $R_2$ pressed into contact with force P, the resultant circular contact area has radius a such that

$$a = \frac{3PR}{4E^*}^{1/3}$$

where $E^*$ is the contact modulus defined by

$$\frac{1}{E^*} = \frac{1-{\nu_1}^2}{E_1} + \frac{1-{\nu_2}^2}{E_2}$$

and R, the effective radius of curvature, is related to those of the individual components by the relation

$$\frac{1}{R} = \frac{1}{R_1} + \frac{1}{R_2}$$

For convex surfaces, the radii of curvature are positive, in contrary, those of concave surfaces have negative. For such a contact, the resulting pressure distribution $p(r)$ is parabolic of the form

$$p(r) = p_0 \left(1 - \frac{r^2}{a^2}\right)^{1/2} \quad \text{, where} \quad r^2 = x^2 + y^2 \tag{A.1}$$

The maximum pressure $p_0$ which occurs on the axis of symmetry of the pressure distribution is given by

$$p_0 = \frac{3P}{2\pi a^2}$$

Such a distribution is characteristic of Hertzian contact. Under this loading, the centers of the two spheres move together by the displacement $\delta$ where

$$\delta = \frac{a^2}{R} = \left(\frac{9P^2}{16RE^{*2}}\right)^{1/3}$$

The local normal displacement at the surface can be calculated by:

$$u_z = \delta(1 - r^2/2a^2)$$

The Hertz model is widely useful even though some assumptions are never strictly valid (e.g., some degree of friction will always occur between the two bodies). Even so, the Hertz model can be used as a first and often nearly exact approximation of the conditions in a contact between two objects.

However, the Hertz contact model only compute the information at the surface of the contact. One solution for solving the displacement field of the whole elastic body is to combine the Boussinesq-Cerruti function with Hook's law. The Boussinesq–Cerruti functions is widely used to compute the stress field of the whole elastic body for a given pressure by

$$\sigma_z = -\frac{2}{\pi} z \int \frac{p(r)}{((x-r)^2 + z^2)^2} \, dr$$

Combining the Hook's law that calculates the strain-stress relation of an elastic body by

$$\frac{\partial u_z}{\partial z} = \frac{1-\nu^2}{E} \sigma_z$$

the displacement field at any point of the elastic body could be resolved. With the pressure distribution at the contact surface $p(r)$ given by the equation A.1 from Hertz contact model, the displacement $u_z$ could be expressed in function of the contact area $a$.

# Bibliography


[1] N. A. Ahmad Ridzuan, S. Masuda, and N. Miki. "Flexible capacitive sensor encapsulating liquids as dielectric with a largely deformable polymer membrane". In: *Micro and Nano Letters* 7.12 (2012), pp. 1193–1196.

[2] Ahmed Alfadhel and Jürgen Kosel. "Magnetic Nanocomposite Cilia Tactile Sensor". In: *Advanced Materials* 27.47 (2015), pp. 7888–7892.

[3] T. André et al. "Effect of skin hydration on the dynamics of fingertip gripping contact". In: *Journal of the Royal Society Interface* 8.64 (2011), pp. 1574–1583.

[4] Anne Sophie Augurelle et al. "Importance of cutaneous feedback in maintaining a secure grip during manipulation of hand-held objects". In: *Journal of Neurophysiology* 89.2 (2003), pp. 665–671.

[5] Sang Hoon Bae et al. "Graphene-based transparent strain sensor". In: *Carbon* 51.1 (2013), pp. 236–242.

[6] Daulet Baimukashev, Zhanat Kappassov, and Huseyin Atakan Varol. "Shear, Torsion and Pressure Tactile Sensor via Plastic Optofiber Guided Imaging". In: *IEEE Robotics and Automation Letters* 5.2 (2020), pp. 2618–2625.

[7] Rongrong Bao et al. "Flexible and controllable piezo-phototronic pressure mapping sensor matrix by ZnO NW/p-polymer LED array". In: *Advanced Functional Materials* 25.19 (2015), pp. 2884–2891.

[8] Allan Barrea et al. "Perception of partial slips under tangential loading of the fingertip". In: *Scientific Reports* 8.1 (2018), pp. 1–8.

[9] *Barrett hand*. https://advanced.barrett.com/barretthand.

[10] Stefan Begej. "Planar and Finger-Shaped Optical Tactile Sensors for Robotic Applications". In: *IEEE Journal on Robotics and Automation* 4.5 (1988), pp. 472–484.

[11] Antonio Bicchi and Centro E Piaggio. "On the Closure Properties of Robotic Grasping". In: *J. of Robotics Research* 14.4.4 (1995), pp. 319–334.

[12] Antonio Bicchi, J. Kenneth Salisbury, and David L. Brock. "Contact Sensing from Force Measurements". In: *The International Journal of Robotics Research* 12.3 (1993), pp. 249–262.

[13] Antonio Bicchi, J. Kenneth Salisbury, and Pablo Dario. "Augmentation of grasp robustness using intrinsic tactile sensing". In: (1989), pp. 302–307.

[14] Ingvars Birznieks et al. "Encoding of direction of fingertip forces by human tactile afferents". In: *Journal of Neuroscience* 21.20 (2001), pp. 8222–8237.

[15] Ian M. Bullock and Aaron M. Dollar. "Classifying human manipulation behavior". In: *IEEE International Conference on Rehabilitation Robotics* (2011).

[16] Gereon H. Büscher et al. "Flexible and stretchable fabric-based tactile sensor". In: *Robotics and Autonomous Systems* 63.P3 (2015), pp. 244–252.

[17] Geneviève Cadoret and Allan M. Smith. "Friction, not texture, dictates grip forces used during object manipulation". In: *Journal of Neurophysiology* 75.5 (1996), pp. 1963–1969.

[18] Roberto Calandra et al. "More than a feeling: Learning to grasp and regrasp using vision and touch". In: *IEEE Robotics and Automation Letters* 3.4 (2018), pp. 3300–3307.

[19] Gaetano Canepa et al. "Detection of incipient object slippage by skin-like sensing and neural network processing". In: *IEEE Transactions on Systems, Man, and Cybernetics, Part B: Cybernetics* 28.3 (1998), pp. 348–356.

[20] Stefano Caselli, Corrado Magnanini, and Francesco Zanichelli. "On the robustness of haptic object recognition based on polyhedral shape representations". In: *IEEE International Conference on Intelligent Robots and Systems* 2 (1995), pp. 200–206.

[21] François Chaumette. "Image Moments: A General and Useful Set of Features for Visual Servoing". In: *IEEE Transactions on Robotics* 20.4 (2004), pp. 713–723.

[22] Ling Chen, Guohua Chen, and Liang Lu. "Piezoresistive behavior study on finger-sensing silicone rubber/graphite nanosheet nanocomposites". In: *Advanced Functional Materials* 17.6 (2007), pp. 898–904.

[23] Ning Chen, Ray Rink, and Hong Zhang. "Local object shape from tactile sensing". In: *Proceedings - IEEE International Conference on Robotics and Automation* 4.April (1996), pp. 3496–3501.

[24] Wei Chen et al. "An eight-legged tactile sensor to estimate coefficient of static friction: Improvements in design and evaluation". In: *Lecture Notes in Computer Science (including subseries Lecture Notes in Artificial Intelligence and Lecture Notes in Bioinformatics)* 9774 (2016), pp. 493–502.

[25] Byungjune Choi, Hyouk Ryeol Choi, and Sungchul Kang. "Development of tactile sensor for detecting contact force and slip". In: *2005 IEEE/RSJ International Conference on Intelligent Robots and Systems, IROS* (2005), pp. 2638–2643.

[26] Craig Chorley et al. "Development of a Tactile Sensor Based on Biologically Inspired Edge Encoding". In: *2009 IEEE International Conference on Advanced Robotics* (2009), pp. 1–6.

[27] Craig Chorley et al. "Tactile edge detection". In: *Proceedings of IEEE Sensors* (2010), pp. 2593–2598.

[28] Arlene B.A. Cole, John E. Hauser, and Shankar Sastry. "Kinematics and Control of Multifingered Hands with Rolling Contact". In: *IEEE Transactions on Automatic Control* 34.4 (1989), pp. 398–404.

[29] *Contactile*. https://contactile.com/.

[30] Tadeo Corradi, Peter Hall, and Pejman Iravani. "Bayesian tactile object recognition: Learning and recognising objects using a new inexpensive tactile sensor". In: *Proceedings - IEEE International Conference on Robotics and Automation* 2015-June.June (2015), pp. 3909–3914.

[31] Darryl P.J. Cotton et al. "A novel thick-film piezoelectric slip sensor for a prosthetic hand". In: *IEEE Sensors Journal* 7.5 (2007), pp. 752–761.

[32] Luke Cramphorn, Benjamin Ward-Cherrier, and Nathan F. Lepora. "Addition of a Biomimetic Fingerprint on an Artificial Fingertip Enhances Tactile Spatial Acuity". In: *IEEE Robotics and Automation Letters* 2.3 (2017), pp. 1336–1343.

[33] A. Cranny et al. "Thick-film force, slip and temperature sensors for a prosthetic hand". In: *Measurement Science and Technology* 16.4 (2005), pp. 931–941.

[34] Ravinder S. Dahiya et al. "Tactile sensing-from humans to humanoids". In: *IEEE Transactions on Robotics* 26.1 (2010), pp. 1–20.

[35] Hao Dang and Peter K. Allen. “Stable grasping under pose uncertainty using tactile feedback”. In: *Autonomous Robots* 36.4 (2014), pp. 309–330.

[36] Javad Dargahi and Siamak Najarian. “Human tactile perception as a standard for artificial tactile sensing - a review”. In: *International Journal of Medical Robotics and Computer Assisted Surgery* 01.01 (2004), p. 23.

[37] P. Dario. “Tactile sensing: Technology and applications”. In: *Sensors and Actuators: A. Physical* 26.1-3 (1991), pp. 251–256.

[38] Benoit Delhaye, Philippe Lefèvre, and Jean Louis Thonnard. “Dynamics of fingertip contact during the onset of tangential slip”. In: *Journal of the Royal Society Interface* 11.100 (2014).

[39] Siyuan Dong, Wenzhen Yuan, and Edward H. Adelson. “Improved GelSight tactile sensor for measuring geometry and slip”. In: *IEEE International Conference on Intelligent Robots and Systems* 2017-Septe (2017), pp. 137–144.

[40] Elliott Donlon et al. “GelSlim: A High-Resolution, Compact, Robust, and Calibrated Tactile-sensing Finger”. In: *IEEE/RSJ International Conference on Intelligent Robots and Systems (IROS)* (2018).

[41] Alin Drimus et al. “Classification of rigid and deformable objects using a novel tactile sensor”. In: *IEEE 15th International Conference on Advanced Robotics: New Boundaries for Robotics, ICAR 2011* (2011), pp. 427–434.

[42] Alin Drimus et al. “Design of a flexible tactile sensor for classification of rigid and deformable objects”. In: *Robotics and Autonomous Systems* 62.1 (2012), pp. 3–15.

[43] A. Faragasso et al. “Multi-axis stiffness sensing device for medical palpation”. In: *IEEE International Conference on Intelligent Robots and Systems* 2015-Decem (2015), pp. 2711–2716.

[44] Ronald S. Fearing and T. O. Binford. “Using a Cylindrical Tactile Sensor for Determining Curvature”. In: *IEEE Transactions on Robotics and Automation* 7.6 (1991), pp. 806–817.

[45] Raul Fernandez et al. “Micro-vibration-based slip detection in tactile force sensors”. In: *Sensors (Switzerland)* 14.1 (2014), pp. 709–730.

[46] Nicola J. Ferrier and Roger W. Brockett. “Reconstructing the shape of a deformable membrane from image data”. In: *International Journal of Robotics Research* 19.9 (2000), pp. 795–816.

[47] Jeremy A. Fishel and Gerald E. Loeb. "Bayesian exploration for intelligent identification of textures". In: *Frontiers in Neurorobotics* 6.JUNE (2012), pp. 1–20.

[48] Jeremy A. Fishel and Gerald E. Loeb. "Sensing tactile microvibrations with the BioTac Comparison with human sensitivity". In: *Proceedings of the IEEE RAS and EMBS International Conference on Biomedical Robotics and Biomechatronics* (2012), pp. 1122–1127.

[49] Kinya Fujita and Hisayuki Ohmori. "A new softness display interface by dynamic fingertip contact area control". In: *Proceedings of the 5th World Multiconference on Systemics, Cybernetics and Informatics* (2001), pp. 78–82.

[50] *GelSight*. https://gelsight.com/.

[51] Masanori Goka, Hiroyuki Nakamoto, and Satoru Takenawa. "A magnetic type tactile sensor by GMR elements and inductors". In: *IEEE/RSJ 2010 International Conference on Intelligent Robots and Systems, IROS 2010 - Conference Proceedings* (2010), pp. 885–890.

[52] A. W. Goodwin, K. T. John, and A. H. Marceglia. "Tactile discrimination of curvature by humans using only cutaneous information from the fingerpads". In: *Experimental Brain Research* 86.3 (1991), pp. 663–672.

[53] Feng Guo et al. "Measurement of three-dimensional deformation and load using vision-based tactile sensor". In: *IEEE International Symposium on Industrial Electronics* 2016-Novem (2016), pp. 1252–1257.

[54] Mallory L. Hammock et al. "25th anniversary article: The evolution of electronic skin (E-Skin): A brief history, design considerations, and recent progress". In: *Advanced Materials* 25.42 (2013), pp. 5997–6038.

[55] Hiraishi Hisato et al. "An Object Profile Detection by a High Resolution Tactile Sensor Using an Optical Conductive Plate". In: *Proc. of IECON '88 14th Annual Conf. of IEEE Industrial Electronics Society* (1988).

[56] Van Anh Ho and Shinichi Hirai. "A novel model for assessing sliding mechanics and tactile sensation of human-like fingertips during slip action". In: *Robotics and Autonomous Systems* 63.P3 (2015), pp. 253–267.

[57] Van Anh Ho et al. "What can be inferred from a tactile arrayed sensor in autonomous in-hand manipulation?" In: *IEEE International Conference on Automation Science and Engineering* (2012), pp. 461–468.

[58] Francois R. Hogan et al. "Tactile Dexterity: Manipulation Primitives with Tactile Feedback". In: (2020).

[59] Francois R. Hogan et al. "Tactile Regrasp: Grasp Adjustments via Simulated Tactile Transformations". In: *IEEE International Conference on Intelligent Robots and Systems* (2018), pp. 2963–2970.

[60] Neville Hogan. "Impedance control: An approach to manipulation: Part I - Theory". In: (1985), pp. 1–7.

[61] Robert D. Howe and Mark R. Cutkosky. "Dynamic Tactile Sensing: Perception of Fine Surface Features with Stress Rate Sensing". In: *IEEE Transactions on Robotics and Automation* 9.2 (1993), pp. 140–151.

[62] Robert D. Howe and Mark R. Cutkosky. "Sensing skin acceleration for slip and texture perception". In: *IEEE International Conference on Robotics and Automation* June 1989 (1989), pp. 145–150.

[63] Dimitris Hristu, Nicola Ferrier, and Roger W Brockett. "The performance of a deformable-membrane tactile". In: *IEEE International Conference on Robotics and Automation* April (2000), pp. 508–513.

[64] Yating Hu et al. "Bioinspired 3-D tactile sensor for minimally invasive surgery". In: *Journal of Microelectromechanical Systems* 19.6 (2010), pp. 1400–1408.

[65] Charles Hudin, Sabrina Panëels, and Steven Strachan. "INTACT: Instant interaction with 3D printed objects". In: *Conference on Human Factors in Computing Systems - Proceedings* 07-12-May- (2016), pp. 2719–2725.

[66] Atsutoshi Ikeda et al. "Grip force control for an elastic finger using vision-based incipient slip feedback". In: *2004 IEEE/RSJ International Conference on Intelligent Robots and Systems (IROS)* 1.May 2014 (2004), pp. 810–815.

[67] Jacob N. Israelachvili. *Intermolecular and Surface Forces*. 2011.

[68] Yuji Ito, Youngwoo Kim, and Goro Obinata. "Robust slippage degree estimation based on reference update of vision-based tactile sensor". In: *IEEE Sensors Journal* 11.9 (2011), pp. 2037–2047.

[69] Yuji Ito et al. "Vision-based tactile sensing and shape estimation using a fluid-type touchpad". In: *IEEE Transactions on Automation Science and Engineering* 9.4 (2012), pp. 734–744.

[70] Nawid Jamali et al. "A new design of a fingertip for the iCub hand". In: *IEEE International Conference on Intelligent Robots and Systems* 2015-Decem (2015), pp. 2705–2710.

[71] Jasper W. James and Nathan F. Lepora. "Slip detection for grasp stabilisation with a multi-fingered tactile robot hand". In: *arXiv preprint* (2020), pp. 1–14.

[72] Jasper W. James, Stephen J. Redmond, and Nathan F. Lepora. "A Biomimetic Tactile Fingerprint Induces Incipient Slip". In: *arXiv preprint* (2020), pp. 9833–9839.

[73] Jasper Wollaston James, Nicholas Pestell, and Nathan F. Lepora. "Slip detection with a biomimetic tactile sensor". In: *IEEE Robotics and Automation Letters* 3.4 (2018), pp. 3340–3346.

[74] R S Johansson and G Westling. "Roles of glabrous skin receptors and sensorimotor memory in automatic control of precision grip when lifting rougher or more slippery objects". In: *Experimental brain research* 56.3 (1984), pp. 550–564.

[75] Roland S. Johansson and J. Randall Flanagan. "Coding and use of tactile signals from the fingertips in object manipulation tasks". In: *Nature Reviews Neuroscience* 10.5 (2009), pp. 345–359.

[76] R.S. Johansson and A.B. Vallbo. "Tactile sensibility in the human hand: Relative and absolute densities of four types of mechanoreceptive units in glabrous skin". In: *Journal of Physiology* 286 (1979), pp. 283–300.

[77] K L Johnson. *Contact Mechanics*.

[78] K. O. Johnson. "The roles and functions of cutaneous mechanoreceptors". In: *Current Opinion in Neurobiology* 11.4 (2001), pp. 455–461.

[79] Micah K. Johnson and Edward H. Adelson. "Retrographic sensing for the measurement of surface texture and shape". In: *2009 IEEE Computer Society Conference on Computer Vision and Pattern Recognition Workshops, CVPR Workshops 2009* 2009 IEEE (2009), pp. 1070–1077.

[80] Micah K. Johnson et al. "Microgeometry capture using an elastomeric sensor". In: *ACM Transactions on Graphics* 30.4 (2011), p. 1.

[81] Mohsen Kaboli, Kunpeng Yao, and Gordon Cheng. "Tactile-based manipulation of deformable objects with dynamic center of mass". In: *IEEE-RAS International Conference on Humanoid Robots* (2016), pp. 752–757.

[82] Asuka Kadowaki et al. "Development of soft sensor exterior embedded with multi-axis deformable tactile sensor system". In: *Proceedings - IEEE International Workshop on Robot and Human Interactive Communication* (2009), pp. 1093–1098.

[83] K. Kamiyama et al. "Evaluation of a vision-based tactile sensor". In: *IEEE International Conference on Robotics and Automation* 2 (2004), pp. 1542–1547.

[84] Kazuto Kamiyama et al. "A Vision-based Tactile Sensor". In: *Stress: The International Journal on the Biology of Stress* (2001).

[85] Kazuto Kamiyama et al. "Vision-based sensor for real-time measuring of surface traction fields". In: *IEEE Computer Graphics and Applications* 25.1 (2005), pp. 68–75.

[86] Peter Kampmann and Frank Kirchner. "Integration of fiber-optic sensor arrays into a multi-modal tactile sensor processing system for robotic end-effectors". In: *Sensors (Switzerland)* 14.4 (2014), pp. 6854–6876.

[87] Zhanat Kappassov et al. "Color-coded fiber-optic tactile sensor for an elastomeric robot skin". In: *Proceedings - IEEE International Conference on Robotics and Automation* 2019-May (2019), pp. 2146–2152.

[88] Astrid M.L. Kappers. "Human perception of shape from touch". In: *Philosophical Transactions of the Royal Society B: Biological Sciences* 366.1581 (2011), pp. 3106–3114.

[89] Anwesha Khasnobish et al. "Object-shape recognition and 3D reconstruction from tactile sensor images". In: *Medical and Biological Engineering and Computing* 52.4 (2014), pp. 353–362.

[90] Marliese Kimmerle. "The Functional Repertoire of the Hand and Its Application to Assessment". In: *American Journal of Occupational Therapy* 57.5 (2003), pp. 489–498.

[91] Roberta L. Klatzky and Susan J. Lederman. "Identifying objects from a haptic glance". In: *Perception & Psychophysics* 57.8 (1995), pp. 1111–1123.

[92] G. Murali Krishna and K. Rajanna. "Tactile sensor based on piezoelectric resonance". In: *IEEE Sensors Journal* 4.5 (2004), pp. 691–697.

[93] Mike Lambeta et al. "DIGIT: A Novel Design for a Low-Cost Compact High-Resolution Tactile Sensor with Application to In-Hand Manipulation". In: *IEEE Robotics and Automation Letters* 5.3 (2020), pp. 3838–3845.

[94] Susan J. Lederman and Roberta L. Klatzky. "Extracting object properties through haptic exploration". In: *Acta Psychologica* 84.1 (1993), pp. 29–40.

[95] Christoph Ledermann et al. "Tactile sensor on a magnetic basis using novel 3D Hall sensor - First prototypes and results". In: *INES 2013 - IEEE 17th International Conference on Intelligent Engineering Systems, Proceedings* (2013), pp. 55–60.

[96] Hyung Kew Lee et al. "Normal and shear force measurement using a flexible polymer tactile sensor with embedded multiple capacitors". In: *Journal of Microelectromechanical Systems* 17.4 (2008), pp. 934–942.

[97] Nathan Lepora, Uriel Martinez-Hernandez, and Tony Prescott. "Active Bayesian Perception for Simultaneous Object Localization and Identification". In: *Robotics: Science and Systems* (2013).

[98] Nathan F. Lepora. "Biomimetic Active Touch with Fingertips and Whiskers". In: *IEEE Transactions on Haptics* 9.2 (2016), pp. 170–183.

[99] Nathan F. Lepora, Kirsty Aquilina, and Luke Cramphorn. "Exploratory Tactile Servoing with Active Touch". In: *IEEE Robotics and Automation Letters* 2.2 (2017), pp. 1156–1163.

[100] Nathan F. Lepora and John Lloyd. "Optimal deep learning for robot touch: Training accurate pose models of 3D surfaces and edges". In: *IEEE Robotics and Automation Magazine* 27.2 (2020), pp. 66–77.

[101] Nathan F. Lepora et al. "From Pixels to Percepts: Highly Robust Edge Perception and Contour Following Using Deep Learning and an Optical Biomimetic Tactile Sensor". In: *IEEE Robotics and Automation Letters* 4.2 (2019), pp. 2101–2107.

[102] Chunyan Li et al. "Flexible dome and bump shape piezoelectric tactile sensors using PVDF-TrFE copolymer". In: *Journal of Microelectromechanical Systems* 17.2 (2008), pp. 334–341.

[103] Qiang Li et al. "Grasp point optimization by online exploration of unknown object surface". In: *IEEE-RAS International Conference on Humanoid Robots* (2012), pp. 417–422.

[104] Rui Li and Edward H. Adelson. "Sensing and recognizing surface textures using a gelsight sensor". In: *Proceedings of the IEEE Computer Society Conference on Computer Vision and Pattern Recognition* (2013), pp. 1241–1247.

[105] Rui Li et al. "Localization and manipulation of small parts using GelSight tactile sensing". In: *IEEE International Conference on Intelligent Robots and Systems* 1.IROS (2014), pp. 3988–3993.

[106] Xi Lin and Michael Wiertlewski. "Sensing the Frictional State of a Robotic Skin via Subtractive Color Mixing". In: *IEEE Robotics and Automation Letters* 4.3 (2019), pp. 2386–2392.

[107] Xi Lin et al. "Curvature sensing with a spherical tactile sensor using the color-interference of a marker array". In: *Proceedings IEEE International Conference on Robotics and Automation.* (2020).

[108] Hongbin Liu et al. "Classification using a Tactile Array Sensor". In: *IEEE International Conference on Robotics and Automation* (2012), pp. 1410–1415.

[109] Weiting Liu et al. "Fingertip Piezoelectric Tactile Sensor Array for Roughness Encoding under Varying Scanning Velocity". In: *IEEE Sensors Journal* 17.21 (2017), pp. 6867–6879.

[110] Yi Hung Liu et al. "Low-resolution tactile image recognition for automated robotic assembly using kernel PCA-based feature fusion and multiple kernel learning-based support vector machine". In: *Mathematical Problems in Engineering* 2014 (2014).

[111] David G. Lowe. "Distinctive image features from scale-invariant keypoints". In: *International Journal of Computer Vision* 60.2 (2004), pp. 91–110.

[112] Qiujie Lu et al. "Precise In-Hand Manipulation of Soft Objects using Soft Fingertips with Tactile Sensing and Active Deformation". In: *2020 3rd IEEE International Conference on Soft Robotics, RoboSoft 2020* (2020), pp. 52–57.

[113] Shan Luo et al. "Iterative Closest Labeled Point for tactile object shape recognition". In: *IEEE International Conference on Intelligent Robots and Systems* 2016-Novem (2016), pp. 3137–3142.

[114] Shan Luo et al. "Novel Tactile-SIFT Descriptor for Object Shape Recognition". In: *IEEE Sensors Journal* 15.9 (2015), pp. 5001–5009.

[115] Daolin Ma et al. "Dense tactile force estimation using gelslim and inverse FEM". In: *Proceedings - IEEE International Conference on Robotics and Automation* 2019-May (2019), pp. 5418–5424.

[116] H. Maekawa et al. "Development of a finger-shaped tactile sensor and its evaluation by active touch". In: *Proceedings 1992 IEEE International Conference on Robotics and Automation* (1992), pp. 1327–1334.

[117] Hitoshi Maekawa, Kazuo Tanie, and Kijoshi Komoritya. “Finger-shaped tactile sensor using an optical waveguide”. In: *Proceedings of the IEEE International Conference on Systems, Man and Cybernetics* 5 (1993), pp. 403–408.

[118] Hitoshi Maekawa et al. “Development of a miniaturized model of a finger shaped tactile sensor using an optical waveguide”. In: *IECON Proceedings (Industrial Electronics Conference)* 3 (1991), pp. 2478–2483.

[119] Takashi Maeno, Shinichi Hiromitsu, and Takashi Kawai. “Control of grasping force by detecting stick/slip distribution at the curved surface of an elastic finger”. In: *Proceedings - IEEE International Conference on Robotics and Automation* 4 (2000), pp. 3895–3900.

[120] Takashi Maeno, Tomoyuki Kawamura, and Sen Chieh Cheng. “Friction estimation by pressing an elastic finger-shaped sensor against a surface”. In: *IEEE Transactions on Robotics and Automation* 20.2 (2004), pp. 222–228.

[121] Stefan C.B. Mannsfeld et al. “Highly sensitive flexible pressure sensors with microstructured rubber dielectric layers”. In: *Nature Materials* 9.10 (2010), pp. 859–864.

[122] Benjamin W. McInroe et al. “Towards a Soft Fingertip with Integrated Sensing and Actuation”. In: *IEEE International Conference on Intelligent Robots and Systems* (2018), pp. 6437–6444.

[123] Martin Meier et al. “Distinguishing sliding from slipping during object pushing”. In: *IEEE International Conference on Intelligent Robots and Systems* 2016-Novem (2016), pp. 5579–5584.

[124] Philipp Mittendorfer and Gordon Cheng. “Humanoid multimodal tactile-sensing modules”. In: *IEEE Transactions on Robotics* 27.3 (2011), pp. 401–410.

[125] Jocelyn Monnoyer et al. “Perception of Ultrasonic Switches Involves Large Discontinuity of the Mechanical Impedance”. In: *IEEE Transactions on Haptics* 11.4 (2018), pp. 579–589.

[126] David J. Montana. “The Kinematics of Contact and Grasp”. In: *The International Journal of Robotics Research* 7.3 (1988), pp. 17–32.

[127] Adithyavairavan Murali et al. “Learning to Grasp Without Seeing”. In: *International Symposium on Experimental Robotics* (2018), pp. 375–386.

[128] Naoki Nakao et al. "A finger shaped tactile sensor using an optical waveguide". In: *IECON Proceedings (Industrial Electronics Conference)* 1 (1990), pp. 300–305.

[129] Lorenzo Natale and Eduardo Torres-jara. "A sensitive approach to grasping". In: *Proceedings of the sixth international workshop on epigenetic robotics* (2006), pp. 87–94.

[130] Goro Obinata et al. "Vision Based Tactile Sensor Using Transparent Elastic Fingertip for Dexterous Handling". In: *Mobile Robots: Perception & Navigation* February (2007).

[131] Shogo Okamoto, Hikaru Nagano, and Yoji Yamada. "Psychophysical dimensions of tactile perception of textures". In: *IEEE Transactions on Haptics* 6.1 (2013), pp. 81–93.

[132] Allison M Okamura and Mark R Cutkosky. "for Haptic Exploration". In: *Haptics, IEEE Transactions on* (2001).

[133] Allison M. Okamura, Niels Smaby, and Mark R. Cutkosky. "Overview of dexterous manipulation". In: *Proceedings - IEEE International Conference on Robotics and Automation* 1.April (2000), pp. 255–262.

[134] Taiyu Okatani et al. "A tactile sensor using piezoresistive beams for detection of the coefficient of static friction". In: *Sensors (Switzerland)* 16.5 (2016).

[135] Derek Olczak, Vaishnavi Sukumar, and J. Andrew Pruszynski. "Edge orientation perception during active touch". In: *Journal of Neurophysiology* 120.5 (2018), pp. 2423–2429.

[136] Luke Osborn et al. "Neuromimetic Event-Based Detection for Closed-Loop Tactile Feedback Control of Upper Limb Prostheses". In: *IEEE Transactions on Haptics* 9.2 (2016), pp. 196–206.

[137] Tiago Paulino et al. "Low-cost 3-axis soft tactile sensors for the human-friendly robot Vizzy". In: *Proceedings - IEEE International Conference on Robotics and Automation* (2017), pp. 966–971.

[138] Peng Peng and Rajesh Rajamani. "Flexible microtactile sensor for normal and shear elasticity measurements". In: *IEEE Transactions on Industrial Electronics* 59.12 (2012), pp. 4907–4913.

[139] Zachary Pezzementi et al. "Tactile-object recognition from appearance information". In: *IEEE Transactions on Robotics* 27.3 (2011), pp. 473–487.

[140] Matti Pietikäinen, Timo Ojala, and Zelin Xu. "Rotation-invariant texture classification using feature distributions". In: *Pattern Recognition* 33.1 (2000), pp. 43–52.

[141] Jonathan Platkiewicz, Hod Lipson, and Vincent Hayward. “Haptic Edge Detection Through Shear”. In: *Scientific Reports* 6.November 2015 (2016), pp. 1–10.

[142] Marsela Polic et al. “Convolutional Autoencoder for Feature Extraction in Tactile Sensing”. In: *IEEE Robotics and Automation Letters* 4.4 (2019), pp. 3671–3678.

[143] Mario Prats, Pedro J. Sanz, and Angel P. Del Pobil. “Reliable non-prehensile door opening through the combination of vision, tactile and force feedback”. In: *Autonomous Robots* 29.2 (2010), pp. 201–218.

[144] Tony J. Prescott, Mathew E. Diamond, and Alan M. Wing. “Active touch sensing”. In: *Philosophical Transactions of the Royal Society B: Biological Sciences* 366.1581 (2011), pp. 2989–2995.

[145] Branden Romero, Filipe Veiga, and Edward Adelson. “Soft, Round, High Resolution Tactile Fingertip Sensors for Dexterous Robotic Manipulation”. In: (2020), pp. 4796–4802.

[146] Tatsuya Sakuma et al. “A Universal Gripper Using Optical Sensing to Acquire Tactile Information and Membrane Deformation”. In: *2018 IEEE/RSJ International Conference on Intelligent Robots and Systems (IROS)* (2018), pp. 6431–6436.

[147] Pornthep Sarakon et al. “Object Shape and Force Estimation using Deep Learning and Optical Tactile Sensor”. In: *Proceedings of The 6th IIAE International Conference on Intelligent Systems and Image Processing* September (2018), pp. 205–212.

[148] Katsunari Sato et al. “Finger-shaped GelForce: Sensor for measuring surface traction fields for robotic hand”. In: *IEEE Transactions on Haptics* 3.1 (2010), pp. 37–47.

[149] Katsunari Sato et al. “Measurement of force vector field of robotic finger using vision-based haptic sensor”. In: *2008 IEEE/RSJ International Conference on Intelligent Robots and Systems, IROS* (2008), pp. 488–493.

[150] Alexander Schmitz et al. “A prototype fingertip with high spatial resolution pressure sensing for the robot iCub”. In: *2008 8th IEEE-RAS International Conference on Humanoid Robots, Humanoids 2008* (2008), pp. 423–428.

[151] Alexander Schmitz et al. “A tactile sensor for the fingertips of the humanoid robot iCub”. In: *IEEE/RSJ 2010 International Conference on Intelligent Robots and Systems, IROS 2010 - Conference Proceedings* (2010), pp. 2212–2217.

[152] Alexander Schmitz et al. “Tactile object recognition using deep learning and dropout”. In: *IEEE-RAS International Conference on Humanoid Robots* (2014), pp. 1044–1050.

[153] Alexander Schneider et al. “Object identification with tactile sensors using bag-of-features”. In: *2009 IEEE/RSJ International Conference on Intelligent Robots and Systems, IROS 2009* (2009), pp. 243–248.

[154] John L. Schneiter and Thomas B. Sheridan. “An optical tactile sensor for manipulators”. In: *Robotics and Computer Integrated Manufacturing* 1.1 (1984), pp. 65–71.

[155] *Schunk 3 fingered hand*. https://schunk.com/de_en/gripping-systems/series/sdh/.

[156] Gregor Schwartz et al. “Flexible polymer transistors with high pressure sensitivity for application in electronic skin and health monitoring”. In: *Nature Communications* 4.May (2013).

[157] N. Tamil Selvan et al. “Piezoresistive natural rubber-multiwall carbon nanotube nanocomposite for sensor applications”. In: *Sensors and Actuators, A: Physical* 239 (2016), pp. 102–113.

[158] Lucia Seminara et al. “Piezoelectric polymer transducer arrays for flexible tactile sensors”. In: *IEEE Sensors Journal* 13.10 (2013), pp. 4022–4029.

[159] Carmelo Sferrazza and Raffaello D’Andrea. “Design, motivation and evaluation of a full-resolution optical tactile sensor”. In: *Sensors (Switzerland)* 19.4 (2019).

[160] *Shadow hand with Biotac*. https://www.shadowrobot.com/.

[161] Wenceslao Shaw-Cortez et al. “Robust object manipulation for tactile-based blind grasping”. In: *Control Engineering Practice* 92.September (2019), p. 104136.

[162] Wenceslao Shaw-Cortez et al. “tactile-based blind grasping: A discrete-time object manipulation controller for robotic hands”. In: *IEEE Robotics and Automation Letters* 5.2 (2018), pp. 3475–3476.

[163] Makoto Shimojo. “Mechanical filtering effect of elastic cover for tactile sensor”. In: *IEEE Transactions on Robotics and Automation* 13.1 (1997), pp. 128–132.

[164] Kazuhiro Shimonomura. “Tactile image sensors employing camera: A review”. In: *Sensors (Switzerland)* 19.18 (2019), pp. 1–21.

[165] Hiroyuki Shinoda, Kenichi Matsumoto, and Shigeru Ando. "Acoustic resonant tensor cell for tactile sensing". In: *Proceedings - IEEE International Conference on Robotics and Automation* 4.April (1997), pp. 3087–3092.

[166] Hiroyuki Shinoda, Shinya Sasaki, and Katsuhiko Nakamura. "Instantaneous Evaluation of Friction Based on ARTC Tactile Sensor". In: *IEEE International Conference on Robotics and Automation* (2000), pp. 73–78.

[167] Gabor Soter et al. "MultiTip: A multimodal mechano-thermal soft fingertip". In: *2018 IEEE International Conference on Soft Robotics, RoboSoft 2018* (2018), pp. 239–244.

[168] Mandayam A. Srinivasan and Robert H. LaMotte. "Tactual Discrimination of Softness". In: *Neurophysiology* 73.1 (1995).

[169] M. W. Strohmayr, H. Worn, and G. Hirzinger. "The DLR artificial skin step I: Uniting sensitivity and collision tolerance". In: *Proceedings - IEEE International Conference on Robotics and Automation* (2013), pp. 1012–1018.

[170] Zhe Su et al. "Force estimation and slip detection/classification for grip control using a biomimetic tactile sensor". In: *IEEE-RAS International Conference on Humanoid Robots* 2015-Decem (2015), pp. 297–303.

[171] Zhe Su et al. "Use of tactile feedback to control exploratory movements to characterize object compliance". In: *Frontiers in Neurorobotics* 6.JULY (2012), pp. 1–9.

[172] K Tanie et al. "A High Resolution Tactile Sensor". In: *Proc. of 4th Int. Conf. on Robot Vision and Sensory Controls* (1984).

[173] Alexander V. Terekhov and Vincent Hayward. "Minimal adhesion surface area in tangentially loaded digital contacts". In: *Journal of Biomechanics* 44.13 (2011), pp. 2508–2510.

[174] Stephen Tian et al. "Manipulation by feel: Touch-based control with deep predictive models". In: *Proceedings - IEEE International Conference on Robotics and Automation* 2019-May (2019), pp. 818–824.

[175] Tito Pradhono Tomo et al. "Covering a Robot Fingertip With uSkin: A Soft Electronic Skin With Distributed 3-Axis Force Sensitive Elements for Robot Hands". In: *IEEE Robotics and Automation Letters* 3.1 (2018), pp. 124–131.

[176] Marc R Tremblay and Mark R Cutkosky. "Estimating Friction Using Incipient Slip Sensing During a Manipulation Task". In: *Proceedings IEEE International Conference on Robotics and Automation.* (1993), pp. 429–434.

[177] Jun Ueda et al. "Development of the NAIST-hand with vision-based tactile fingertip sensor". In: *Proceedings - IEEE International Conference on Robotics and Automation* 2005.April (2005), pp. 2332–2337.

[178] A. B. Vallbo and R.S Johansson. "Properties of cutaneous mechanoreceptors in the human hand related to touch sensation". In: *Human Neurobiology* 3.1 (1984), pp. 3–14.

[179] Herke Van Hoof et al. "Learning robot in-hand manipulation with tactile features". In: *IEEE-RAS International Conference on Humanoid Robots* 2015-Decem (2015), pp. 121–127.

[180] Fabrizio Antonio Viola et al. "Ultrathin, flexible and multimodal tactile sensors based on organic field-effect transistors". In: *Scientific Reports* 8.1 (2018), pp. 1–8.

[181] Antti Virta et al. "Force sensing using artificial magnetic cilia". In: *IEEE International Conference on Intelligent Robots and Systems* (2012), pp. 1–6.

[182] *Visevi*. `https://www.visevi.com/en/product-tactile.html`.

[183] J. J. Wang et al. "Nanocomposite rubber elastomer with piezoresistive detection for flexible tactile sense application". In: *Proceedings of the IEEE International Conference on Micro Electro Mechanical Systems (MEMS)* (2017), pp. 720–723.

[184] Benjamin Ward-Cherrier, Luke Cramphorn, and Nathan F. Lepora. "Exploiting Sensor Symmetry for Generalized Tactile Perception in Biomimetic Touch". In: *IEEE Robotics and Automation Letters* 2.2 (2017), pp. 1218–1225.

[185] Benjamin Ward-Cherrier, Luke Cramphorn, and Nathan F. Lepora. "Tactile Manipulation With a TacThumb Integrated on the Open-Hand M2 Gripper". In: *IEEE Robotics and Automation Letters* 1.1 (2016), pp. 169–175.

[186] Benjamin Ward-Cherrier et al. "The TacTip Family: Soft Optical Tactile Sensors with 3D-Printed Biomimetic Morphologies". In: *Soft Robotics* 00.00 (2018), soro.2017.0052.

[187] Norinao Watanabe and Goro Obinata. "Grip force control based on the degree of slippage using optical tactile sensor". In: *International Symposium on Micro-NanoMechatronics and Human Science.* (2007), pp. 466–471.

[188] S. Weinstein. "Intensive and Extensive Aspects of Tactile Sensitivity". In: *The Skin Senses: Proceedings* (1968), pp. 195–218.

[189] Nicholas Wettels, Jeremy A. Fishel, and Gerald E. Loeb. "Multimodal tactile sensor". In: *Springer Tracts in Advanced Robotics* 95.0912260 (2014), pp. 405–405.

[190] Nicholas Wettels et al. "Biomimetic tactile sensor array". In: *Advanced Robotics* 22.8 (2008), pp. 829–849.

[191] Michael Wiertlewski, José Lozada, and Vincent Hayward. "The spatial spectrum of tangential skin displacement can encode tactual texture". In: *IEEE Transactions on Robotics* 27.3 (2011), pp. 461–472.

[192] Laurence Willemet et al. "The mechanics of tactile perception of friction on initial contact". In: (2020).

[193] Benjamin Winstone et al. "TACTIP - Tactile fingertip device, challenges in reduction of size to ready for robot hand integration". In: *2012 IEEE International Conference on Robotics and Biomimetics, ROBIO 2012 - Conference Digest* (2012), pp. 160–166.

[194] Benjamin Winstone et al. "TACTIP-tactile fingertip device, texture analysis through optical tracking of skin features". In: *Conference on Biomimetic and Biohybrid Systems* (2013), pp. 323–334.

[195] Danfei Xu, Gerald E. Loeb, and Jeremy A. Fishel. "Tactile identification of objects using Bayesian exploration". In: *Proceedings - IEEE International Conference on Robotics and Automation* (2013), pp. 3056–3061.

[196] Akihiko Yamaguchi and Christopher G. Atkeson. "Combining finger vision and optical tactile sensing: Reducing and handling errors while cutting vegetables". In: *IEEE-RAS International Conference on Humanoid Robots* (2016), pp. 1045–1051.

[197] Akihiko Yamaguchi and Christopher G. Atkeson. "Implementing tactile behaviors using FingerVision". In: *IEEE-RAS International Conference on Humanoid Robots* (2017), pp. 241–248.

[198] Zhengkun Yi, Yilei Zhang, and Jan Peters. "Bioinspired tactile sensor for surface roughness discrimination". In: *Sensors and Actuators, A: Physical* 255 (2017), pp. 46–53.

[199] Chen Yu et al. “A vision-based soft somatosensory system for distributed pressure and temperature sensing”. In: *IEEE Robotics and Automation Letters* 5.2 (2020), pp. 3323–3329.

[200] Ping Yu et al. “Flexible piezoelectric tactile sensor array for dynamic three-axis force measurement”. In: *Sensors (Switzerland)* 16.6 (2016).

[201] Wenzhen Yuan, Siyuan Dong, and Edward H. Adelson. “GelSight: High-resolution robot tactile sensors for estimating geometry and force”. In: *Sensors (Switzerland)* 17.12 (2017).

[202] Wenzhen Yuan, Mandayam A. Srinivasan, and Edward H. Adelson. “Estimating object hardness with a GelSight touch sensor”. In: *IEEE International Conference on Intelligent Robots and Systems* 2016-Novem (2016), pp. 208–215.

[203] Wenzhen Yuan et al. “Active clothing material perception using tactile sensing and deep learning”. In: *Proceedings - IEEE International Conference on Robotics and Automation* 1 (2018), pp. 4842–4849.

[204] Wenzhen Yuan et al. “Measurement of shear and slip with a GelSight tactile sensor”. In: *Proceedings - IEEE International Conference on Robotics and Automation* 2015-June.June (2015), pp. 304–311.

[205] Wenzhen Yuan et al. “Shape-independent hardness estimation using deep learning and a GelSight tactile sensor”. In: *Proceedings - IEEE International Conference on Robotics and Automation* (2017), pp. 951–958.

[206] Hanafiah Yussof et al. “Determination of object stiffness control parameters in robot manipulation using a prototype optical three-axis tactile sensor”. In: *Proceedings of IEEE Sensors* (2008), pp. 992–995.

[207] Hong Zhang and Ning Nicholas Chen. “Control of contact via tactile sensing”. In: *IEEE Transactions on Robotics and Automation* 16.5 (2000), pp. 482–495.

[208] Yazhan Zhang et al. “Effective Estimation of Contact Force and Torque for Vision-Based Tactile Sensors With Helmholtz–Hodge Decomposition”. In: *IEEE Robotics and Automation Letters* 4.4 (2019), pp. 4094–4101.

[209] Yin Zhu et al. “A new robotic tactile sensor with bio-mimetic structural colour inspired by Morpho butterflies”. In: *Bioinspiration and Biomimetics* 14.5 (2019).